NASA Contractor Report 175041

Experiments on Two Opposed Lateral Jets Injected into Swirling Crossflow

C.B. McMurry and D.G. Lilley
Oklahoma State University
Stillwater, Oklahoma

January 1986

Prepared for
Lewis Research Center
Under Grant NAG 3-549

NASA
National Aeronautics and
Space Administration

TABLE OF CONTENTS

NOMENCLATURE

A_c	cross-sectional area of crossflow
A_j	cross-sectional area of jet
D	test section diameter
d	inlet nozzle diameter
d_j	lateral jet inlet diameter
R	jet-to-crossflow velocity ratio
Re	Reynolds number
$\bar{V} = (u,v,w)$	time-mean velocity in facility coordinates (x-, r-, θ-directions)
x,r,θ	axial, radial, azimuthal coordinates
ϕ	swirl vane angle with respect to facility axis
θ	traverse azimuthal angle

Subscripts

o	value at inlet to flowfield
rms	root-mean-squared

Superscripts

$(\bar{\ })$	time-mean average
$( )'$	fluctuating component
$(\tilde{\ })$	relative to probe coordinates

CHAPTER I

INTRODUCTION

1.1 Preamble

In both can and annular combustion chambers lateral jets of cooler air are injected into the flowfield through round holes in the combustor walls. These jets enhance the performance of the combustor by altering the aerodynamics. In the swirl-induced central recirculation region of the primary zone, where most fuel burning takes place, additional air is provided by some of the lateral jets for stoichiometric conditions. In the secondary zone, other jets provide additional air to help complete combustion. Similar jets cool and evenly mix the products of combustion in the dilution zone before the flow enters the turbine. Similar processes occur in ramjet combustors. The complex nature of these flowfields has resulted in the design and development of combustors being based largely on experimental trial and error research programs.

Recently, however, there has become increased emphasis on theoretical modeling of combustor flows, the success of which will lead to reduced time and cost of experimental research programs. Their development requires the existence of an accurate data base (for a variety of flow types) with which to compare predictions and further develop models for improved accuracy. Problems and progress in this area are extensively reviewed in recent textbooks. Schetz[1] concentrates on the physics and modeling of injection and mixing of turbulent flows;

Lefebvre[2] acknowledges that the phenomena are of paramount importance in the combustion and dilution zones, and presents recent progress and its relevance to combustor design requirements. Reference 3 provides an extensive compendium of information about swirl flows, and flowfield modeling and diagnostic techniques are digested in Reference 4.

Research in progress at Oklahoma State University is concerned with combustor flowfields in the absence of combustion. The experimental results being obtained add to the detailed data base. A recent Ph. D. thesis[5] discusses hot-wire measurements of a single lateral jet being injected into nonswirling crossflow, and presents flow visualization results concerning injection into swirling crossflow, with crossflow swirl vane angle ϕ = 0 (swirler removed), 45 and 70 degrees. Results with lateral jet to crossflow velocity ratio $R = v_j/u_o$ = 2, 4 and 6 were presented in all cases investigated. Three research papers have also evolved[6-8] from the recent study. All flowfields being investigated under this program at Oklahoma State University have no expansion of the crossflow (the test section to swirler diameter ratio D/d = 1), after its passage through an optional swirler (with swirl vane angle ϕ = 0 (swirler removed), 45 and 70 degrees). The lateral jet(s) is(are) located one test-section diameter downstream of the test-section inlet (x/D = 1). The lateral jets have round nozzles, each of which has an area of 1/100th of the cross-sectional area of the crossflow (A_j/A_c = 1/100).

1.2 The Present Contribution

Two opposed lateral jets injected normally into swirling crossflow is the focus of the present study. It complements a concurrent study

investigating a single lateral jet being injected normally into swirling crossflow,[9] and previous studies on similar configurations with swirl but without lateral injection,[10,11] and with lateral injection but without swirl.[5] The present research investigates three particular flowfields having lateral jet to crossflow velocity ratio $R = v_j/u_o = 4$ only, with swirl vane angle $\phi = 0$ (swirler removed), 45 and 70 degrees being used with the main crossflow. Specific objectives included:

1. Flow visualization of the flowfield using neutrally-buoyant helium-filled soap bubbles, and multi-sparks.
2. Detailed hot-wire measurements of time-mean velocities, three normal and three shear turbulent stresses using the six-orientation single-wire hot-wire technique.

1.3 Previous Studies

Previous research conducted at Oklahoma State University on combustor-type flowfields without lateral injection jets are summarized by Lilley.[10,11] They included experimental and theoretical research under low speed, nonreacting, turbulent, swirling flow conditions. The flow enters the test section and preceeds into a larger chamber (the expansion D/d = 2, 1.5 or 1) via a sudden or gradual expansion (side-wall angle α = 90 and 45 degrees). A weak or strong nozzle may be positioned downstream to form a contraction exit to the test section. Inlet swirl vanes are adjustable to a variety of vane angles with values of ϕ = 0 (swirler removed), 38, 45, 60 and 70 degrees being emphasized. The objective was to determine the effect of these parameters on isothermal flowfield patterns, time-mean velocities and turbulence quantities, and to establish an improved simulation in the

form of a computer prediction code equipped with a suitable turbulence model. Helium bubble flow visualization, five-hole pitot probe time-mean velocity measurements, and one-wire and two-wire hot-wire normal and shear stress turbulence data were obtained in the experimental program. Turbulence modeling deductions and flowfield predictions were made via a 2-D axisymmetric technique.

An outgrowth of the above research is the research program at Oklahoma State University which deals both experimentally and theoretically with the problem of primary and dilution lateral jet injection into typical combustor flowfields in the absence of combustion. Parameter variations to be systematically investigated include: lateral jet velocity, number and location of lateral jets, combustor crossflow inlet swirl strength, and downstream contraction nozzle location and strength. The general goal is to characterize the time-mean and turbulence flowfield with a variety of parameter settings, recommend appropriate turbulence model advances, and implement and exhibit results of flowfield predictions.

Significant earlier studies elsewhere include Chassaing et al,[12] Rathgeber and Becker,[13] Crabb et al[14] and Holdeman et al.[15] The recent Ph. D. thesis by Ferrell[5] provides an extensive review of these and other studies on the lateral jet injected into crossflow. Ferrell completed his detailed work on the single lateral injected jet with velocity ratio $R = v_j/u_o = 2$, 4 and 6 entering into nonswirling crossflow, using the six-orientation single hot-wire measurement technique. In addition to this, several flow visualization techniques (bubbles, smoke and sparks) were used with these same velocity ratios into swirling crossflow, with swirl vane angle $\phi = 0$ (swirler removed),

45 and 70 degrees. Detailed measurements were not made for these swirling cases. Conference papers were prepared by Ferrell and colleagues dealing with preliminary results and computer simulation,[6] flow visualization,[7] and detailed hot-wire measurements.[8]

The objective of current research is to emphasize the swirl effect on lateral injection into tubular crossflow. A concurrent research effort on the single lateral jet with R = 4 entering the 0, 45 and 70 degree swirling crossflow is being undertaken by Ong.[9] The present study is highlighted by two opposed lateral jets with R = 4 entering the 0, 45 and 70 degree swirling crossflow.

1.4 Outline of the Thesis

The first chapter of this five-chapter thesis is the introduction. The importance of deflected jets in combustor flowfields is briefly described. Previous work related to combustor flowfield experiments are summarized.

Chapter II describes the experimental facility, test-section, and dilution jets. The data acquisition system is briefly described and other equipment used in the investigation is mentioned.

Flow visualization and measurement techniques are discussed in Chapter III. Results of the flow visualization and measurement techniques are discussed thoroughly in Chapter IV. Chapter V presents the conclusions to be drawn from this investigation.

Appendix A, Figures 4 through 7 present flow visualization photographs. Figures 8 through 25 are two-dimensional plots of the time-mean and turbulent flowfield.

CHAPTER II

EXPERIMENTAL FACILITY

2.1 Wind Tunnel And Vane Swirler

The experimental facility is the same as used on the previous experimental program without lateral jets and described at length in previous M. S. and Ph. D. theses and in abbreviated form in several conference papers included in Ref. 10. A complete description of the wind tunnel, nozzle and facility layout is given by Ferrell.[5] The test facility is shown schematically in Figure 1 of Appendix A. It consists of a wind tunnel, a variable-angle vane swirler, and a plexiglass test section of diameter 15 cm. The wind tunnel has a contraction section whose contour conforms to the method of design suggested by Morel[16] to produce a minimum adverse pressure gradient on the boundary layer and thus avoid unsteady problems associated with local separation regions. The air-flow passes through a 15 cm diameter circular jet nozzle, exiting into a 15 cm diameter test section of length 90 cm, which is constructed of plexiglass to facilitate flow visualization.

A variable-angle vane swirler may be positioned immediately before the test section. Its flow area has an outer diameter of 15 cm. The swirler has ten vanes which are individually adjustable to any angle ϕ and a hub with a streamlined upstream nose and a flat downstream face. The nose has a hyperbolic shape with a very smooth surface so as to offer minimal flow interference. The flat blades are wedge-shaped to

offer minimal flow interference. The flat blades are wedge-shaped to give a constant pitch-to-chord ratio of 0.68 which gives good turning efficiency.[3] Its performance is documented elsewhere.[10] The test section begins at a location x/D = 0, which is 3.2 cm downstream of the swirler exit.

2.2 Test Section and Dilution Jets

Figure 1 also shows the configuration of the 15 cm diameter test section (the same as the exit throat) mounted on the wind tunnel with the swirler omitted. Air to the lateral dilution jets is supplied from a compressed air line via piping and carefully-designed nozzles. Upstream of each nozzle, a stagnation chamber, turbulence management screens, flow straightening straws, and flow metering equipment are used for flow conditioning. Experiments have been performed on the present study with the two opposed lateral jets located one test-section diameter downstream of the inlet.

The test section consists of a clear acrylic tube approximately 90 cm in length attached to the wind tunnel throat. Standard commercial acrylic tube is used with 15.24 cm (6.0 in.) outside diameter, 0.318 cm (0.125 in.) wall thickness. The inside diameter is 14.61 cm with a measured variation of ± 0.05 cm. To adapt the test section to the wind tunnel throat (inside diameter 15 cm), an adaptor section was machined to provide a smooth transition from the wind tunnel throat to the test section.

The test section tube allows probe access to locations downstream of x/D = 1.75, 2.00, 2.50, 3.00 and at any azimuthal angle. This is accomplished via a tube rotation section, constructed from machined

aluminum rings, acrylic, and ball bearings as seen in Figure 2. A photograph showing both jets in position on the test section is seen in Figure 3. Also visible is the valve arrangement for five-hole pitot probe measurements.

A more complete description of the dilution jets and air supply appears in Reference 5.

2.3 Equipment

Equipment used in this investigation includes the calibration jet, data acquisition and probe drive system, DISA type 55P01 normal hot-wire probe, DISA 55M21 probe support, DISA 55M01 anemometer, Burr-Brown SDM853 12-bit A/D converter, and an Apple IIe computer. These are the same as used previously and described in full in Reference 5.

CHAPTER III

INVESTIGATION TECHNIQUES

3.1 Bubble Flow Visualization

Flow visualization[4,17] is used primarily for the identification and characterization of the flowfield, with two techniques being used in the present study: bubbles (described in the present section) and sparks (described in the next section). The equipment and techniques are described fully by Ferrell and colleagues [5,7] in regard to their use on the present facility.

Bubbles, because of their reflective qualities and neutral buoyancy in the airflow, provide an excellent medium to determine the paths of the jet trajectories. The technique has been used on investigations without lateral jet injection[10,11] and on the single lateral jet injection.[5,7] A bubble generator, manufactured by Sage Action, Inc. is used to supply up to 100 bubbles per second, and inject them into the lower lateral jet.

The lighting for bubble flow visualization consists of light from a high-intensity slide projector located approximately 3 m downstream of the test section. A slit in an opaque slide provides a vertical light curtain about 1.5 cm wide. The lighting is on throughout the photography session and the exposure time of typically 5 seconds permits streamlines to be identified. The camera used is a Minolta SRI 200. The films used include Kodak Tri-X Pann 400 ASA black and white, Ilford

400 ASA black and white, and Kodak color 1000 ASA film, with all of these giving excellent results. The camera is positioned approximately 0.5 m laterally from the test section and supported by a tripod. A low F-stop of 2 is used for maximum light intake,to accentuate the bubble streaklines illustrating the flow trajectories.

3.2 Spark Flow Visualization

A multi-spark visualization method has also been used on the present study.[4,5,7] The technique uses an ionized path between two electrodes. This path moves with the air flow, and is sequentially lit up by successive sparks. The pulse generating circuit and pulse transformer are manufactured by Sugawara Laboratories, Inc., Tokyo. Equipment specifications and operating procedures are given in References 5 and 7.

When a high voltage source is sparked across an air gap, an ionized path is created. Subsequent sparks will follow the current position of this low-resistance ionized path. By placing electrodes in the wall boundary layer, where there is essentially zero velocity (next to the wall), several discharges can follow the ionized path as it moves with the fluid. The test section materials must have low electrical conductivity such as acrylic so as not to interfere with spark paths. The spark itself provides sufficient lighting for photographs. One camera (side view) is used for photographs with zero swirl. Two cameras (side and end view) are used simultaneously in the swirl crossflow cases to give added perspective to the three-dimensional features of the resulting flowfield.

3.3 Hot-Wire Anemometry

In a turbulent, three-dimensional flowfield the main flow direction may be unknown and conventional hot-wire or Laser-Doppler techniques fail to supply sufficient velocity vector information. To measure the three velocity components and their corresponding fluctuations, a three-wire hot-wire probe is often used. Few 3-D Laser-Doppler systems are in use and are not cost-effective. The three-wire probe technique has several drawbacks. Three anemometers are required. A multiple-orientation probe drive may be needed to align the probe with the mean flow direction. Because of the physical separation of the wires, spatial resolution of the probe is poor. A recent textbook surveys the experimental challenges and assesses available techniques.[4]

Multi-orientation of a single hot-wire is a novel way to measure the three components of a velocity vector and their fluctuating components. In the present study, the six-orientation single-wire hot-wire method is used exclusively for detailed measurements. It is described in the M.S. and Ph.D. theses of Janjua[18] and Jackson.[19] This method calls for a normal hot wire to be oriented through six different positions, each orientation separated by 30 degrees from the adjacent one. Orientation 1 is normal to the facility centerline, orientation 2 is rotated 30 degrees from this, etc. Time-mean and root-mean-square voltages are measured at each orientation. The data reduction is performed using several simplifying assumptions regarding the statistical nature of turbulence, making it possible to solve for three time-mean velocities, the three turbulent normal stresses, and the three turbulent shear stresses.

The six-orientation hot-wire technique requires a single, straight,

hot wire to be calibrated for three different flow directions in order to determine the directional sensitivity of the probe. When the wire is placed in a three-dimensional flowfield, the effective cooling velocity experienced by the hot wire may be deduced from the calibration curves. Hence, equations for the effective cooling velocity can be obtained for each of the six wire orientations. Simultaneously solving any three adjacent equations provides expressions for the instantaneous values of the three velocity components (u, v, and w in the facility x, r, and θ coordinates, respectively) in terms of the equivalent cooling velocities. It is then possible to obtain the three time-mean velocity components and the six different components of the Reynolds stress tensor in the manner described by Janjua[18] and Jackson,[19] which is described briefly in research papers included in Ref. 10. Jackson also assessed the accuracy and directional sensitivity of the technique, concluding that severe inaccuracies may be present, especially in the deduced shear stress values which are discussed in section 4.2. Jackson found that the configuration of probes versus local flow direction is of little importance. He recommended evaluating quantities from the average of all six possible wire combinations, and this smoothing has been used exclusively in recent studies and in the present study.

CHAPTER IV

RESULTS AND DISCUSSION

4.1 Flow Visualization

Neutrally-buoyant helium filled soap bubbles injected through the lower jet, located at x/D = 1.0, trace pathlines clearly when illuminated. Figure 4 presents time exposures of bubble pathlines for the case of 2 jets, R = 4, ϕ = 0 (swirler removed), 45, and 70 degrees in parts a, b, and c respectively. Vertical slit lighting is used as discussed in Section 3.1 to obtain a view of the rx-plane.

Part a reveals the depth of penetration of the dilution jet. The jet does not cross the centerline of the test section because of the symmetry effect of the presence of the opposing dilution jet. Ferrell[5] found for the case of a single lateral jet with the same velocity ratio R = 4 that the jet penetrates the test-section centerline at approximately x/D = 1.4. In the swirl flow case, parts b and c of Figure 4, the extent of jet penetration is not readily discernable. In the case of ϕ = 45, the helical path of the jet is visible. The region from the dilution jet inlet x/D = 1.00 to approximately x/D = 2.00 indicates, by lack of visible bubbles that the jets do not immediately mix with the precessing vortex core (PVC). The jet trajectory has spiraled away from the light curtain. The presence of the opposed jets appears to delay the onset of mixing with the PVC as compared to the case of one dilution jet.[5] In the case of ϕ = 70 degrees, the

centrally-located PVC occupies a much narrow region in the opposed jet case, as compared with the single and no lateral injection jet cases.[19,20] The flow centerline is slightly deflected from the facility centerline throughout the test section, appearing to oscillate about the centerline for the strong swirl case.

Figures 5, 6, and 7 present multispark flow visualization pictures for the R = 4 jet entering different crossflow swirl conditions with ϕ = 0 (swirler removed), 45 and 70 degrees of swirl, respectively. Electrodes are positioned at x/D = 0.5, 1.5, 2.0, and 2.5 in parts a, b, c, and d respectively, to identify changes in the flowfield with movement downstream. The opposed jets are located at x/D = 1.

In Figure 5, the camera is positioned to the side of the test section to obtain a view of the rx-plane. Part a exhibits a roughly turbulent velocity profile although the initial sparks which are now further downstream show some deformation. A probable cause for the deformation of the spark path is the vicinity of the metal swirler assembly, which provides an alternative spark-gap. In part b of Figure 5, the influence of the opposed jets is clearly visible. Near the center of the test section, the flow is accelerated as indicated by the larger spacing between the sparks near the center of the section. Near the top and bottom of the test section, the presence of the opposed jets is indicated by the sparks wrapping around the boundaries of the jets. In part c and d, the wrap around of the sparks is still visible, but much less intense. With distance downstream the opposed jets tend to amalgamate with the crossflow to exhibit the characteristic flat velocity profile of turbulent flows in round tubes.

In Figures 6 and 7 which include the effects of swirl, a second

camera was positioned downstream and simultaneously operated to obtain the rθ-plane behavior. The rx-plane and the rθ-plane photographs were then combined to form a common picture of the flow behavior at various x/D locations. A wire was placed at the centerline of the test section to prevent the spark from arcing to the tube wall and to help define the center of the tube. The end views show a considerable reflection of the spark off the test section wall.

In Figure 6, with swirl vane angle ϕ = 45 degrees, little variation in the swirl pattern is distinguishable up to x/D = 2.5. At x/D = 2.5 however, there appears to be an elongation of successive sparks, and a strengthening of the centrally located PVC. The apparent strengthening of the PVC corresponds well with the appearance of bubbles in the bubble-flow visualization pictures of Figure 4b. Figure 7 presents multi-spark photography for the case of ϕ = 70 degrees. At x/D = 0.5 and 1.5, interpreting the flowfield is difficult due to the spark pattern. The spark path appears to have arced past the wire at the center of the test section. It does not exhibit the symmetric swirl pattern of the locations x/D = 2.0 and 2.5. At x/D = 2.0, part c of Figure 7, the symmetrical spark shows no direct influence from the opposed jets such as being deflected around the jets. However, comparing parts c and d of the same figure, the spark pattern appears to occupy an increasing area of the test section with distance downstream of the entrance of the opposed jets, located at x/D = 1. The effect may be accounted for by the opposed jets mixing with the crossflow as the flow progresses downstream.

4.2 Hot-Wire Measurements

Figures 8 through 25 present the time mean and turbulence

quantities for jet-to-crossflow velocity ratio R = 4, swirl vane angle ϕ = 0 (swirler removed), 45, and 70 degrees. Figures 9 through 13 have a swirl vane angle ϕ = 0 (swirler removed) with a jet-to-crossflow velocity ratio of R = 4. Figure 8 has a traverse angle θ = 270 degrees, Figure 9 has a traverse angle θ = 300 degrees, etc. Figures 14 through 19 have R = 4 with swirl angle ϕ = 45 degrees. Figures 20 through 25 present the case of R = 4, swirl angle ϕ = 70 degrees. The geometrical relationship of the traverse angle to the test section may be seen in Figure 2. For the traverse angle θ = 0 degrees, the viewer is seeing a vertical rx-plane of the flowfield which passes through the test-section centerline and through the opposed jet nozzles, as in Figure 11 for example.

In each of the Figures 8 through 25, subparts a, b, and c present normalized time-mean velocity components; subparts d, e, and f give normalized fluctuating velocity components (normal stresses); subparts g, h, and i exhibit normalized shear stresses, and subparts j, k, and l provide normalized total velocity, axial turbulence intensity, and turbulent kinetic energy, respectively. As mentioned previously, the accuracy of results for turbulence quantities (normal stresses and especially shear stresses) is in doubt. Jackson[19] discussed the quality of the hot-wire technique in a weakly swirling axisymmetric expanded flowfield with D/d = 2. He found that in turbulent shear regions, the maximum errors are 18, 24, 29, and 98 percent for time-mean values, normal stresses, shear stresses and $\overline{u'w'}$, respectively. The present study emphasizes the stronger swirl without expansion into the test section and may have potentially further accuracy problems. One major limitation with the present data acquisition system is the limited

sampling rate of 1000 Hz. Higher frequency signals are not properly digitized due to an aliasing effect. Signal frequencies above 1000 Hz should be filtered out in the data acquisition system. However, the data acquisition system used in this study does not include the use of a filter. Thus, the data includes any aliasing of high frequency signals. The amalgamated effect of these uncertainties leads to an unknown degree of error in the calculated values of turbulence quantities, especially the shear stresses. There are no alternative sources of data with which to compare the deduced values.

The plots were produced on a Tektronix 4006 terminal connected to an IBM 3081D using PLOT 10 as the graphics control language. The data are merely scaled and plotted point-to-point for each axial location. The x/D scales also provide as the magnitude scale for each normalized data point. For example, in Figure 8a, the values of $\bar{u}/u_o$ at x/D = 1.75 are scaled such that values of $\bar{u}/u_o$ = 1.0 are placed at x/D = 2.00.

The case of jet-to-crossflow velocity ratio R = 4 and swirl vane angle ϕ = 0 degrees (swirler removed) is presented in Figures 8 through 13. Figure 11a presents the axial velocity profiles through the center of both jets. At x/D = 1.75 it appears the opposed jets have already met at the centerline of the test-section as evidenced by the higher velocities at the centerline. At x/D = 2.00, the jets are mixing with the crossflow tending to decrease the centerline velocity. At x/D = 2.5, the velocity profile is uniform throughout the test section. Figure 8 provides a view of the flowfield normal to the entrance direction of the opposed jets. At x/D = 1.75, parts a and j show the jets to have met near the centerline. At x/D = 2.00, the crossflow appears to have accelerated around the sides of the jet, due to the

obstruction to flow caused by the jets. With distance downstream, the velocity profiles begin to flatten out.

The case of jet-to-crossflow velocity ratio R = 4 and swirl angle ϕ = 45 degrees is presented in Figures 14 through 19. Figure 17 presents a vertical rx-plane view of the flowfield, passing through the entrance of the opposed jets. There is evidence of a precessing vortex core (PVC) as indicated in Figure 17, parts a, c and j, by the low axial velocity and almost solid body rotation near the axis at the center of the test section. The upstream velocity of the crossflow is measured before the crossflow reaches the swirler. Thus, after introduction into the swirler, the net crossflow velocity experienced by the opposed jets is larger due to the swirl component of the total crossflow velocity. Thus, the true jet-to-crossflow velocity ratio is lower, which will reduce the penetration of the opposed jets into the crossflow.[5] For the 45 degree swirl case, the R value is reduced to approximately 2.8.

The angle δ between the local crossflow direction and the plane normal to the facility centerline is calculated by δ = arctan (u/w) locally. Near the injection locations of the lateral jets, this angle is approximately δ = 45 degrees for the moderate swirl case (ϕ = 45 degrees). For the strong swirl case (ϕ = 70 degrees) the angle δ is approximately 27 degrees. A spiralling path on the tube wall would require a normalized downstream distance of L/D = π(tan δ) to complete one revolution of the tube. The trajectory of the lateral jets follow roughly this path, but the angle δ changes as the jet penetrates into the field. Assuming the angle δ remains constant, for the moderate swirl case of ϕ = 45 degrees (δ = 45 degrees), the required normalized downstream distance is L/D = 3.14; for the ϕ = 70 degree case (δ = 26

degrees), L/D = 1.5. Hence, evidence of the lateral jets are expected to be seen at x/D = 1.75 in the θ = 270 degree traverse, etc. for the moderate swirl case. For the strong swirl case, it is expected to be seen at x/D = 1.75 in the θ = 0 degree traverse, at x/D = 2.0 in the θ = 300 degree traverse, etc.

The clearance requirement of the probe-drive system does not allow measurements to be taken upstream of x/D = 1.75 so tracking of initial jet trajectories is not possible. However, the presence of the opposed jets is visible in Figure 14 (a, b, c, and j), θ = 270 degrees. The lateral jets are swept along with the swirling crossflow. The two axial velocity maxima indicating the presence of the jets at x/D = 1.75 are not visible at the other downstream locations. The jets may be traced further downstream by viewing Figure 16 (θ = 330 degrees), parts a and j, at x/D = 2.00. Similar velocity maxima are observable in Figure 15a (θ = 300 degrees) at x/D = 2.00 but at a lower axial velocity. It appears that the traverse of Figure 16a at x/D = 2.00 came near the center of the jets while the traverse of Figure 15a merely passed through the edge of the jet boundaries. The effect of the opposed jets on the velocity profiles may be seen in Figures 14 through 17. Comparing part a of these figures, the axis of symmetry for the time-mean velocities appears to shift around the centerline of the test section. The shear stresses $\overline{u'v'}/u_o^2$ and $\overline{u'w'}/u_o^2$, parts g and h of these figures respectively, are evenly distributed throughout the test section.

In the strong swirl case, ϕ = 70 degrees, the angle between the local crossflow direction and the plane normal to the facility centerline, δ = arctan (u/w) = 27 degrees near the lateral jet injection

locations, as discussed previously. This requires approximately a downstream distance of L/D = 1.5 for the path of the jet to ideally make one revolution, with evidence of the lateral jet expected to be seen at x/D = 1.75 in the r = 0 degree traverse, at x/D = 2.00 in the r = 300 degree traverse, etc. Time-mean and turbulent quantity profiles are presented in Figures 20 through 25 for the case of jet-to-crossflow velocity ratio R = 4, swirl vane angle d = 70 degrees. Part a of the figures show that most of the flow is confined to the region near the wall due to high centrifugal forces. The reduced jet-to-crossflow velocity ratio, because of the swirling velocity component in the crossflow, results in the true jet-to-crossflow ratio R at approximately 1.2. Previous studies[5] show that jet penetration into the crossflow will be substantially reduced. Flow visualization photographs indicate that this is indeed the case. Figures 20 through 25 show no direct evidence of the jets. However, as noted in the case of d = 45 degrees, their effect on the symmetry of the velocity profiles is indicated by comparing the velocity profiles of part a in Figures 20 through 25. The symmetry of the velocity profiles is somewhat distorted, indicating the jets are disturbing the flowfield. The oscillations visible along the centerline of the test-section in Figure 4c are not related to shifts in the PVC axis. Part c of Figures 20 through 25 show the swirl axis and hence, the PVC, to remain along the test-section centerline.

CHAPTER V

CLOSURE

5.1 Conclusions

Experiments have been conducted to obtain the time-mean and turbulent quantities of opposed lateral jets in a low speed, nonreacting flowfield. A jet-to-crossflow velocity ratio of R = 4 only, with crossflow inlet swirler vane angles ϕ = 0 (swirler removed), 45, and 70 degrees were investigated. Flow visualization techniques, with neutrally-buoyant helium-filled soap bubbles and multi-spark photography, were used to identify flowfield characteristics such as jet penetration into the flowfield. Time-mean and turbulent quantities were determined using a six-orientation single hot-wire technique.

Flow visualization shows that the jets do not penetrate past the centerline of the test-section in the nonswirling case, ϕ = 0 (swirler removed). Measurements, using the six-orientation single hot-wire technique, indicated that this is indeed the case. In the swirling cases, the crossflow tends to remain in the region near the wall. The jets are deflected from their vertical course into a spiral course with the main flow. The jets were also found not to deflect the axis of the precessing vortex core. In the case of moderate swirl, swirl vane angle ϕ = 45 degrees, the jets could be tracked following a spiral trajectory. With strong swirl, swirl vane angle ϕ = 70 degrees, the jet trajectories are difficult to determine. The data indicate that

symmetry of the velocity profiles is disturbed due to the presence of the jets for the x/D locations considered. Jet penetration into the crossflow is reduced due to the additional velocity component introduced into the crossflow by swirl.

Normal stresses, were found to be highest near the center of test-section. The shear stresses remain low across the test-section.

As previously mentioned, there are uncertainties concerning the accuracy of the calculated values of the turbulence quantities. The present data acquisition system is limited to a sampling rate of 1000 Hz. To decrease any aliasing effects, higher turbulence frequencies should be filtered out. The accuracy of the turbulence quantity calcuations may also be increased by conducting an energy spectrum analysis to determine the relevant range of turbulence frequencies. Increasing the sampling rate to frequencies above the range of the relevant turbulent frequencies, combined with appropriate filtering, could greatly increase the accuracy of turbulent quantity measurements.

5.2 Recommendations for Further Work

This experiment is the first investigation into the effects of opposed jets on time-mean and turbulent quantities in swirling crossflow. Ong[9] presents the case of one laterally injected jet, jet-to-crossflow velocity ratio R = 4, with swirl vane angle d = 0 (swirler removed), 45, and 70 degrees. Further experiments should be carried out for jet-to-crossflow velocity ratios of R = 2, 6, and 8 with swirl vane angle d = 0, 45 and 70 degrees for each velocity ratio. Later experiments should include investigations into multiple jets located at the same axial location, as well as axially-staggered multiple jets.

REFERENCES

1. Schetz, J. A., "Injection and Mixing in Turbulent Flow." Prog. in Astro. and Aero., AIAA, Vol. 68, 1980.

2. Lefebvre, A. H. "Gas Turbine Combustion." McGraw-Hill, New York, 1983.

3. Gupta, A. K., Lilley, D. G., and Syred, N. "Swirl Flows." Abacus Press, Tunbridge Wells, England, 1984.

4. Gupta, A. K. and Lilley, D. G., "Flowfield Modeling and Diagnostics." Abacus Press, Tunbridge Wells, England, 1985.

5. Ferrell, G. B., "Deflected Jet Experiments in a Turbulent Combustor Flowfield." Ph.D. Thesis, Oklahoma State University, Stillwater, Okla., Dec. 1984. See also: Ferrell, G. B. and Lilley, D. G. "Deflected Jet Experiments in a Turbulent Combustor Flowfield." NASA CR-174863, May 1985.

6. Ferrell, G. B., Abujelala, M. T., Busnaina, A. A., Lilley, D. G., "Lateral Jet Injection into Typical Combustor Flowfields." AIAA Paper 84-0374, Reno, Nevada, Jan. 9-12, 1984.

7. Ferrell, G. B., Aoki, K. and Lilley, D. G. "Flow Visualization of Lateral Jet Injection into Swirling Crossflow." AIAA Paper 85-0059, Reno, Nevada, Jan. 14-17, 1985.

8. Ferrell, G. B. and Lilley, D. G. "Turbulence Measurements of Lateral Jet Injection into Confined Tubular Crossflow." Paper AIAA-85-1102, Monterey, Calif., July 8-10, 1985.

9. Ong, L. H., "Measurements of a Single Lateral Jet Injected into Swirling Crossflow." M.S. Thesis, Oklahoma State University, Stillwater, Okla., Dec. 1985.

10. Lilley, D. G., "Investigation of Flowfields Found in Typical Combustor Geometries." NASA CR-3869, Feb. 1985.

11. Lilley, D. G., "Swirling Flows in Typical Combustor Geometries." Paper AIAA-85-0184, Reno, Nevada, Jan. 14-17, 1985. See also: AIAA J. of Propulsion and Power, Vol. 2, 1986 (in press).

12. Chassaing, P., George, J., Claria, A., and Sananes, F., "Physical Characteristics of Subsonic Jets in a Cross-Stream." Journal of Fluid Mechanics, Vol. 62, 1974, p. 41-64.

13. Rathgeber, D. E., and Becker, H. A., "Mixing Between a Round Jet and a Transverse Pipe Flow." Proceedings of 1st Symposium on Turbulent Flows, Penn State University, 1977, pp. 10.17-10.26.

14. Crabb, D., Durao, D. F. G., and Whitelaw, J. W., "A Round Jet Normal to a Cross-Flow." ASME Trans., J. of Fluids Engr., Vol. 103, 1981, pp. 142.153.

15. Holdeman, J. D., Srinivasan, R., and Berenfeld, A., "Experiments in Dilution Jet Mixing." AIAA Journal, Vol. 22, No. 10, Oct. 1984, pp. 1436-1443.

16. Morel, T., "Comprehensive Design of Axisymmetric Wind Tunnel Contractions." ASME Paper 75-FE-17, Minneapolis, MN, May 5-7, 1975.

17. Merzkirch, W., "Flow Visualization." Academic Press, New York and London, 1974, pp. 191-196.

18. Janjua, S. I., "Turbulence Measurements in a Complex Flowfield Using a Six-Orientation Hot-Wire Probe Technique." M.S. Thesis, Oklahoma State University, Stillwater, Okla., Dec. 1981.

19. Jackson, T. W., "Turbulence Characteristics of Swirling Flowfields." Ph.D. Thesis, Oklahoma State University, Stillwater, OK, Dec. 1983. See also: Jackson, T. W. and Lilley, D. G. "Turbulence Characteristics of Swirling Flowfields." NASA CR-174918, May 1985.

20. Scharrer, G. L., "Swirl, Expansion Ratio and Blockage Effects on Continued Turbulent Flow." M. S. Thesis, Oklahoma State University, Stillwater, Okla. May 1984.

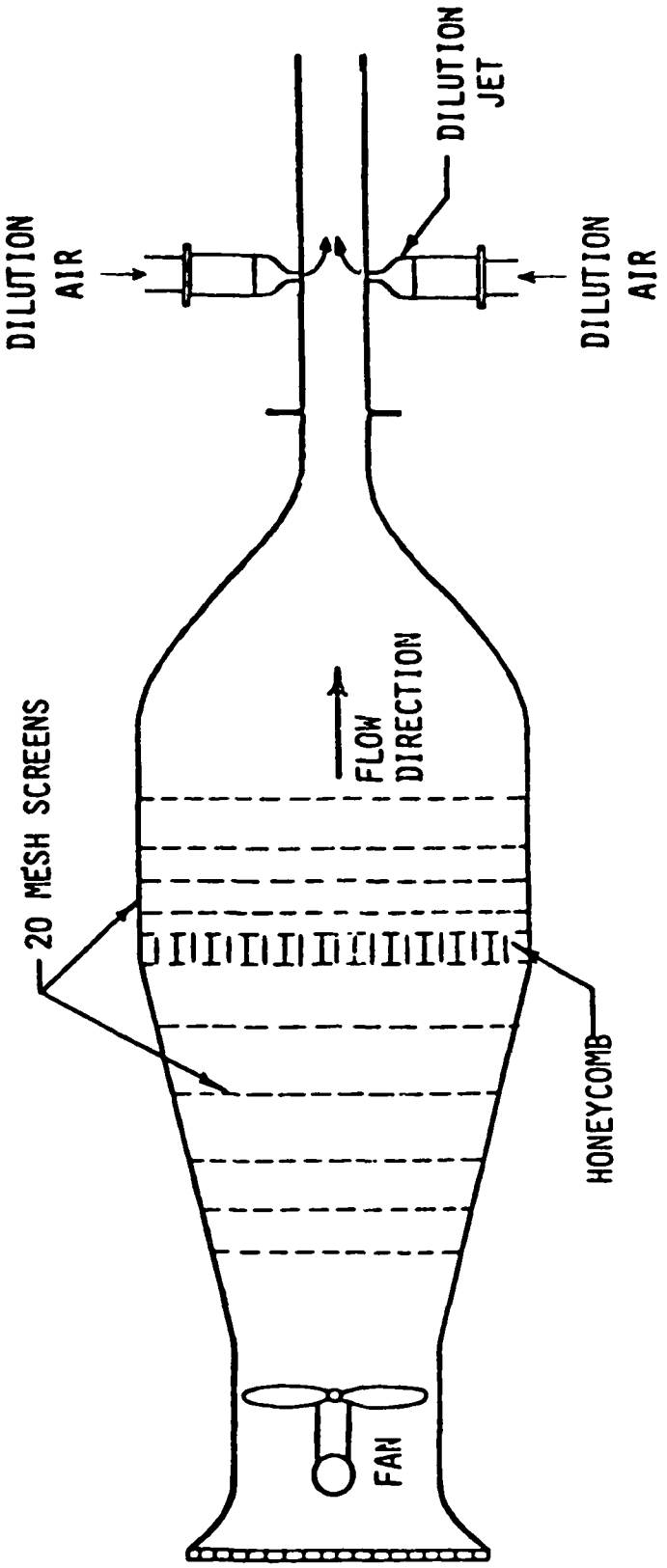

Figure 1. Schematic of Experimental Facility

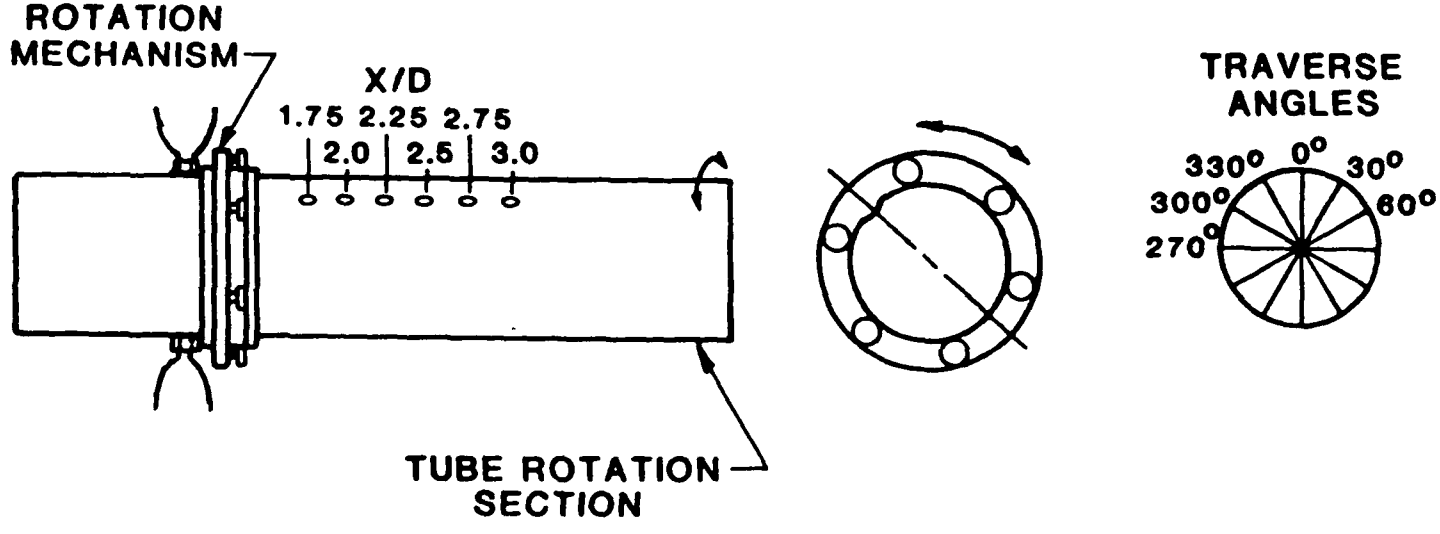

Figure 2. Test Section.

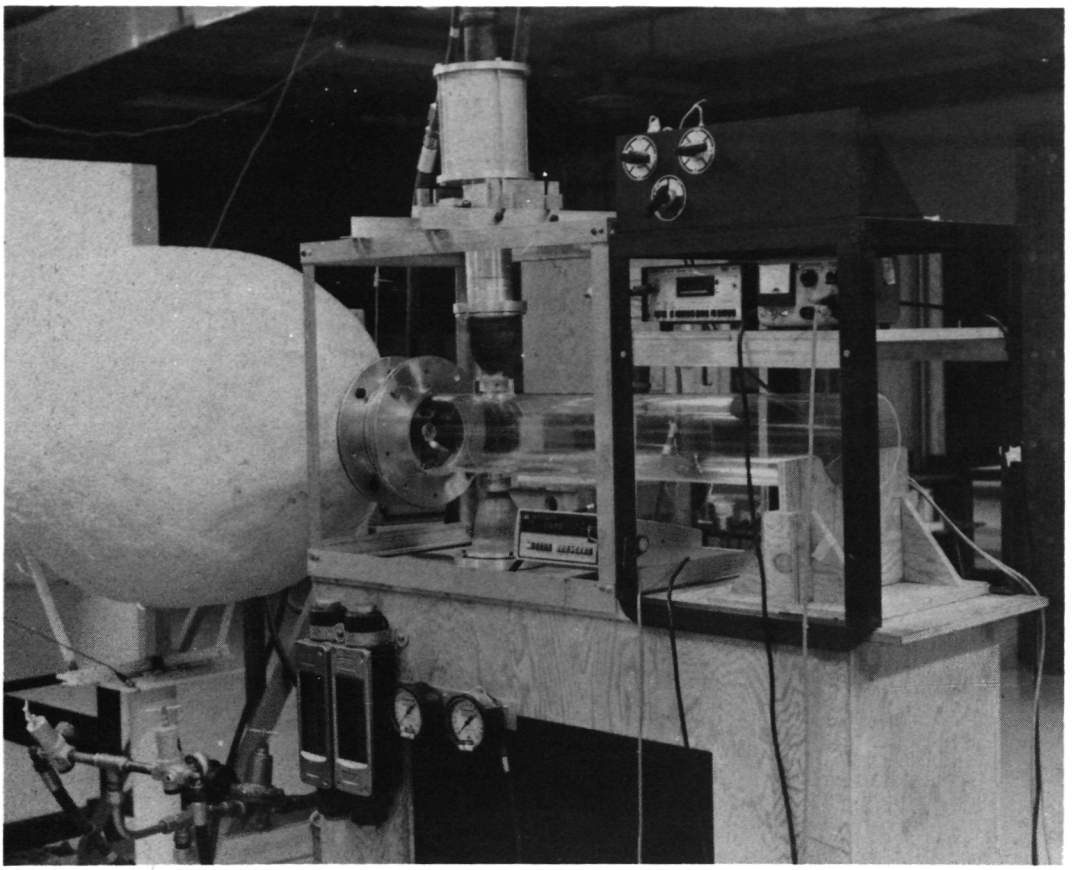

Figure 3. Dilution Jets Mounted on Test Section.

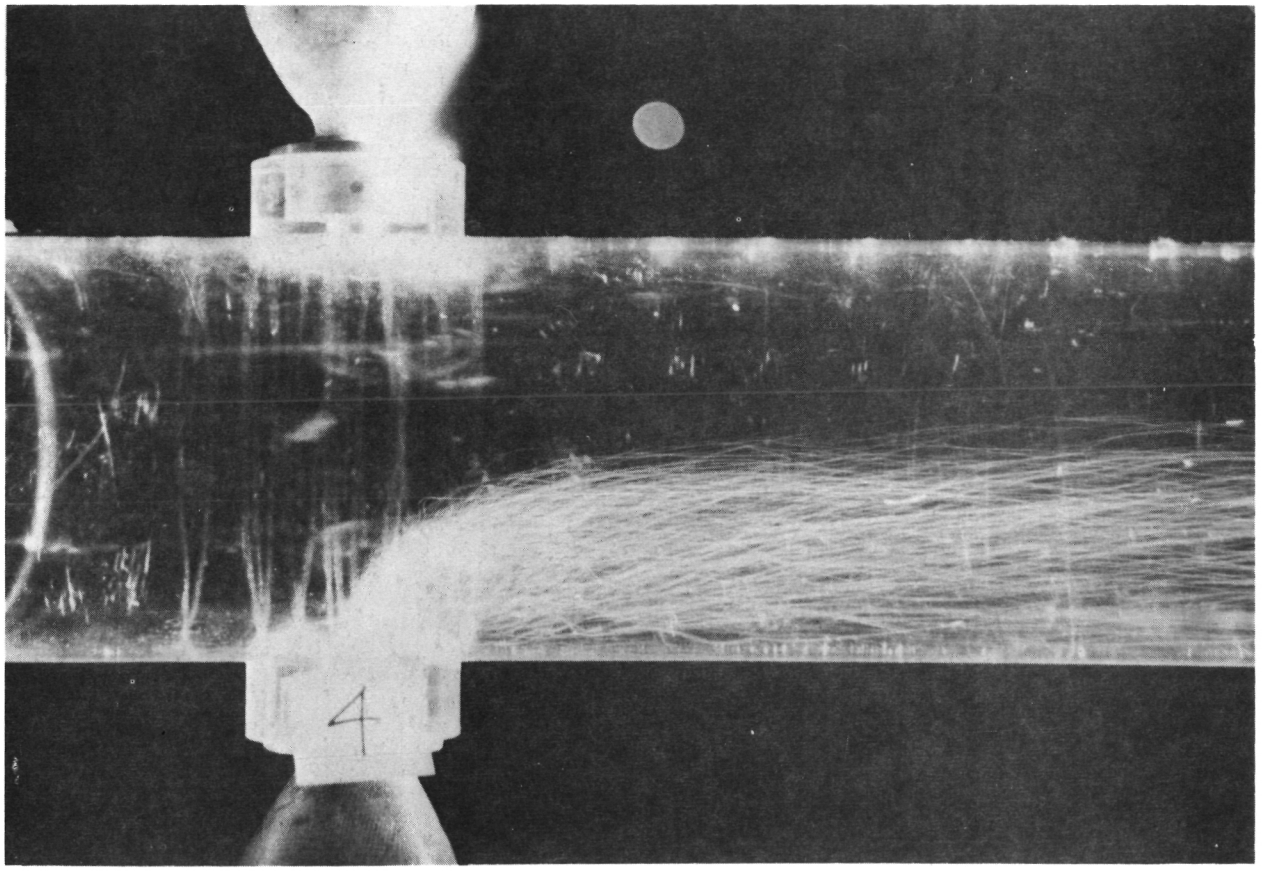

a) Swirl Vane Angle ϕ = 0 Degrees (Swirler Removed).

Figure 4. Bubble Flow Visualization for Jet to Crossflow Velocity Ratio R = 4, Swirl Vane Angle ϕ = 0 (Swirler Removed), 45 and 70 Degrees.

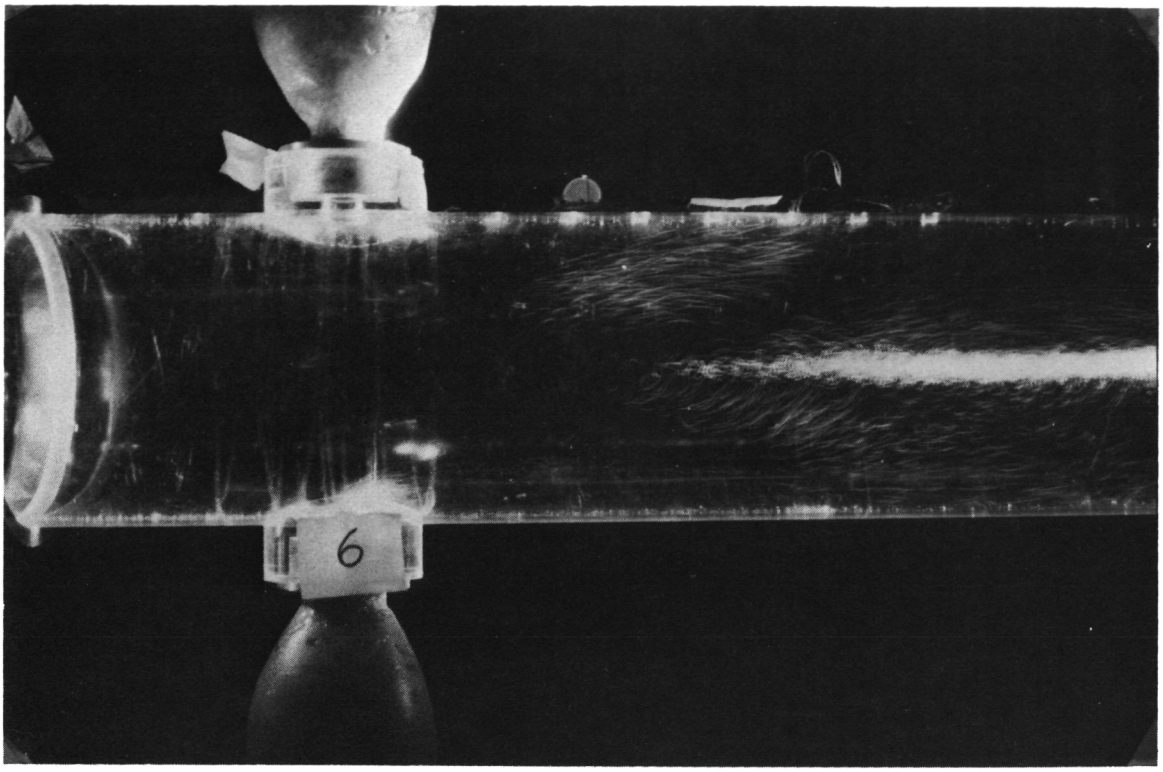

b) Swirl Vane Angle ϕ = 45 Degrees.

Figure 4. (Continued)

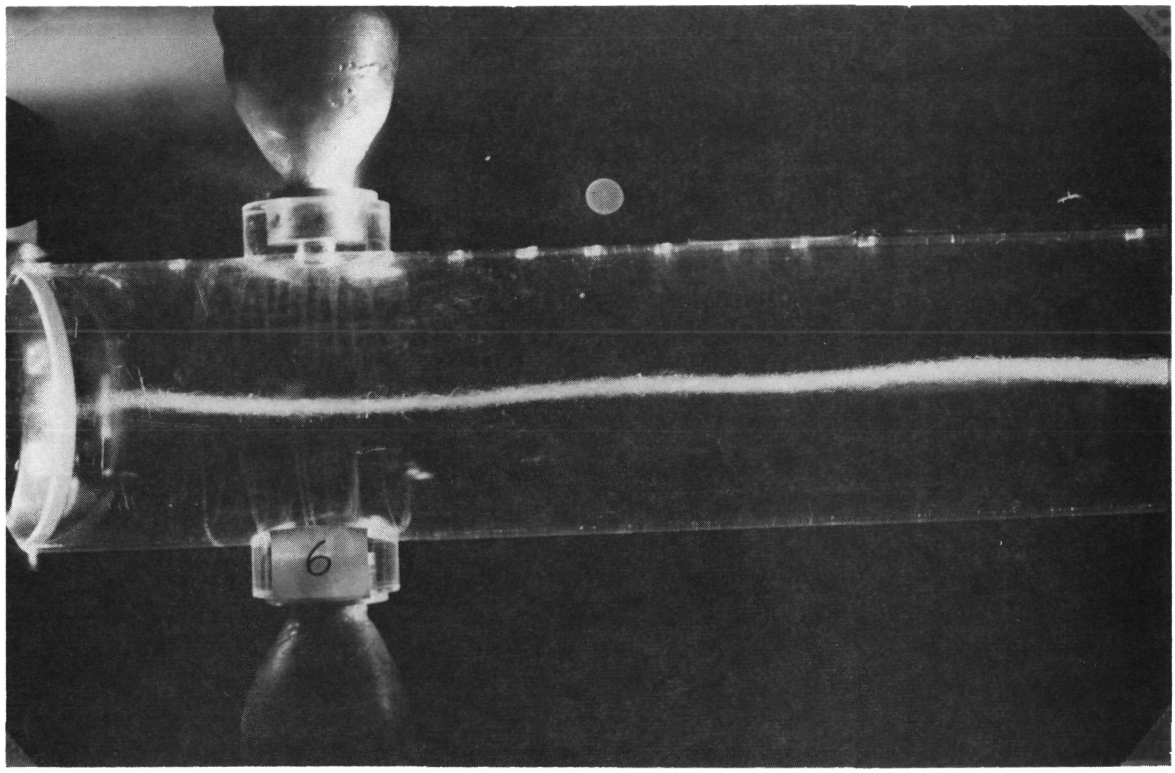

c) Swirl Vane Angle ϕ = 70 Degrees.

Figure 4. (Continued)

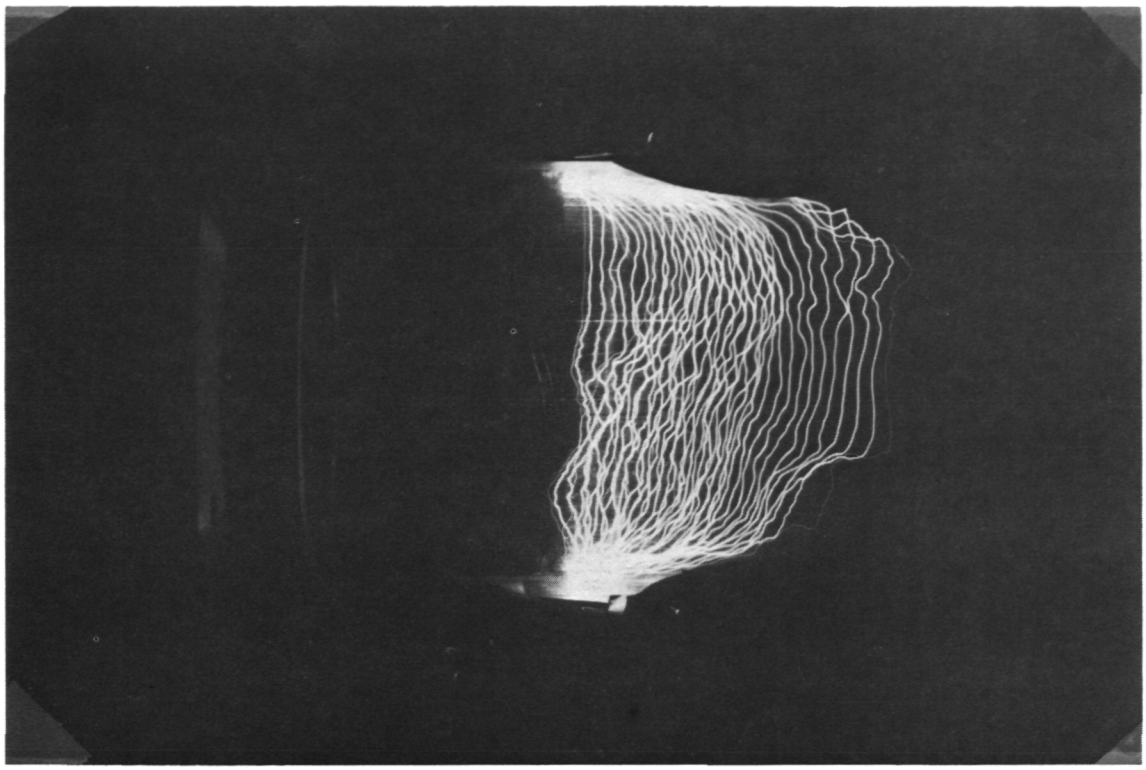

a) x/D = 0.5

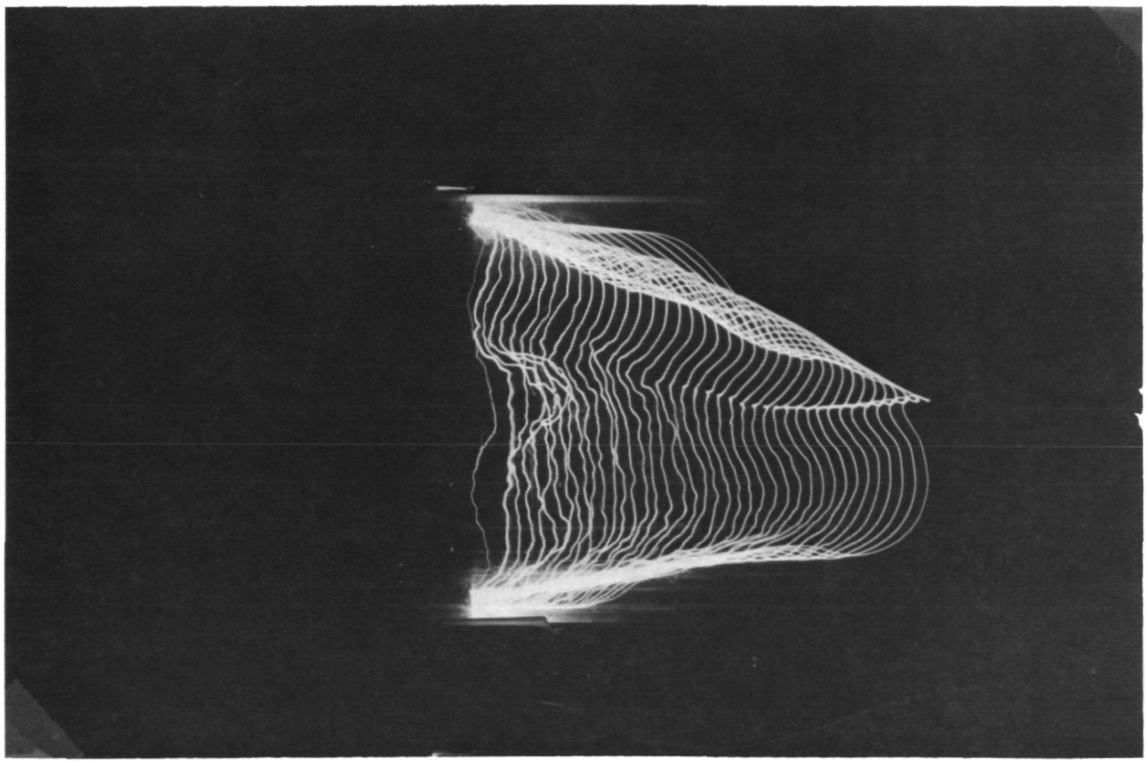

b) x/D = 1.5

Figure 5. Spark Flow Visualization for Jet to Crossflow Velocity Ratio R = 4, Swirl Vane Angle ϕ = 0 Degrees.

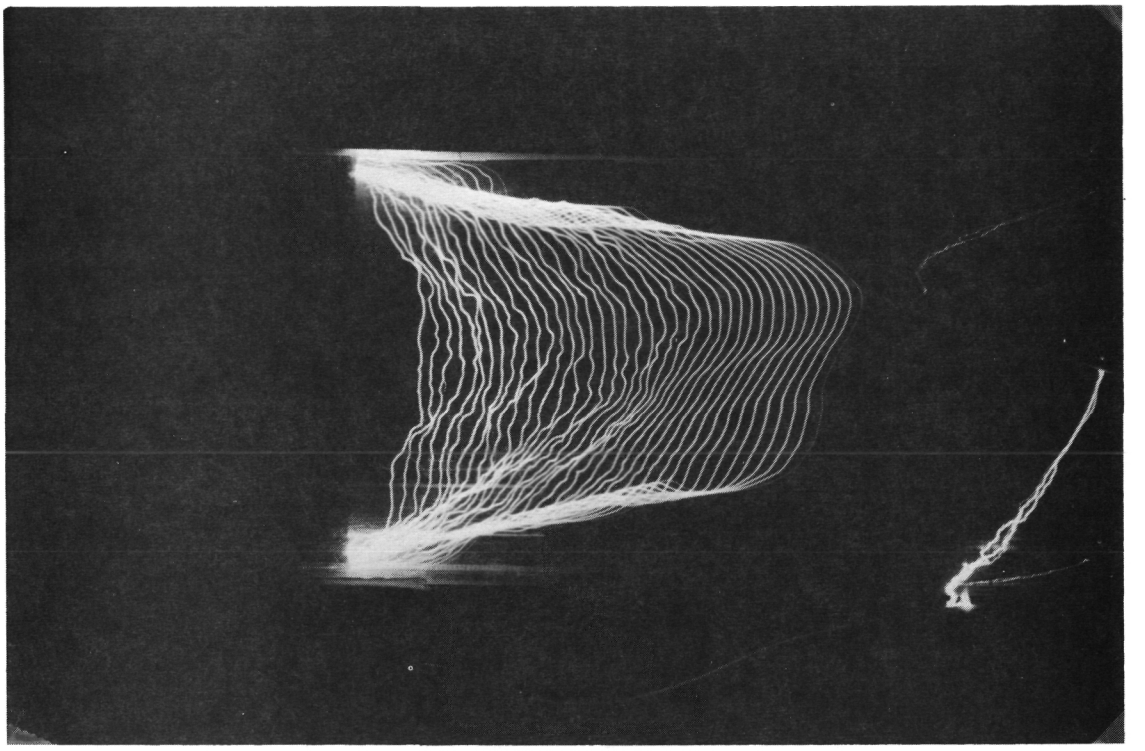

c) x/D = 2.0

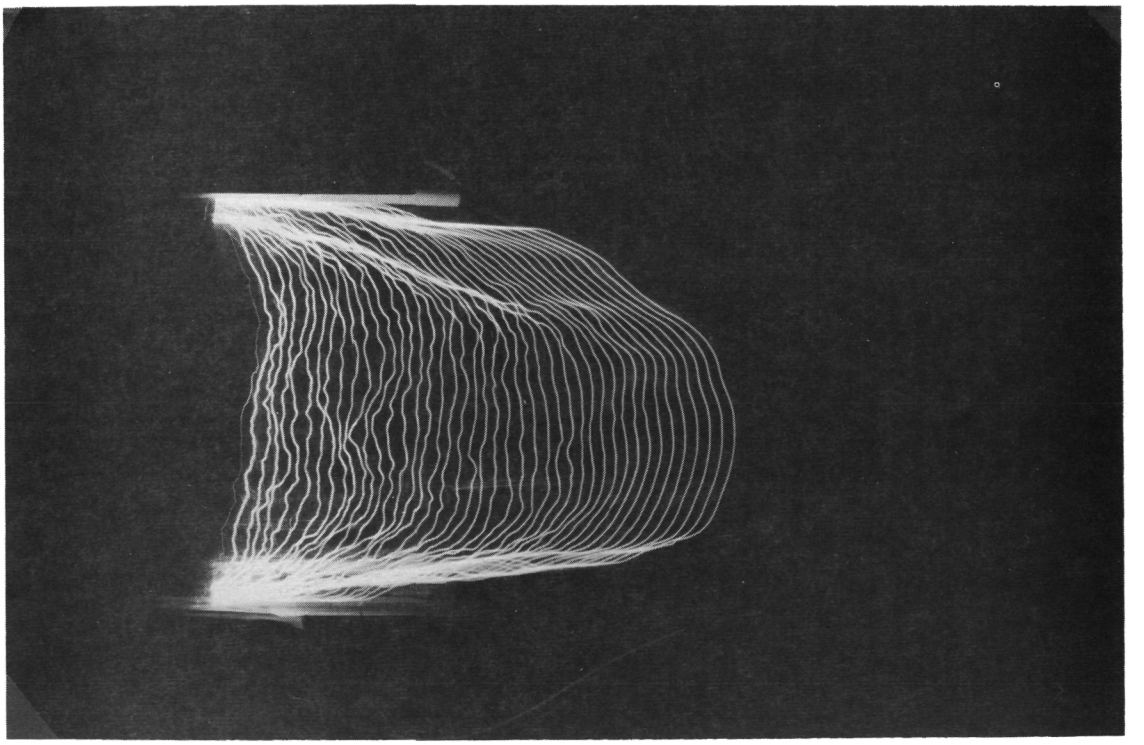

d) x/D = 2.5

Figure 5. (Continued)

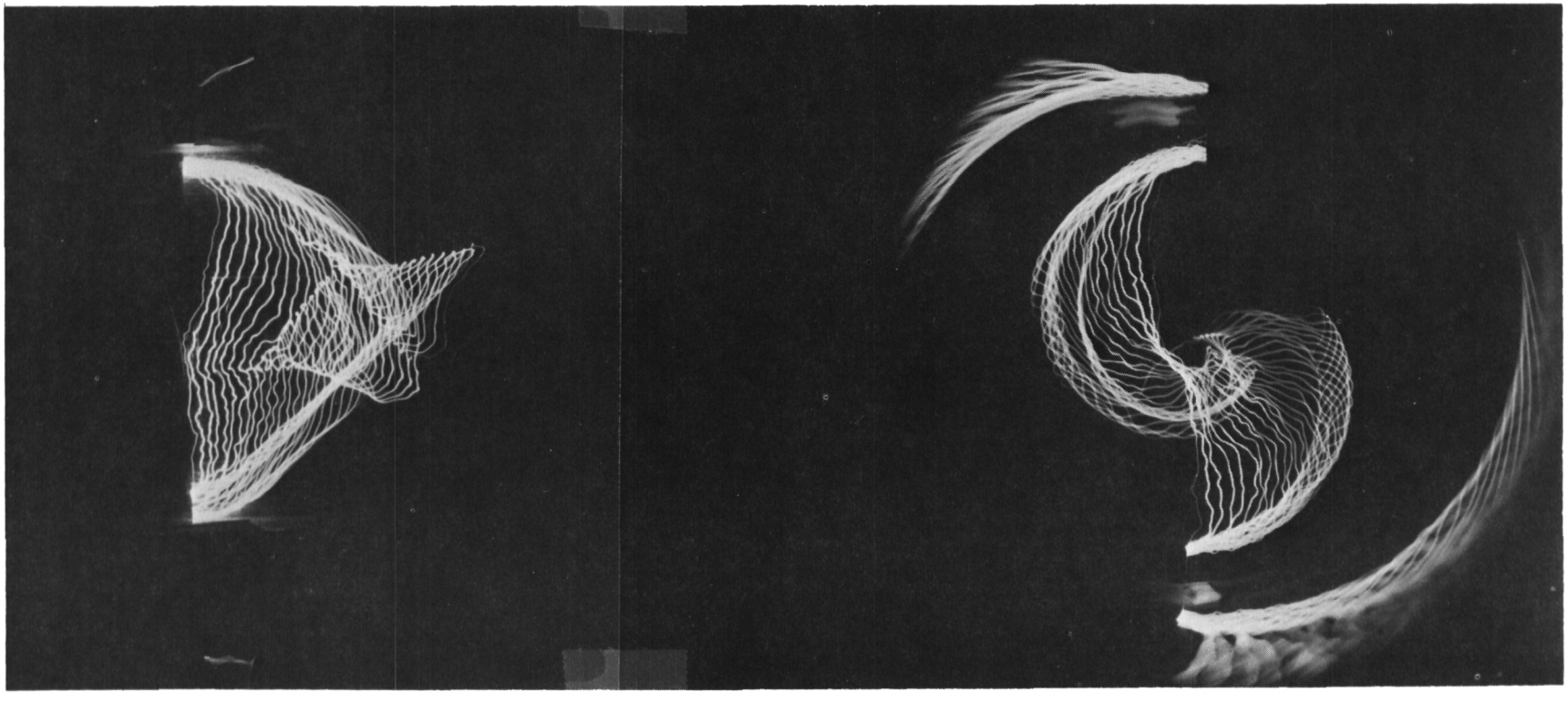

(a) x/D = 0.5

Figure 6. Spark Flow Visualization for Jet to Crossflow Velocity Ratio R = 4, Swirl Vane Angle ϕ = 45 Degrees.

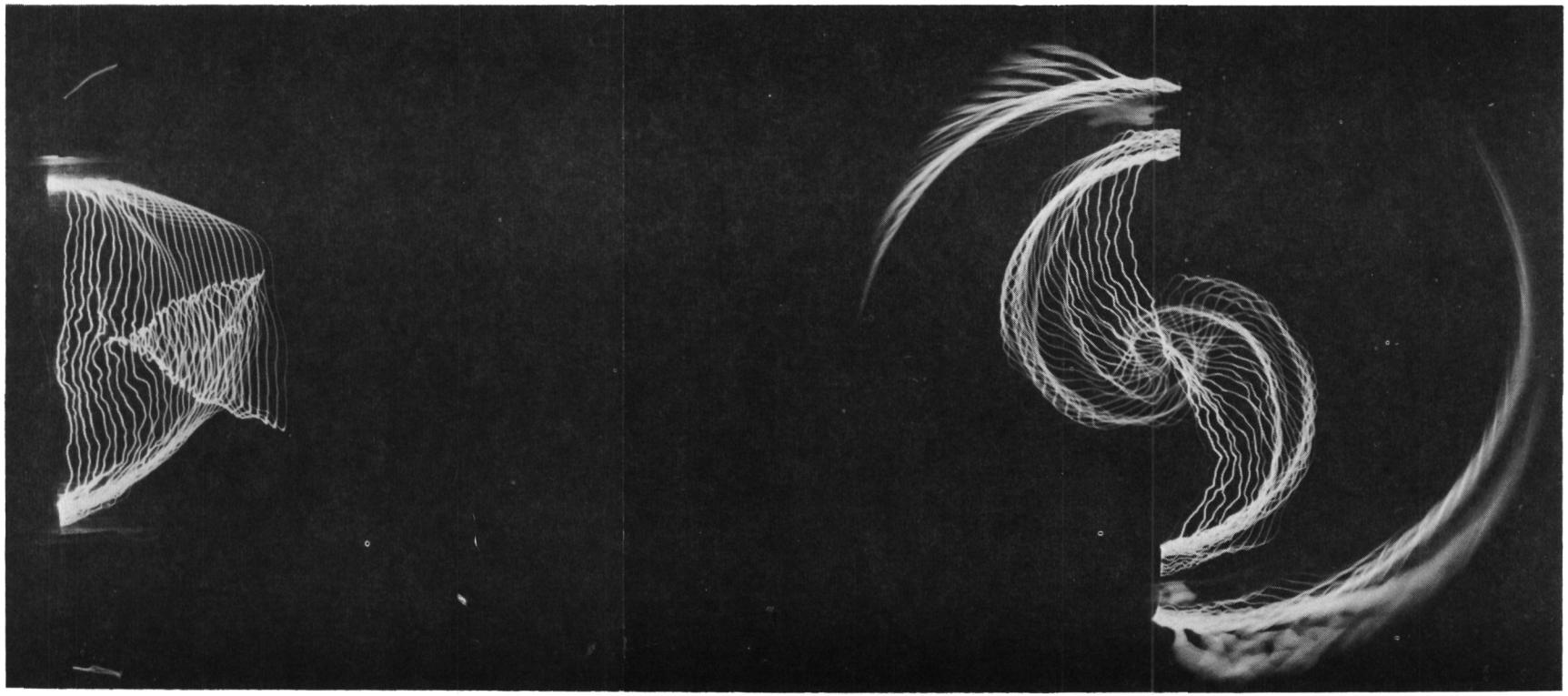

(b) x/D = 1.5

Figure 6. (Continued)

(c) x/D = 2.0

Figure 6. (Continued)

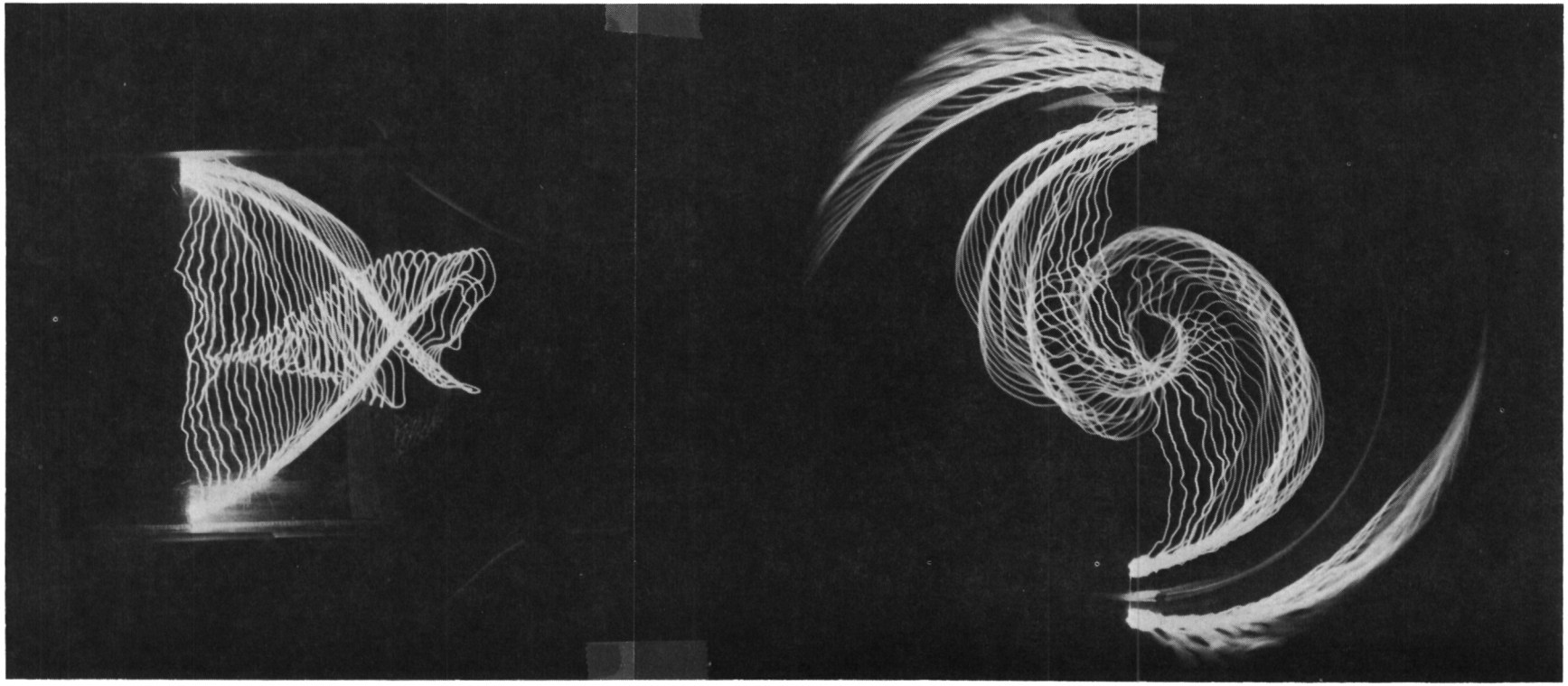

(d) x/D = 2.5

Figure 6. (Continued)

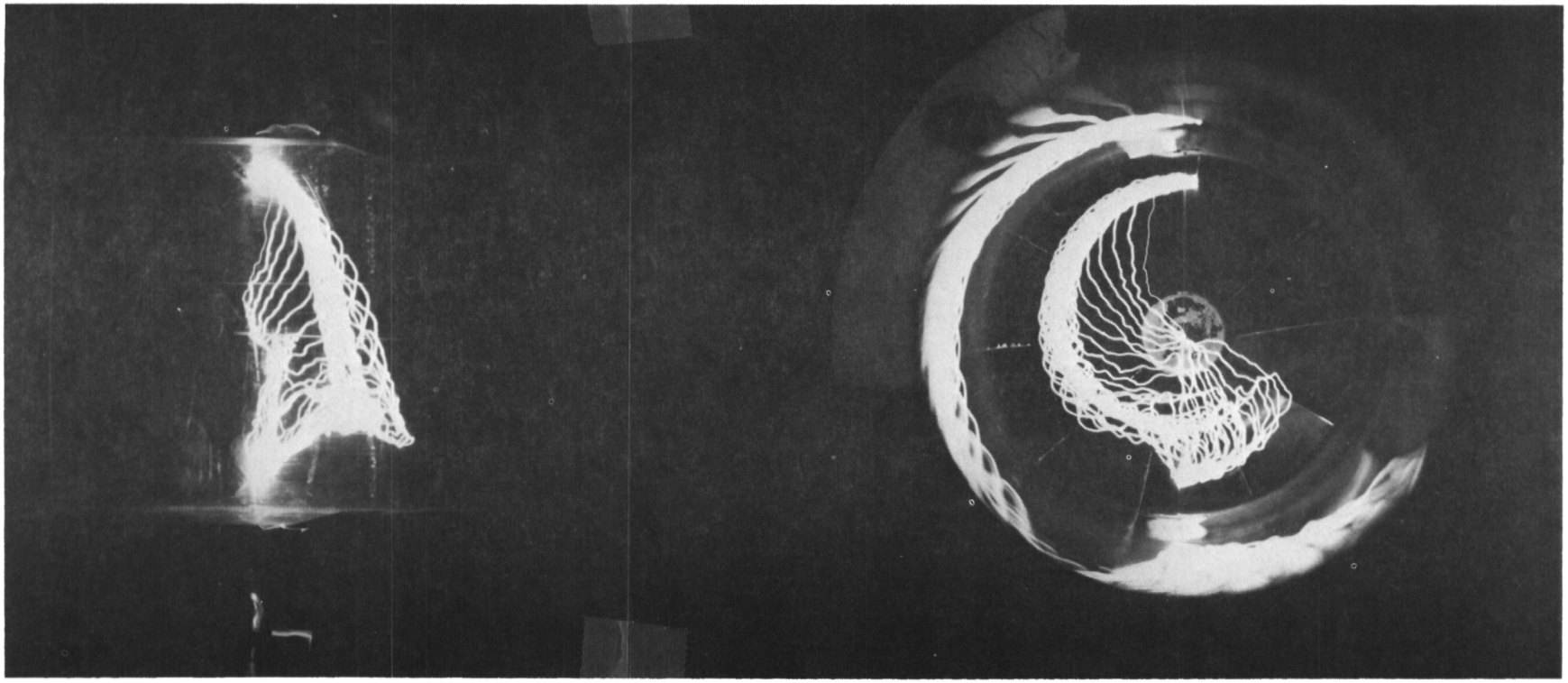

(a) x/D = 0.5

Figure 7. Spark Flow Visualization for Jet to Crossflow Velocity Ratio R = 4, Swirl Vane Angle ϕ = 70 Degrees.

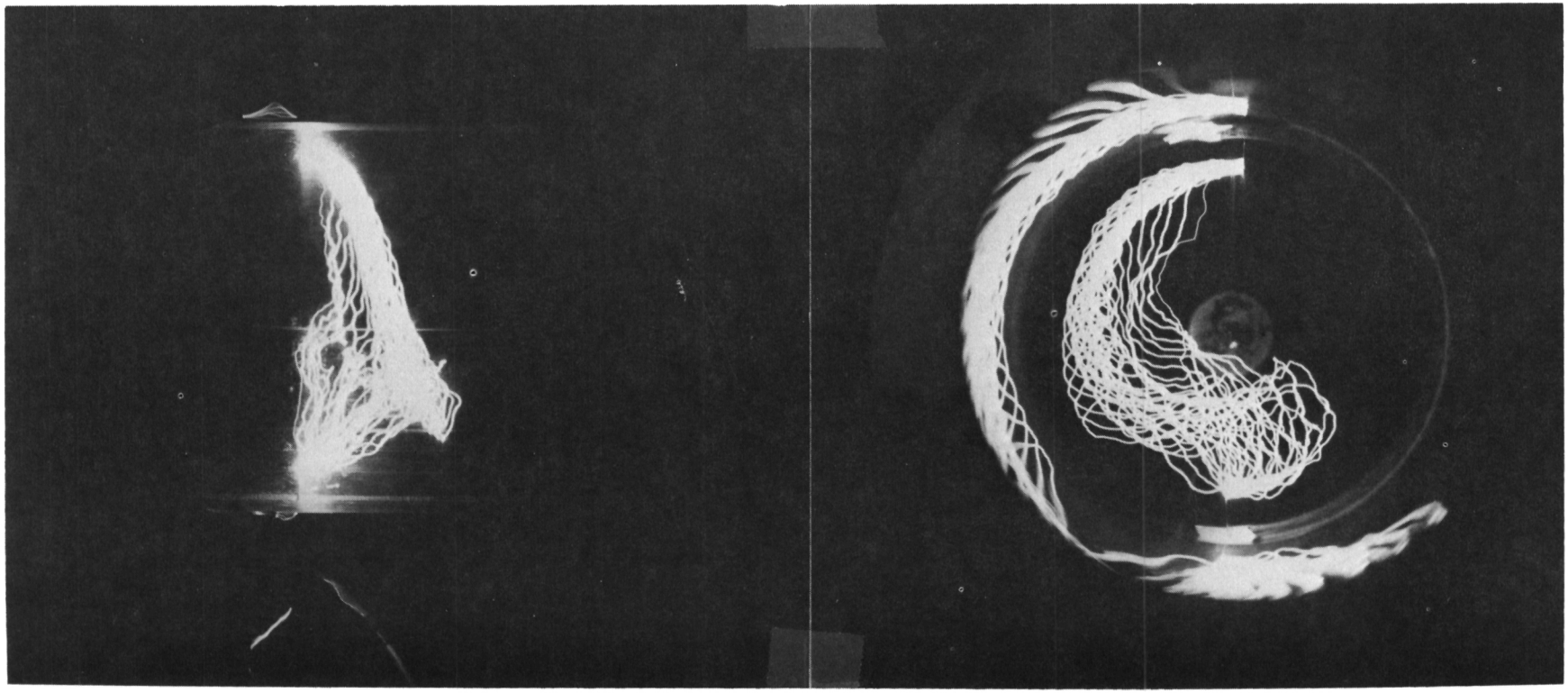

(b) x/D = 1.5

Figure 7. (Continued)

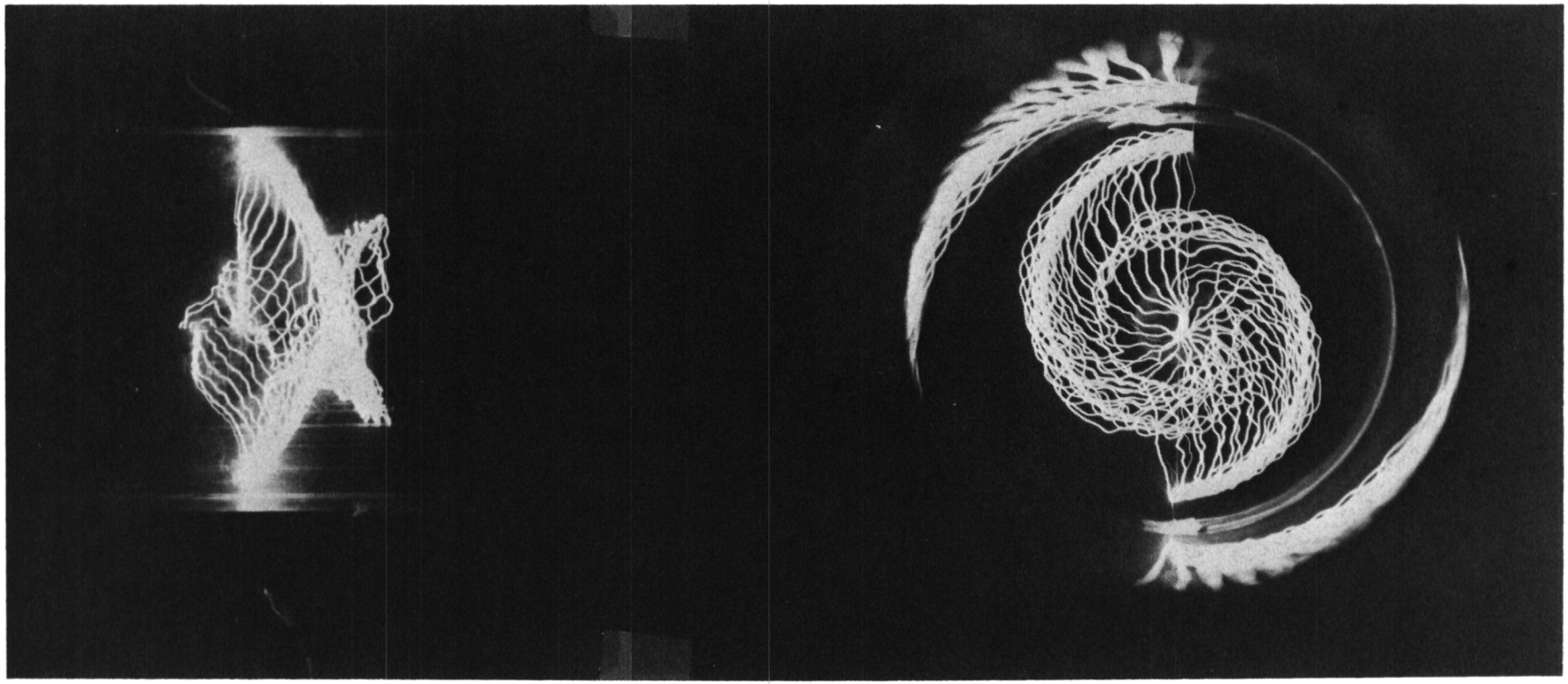

(c) x/D = 2.0

Figure 7. (Continued)

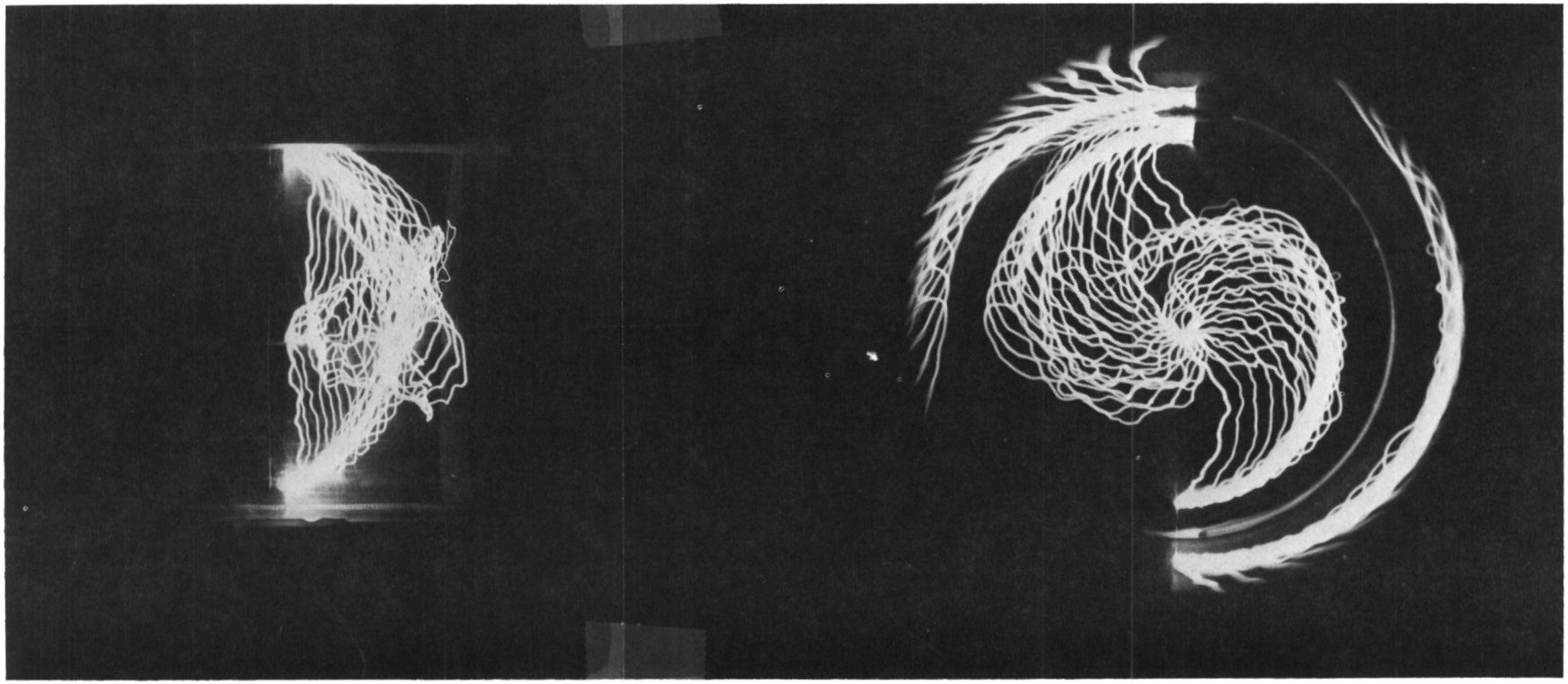

(d) x/D = 2.5

Figure 7. (Continued)

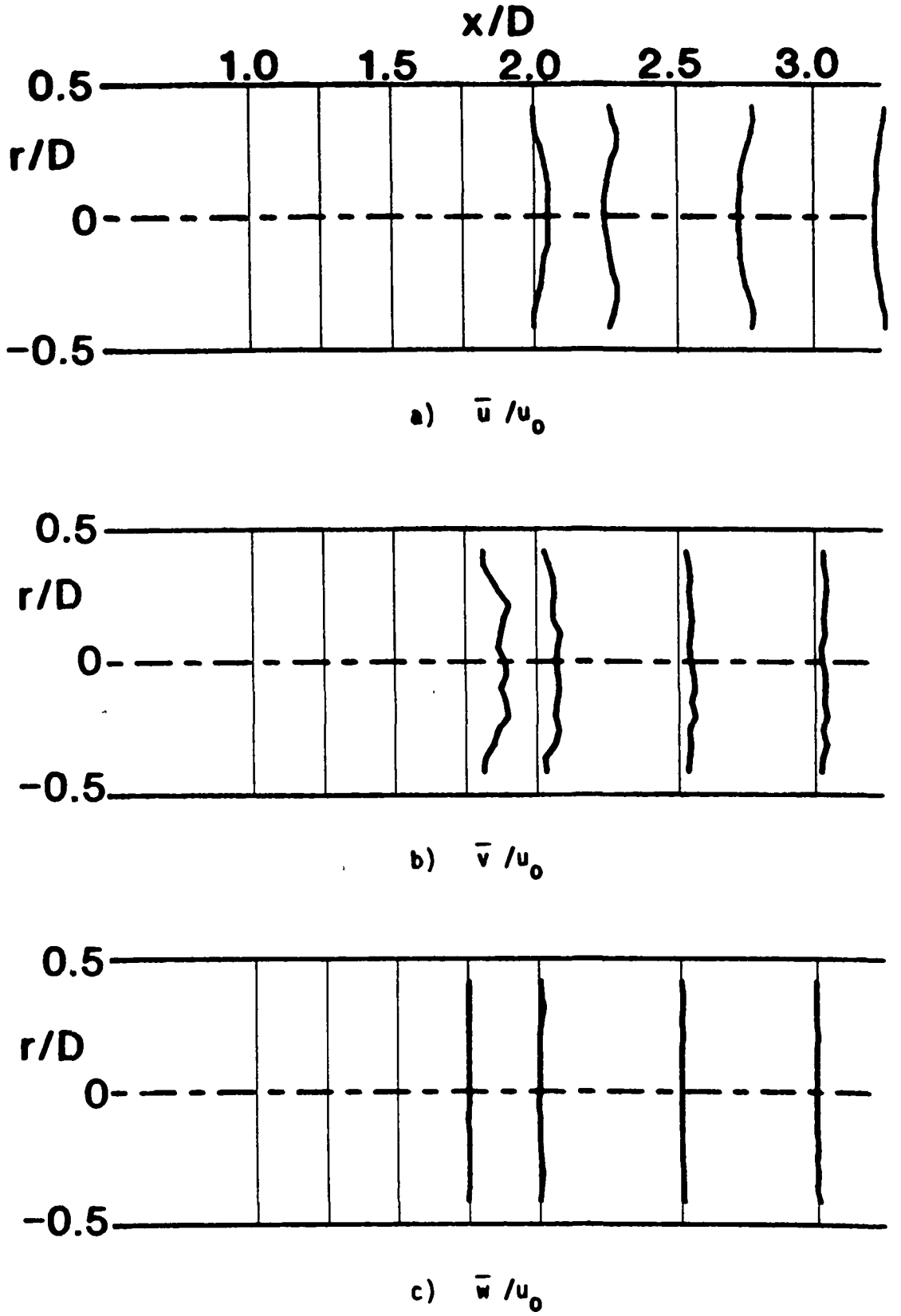

Figure 8. Time-Mean and Turbulent Flowfield, R = 4, ϕ = 0 Degrees (Swirler Removed), Traverse Angle θ = 270 Degrees.

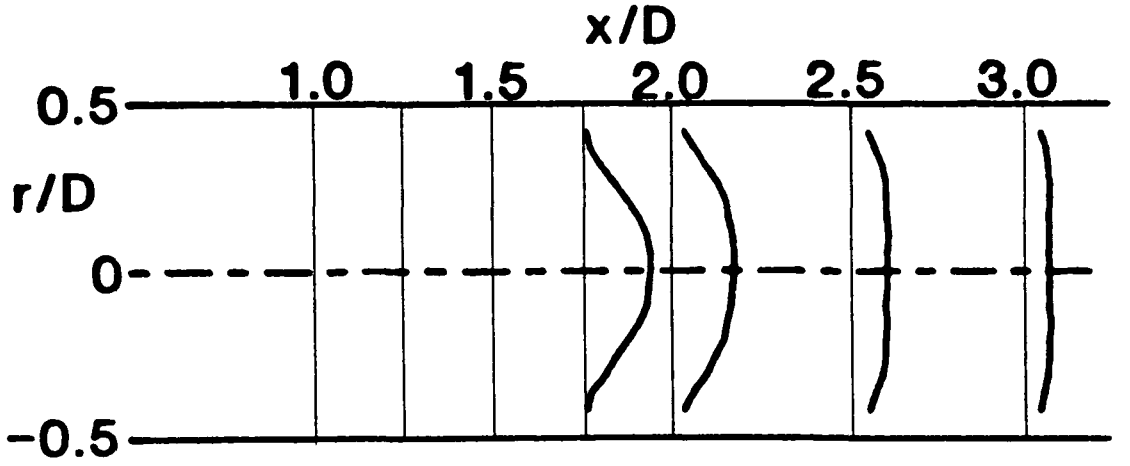

d) u'_{rms}/u_o x 2

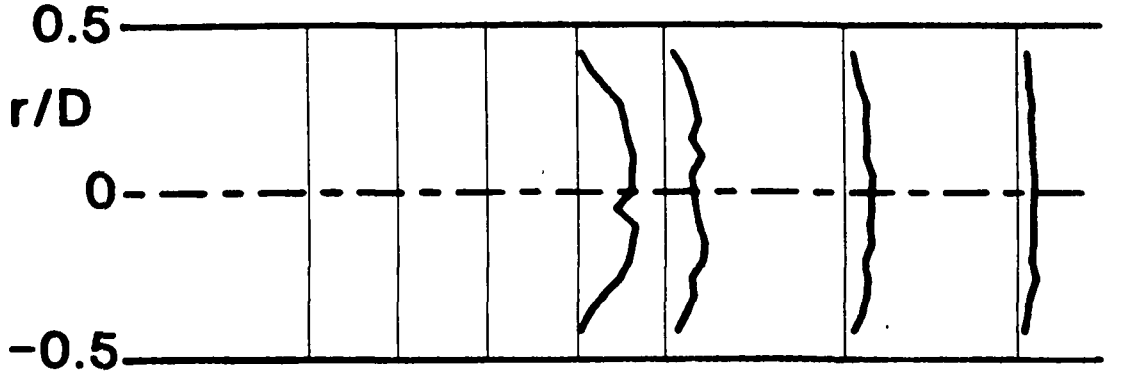

e) v'_{rms}/u_o x 2

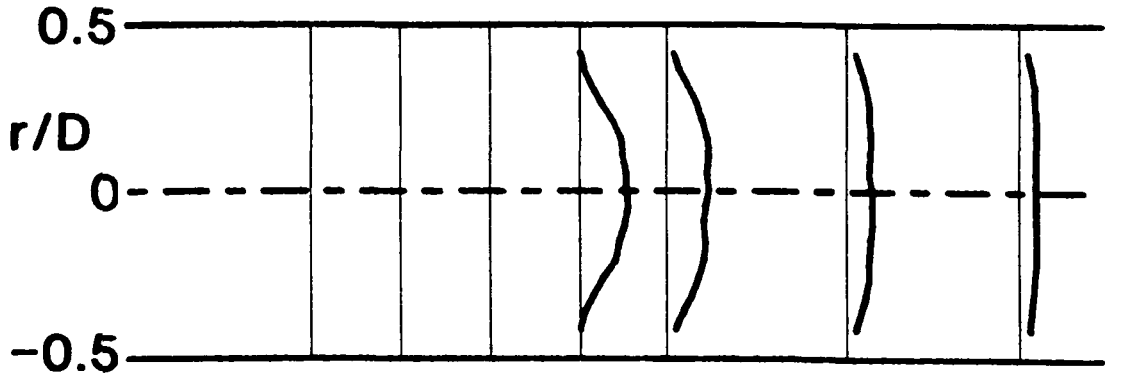

f) w'_{rms}/u_o x 2

Figure 8. (Continued)

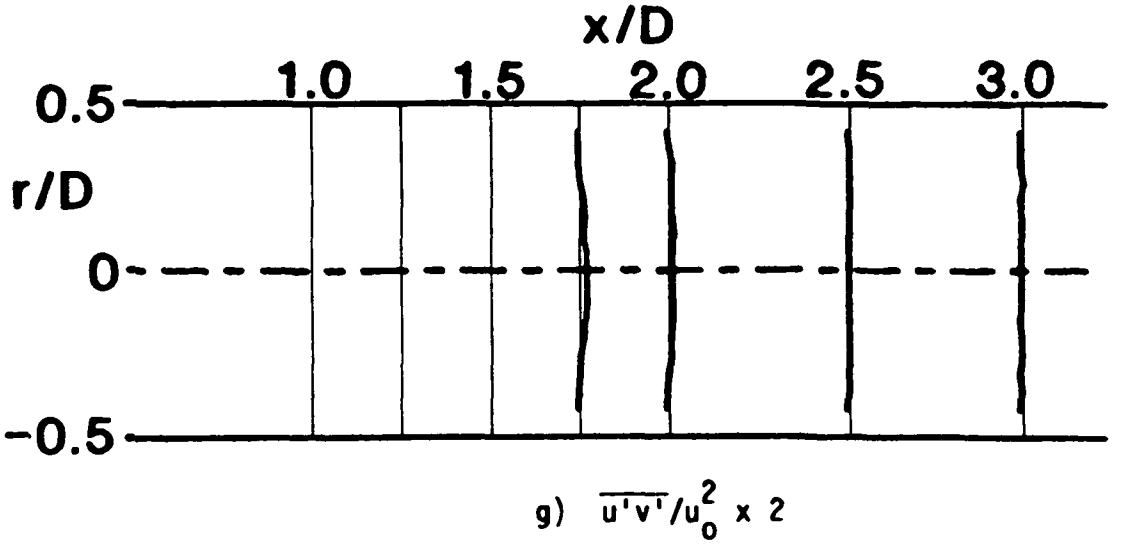

g) $\overline{u'v'}/u_0^2 \times 2$

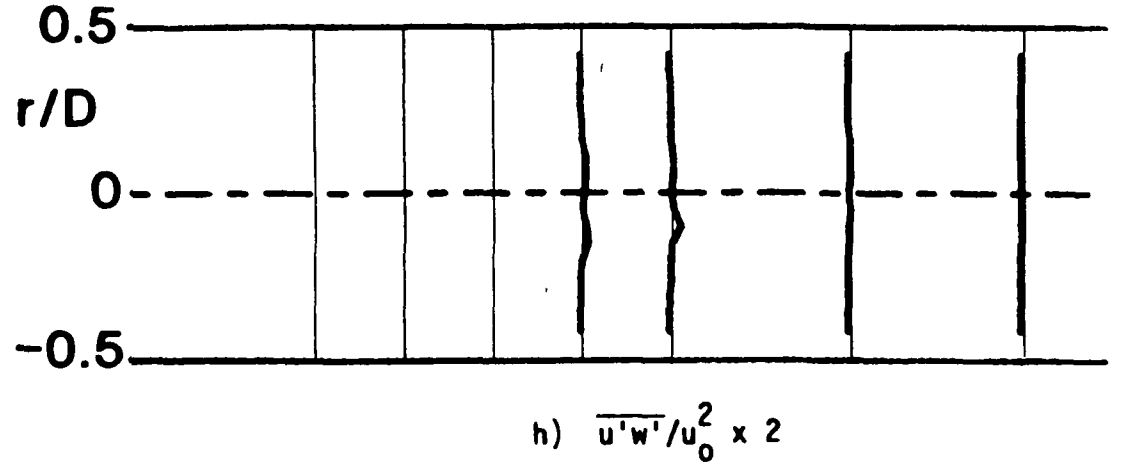

h) $\overline{u'w'}/u_0^2 \times 2$

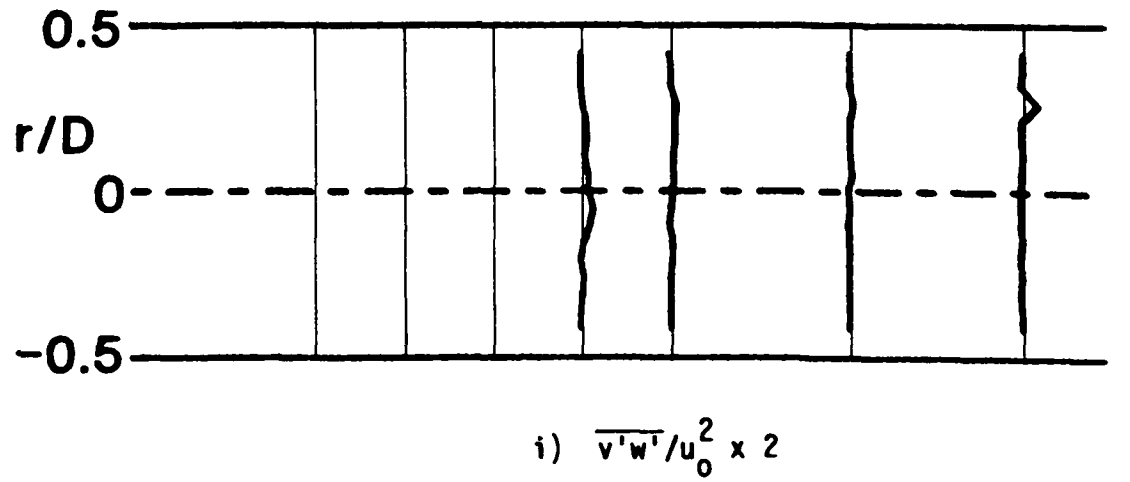

i) $\overline{v'w'}/u_0^2 \times 2$

Figure 8. (Continued)

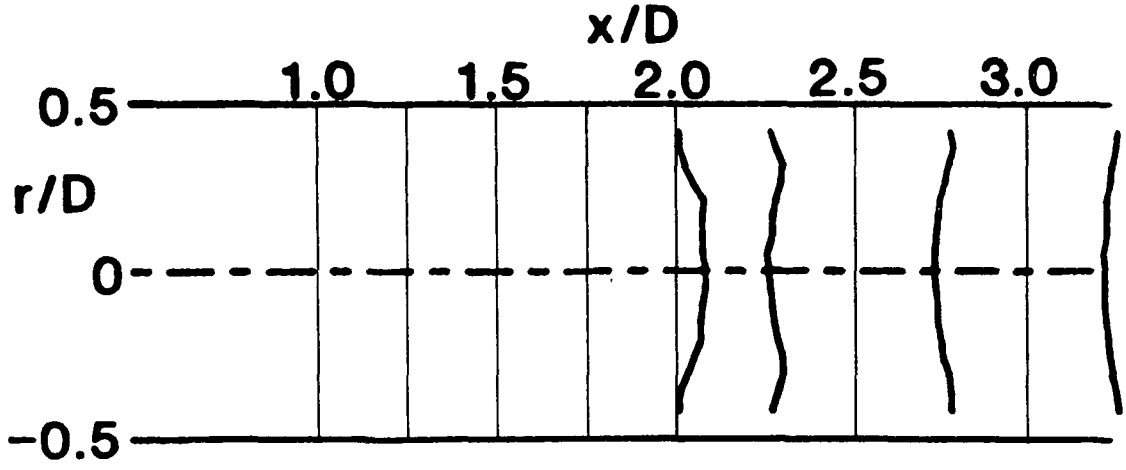

j) $\bar{V} = (\bar{u}^2 + \bar{v}^2 + \bar{w}^2)^{1/2}/u_o$

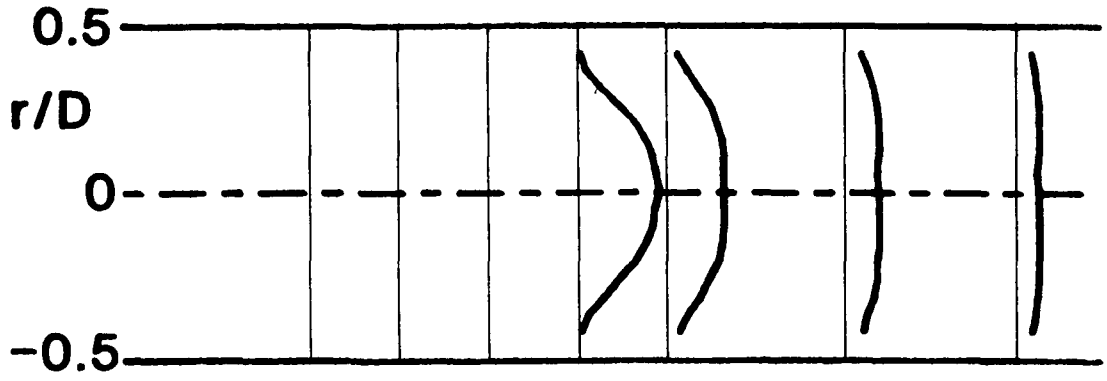

k) $u'_{rms}/\bar{u} \times 2$

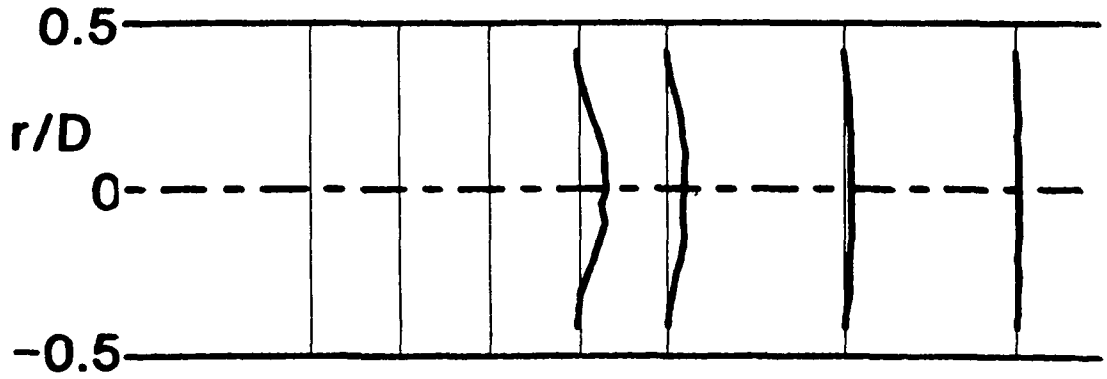

l) $\frac{1}{2}(u'^2_{rms} + v'^2_{rms} + w'^2_{rms})/u_o^2 \times 2$

Figure 8. (Continued)

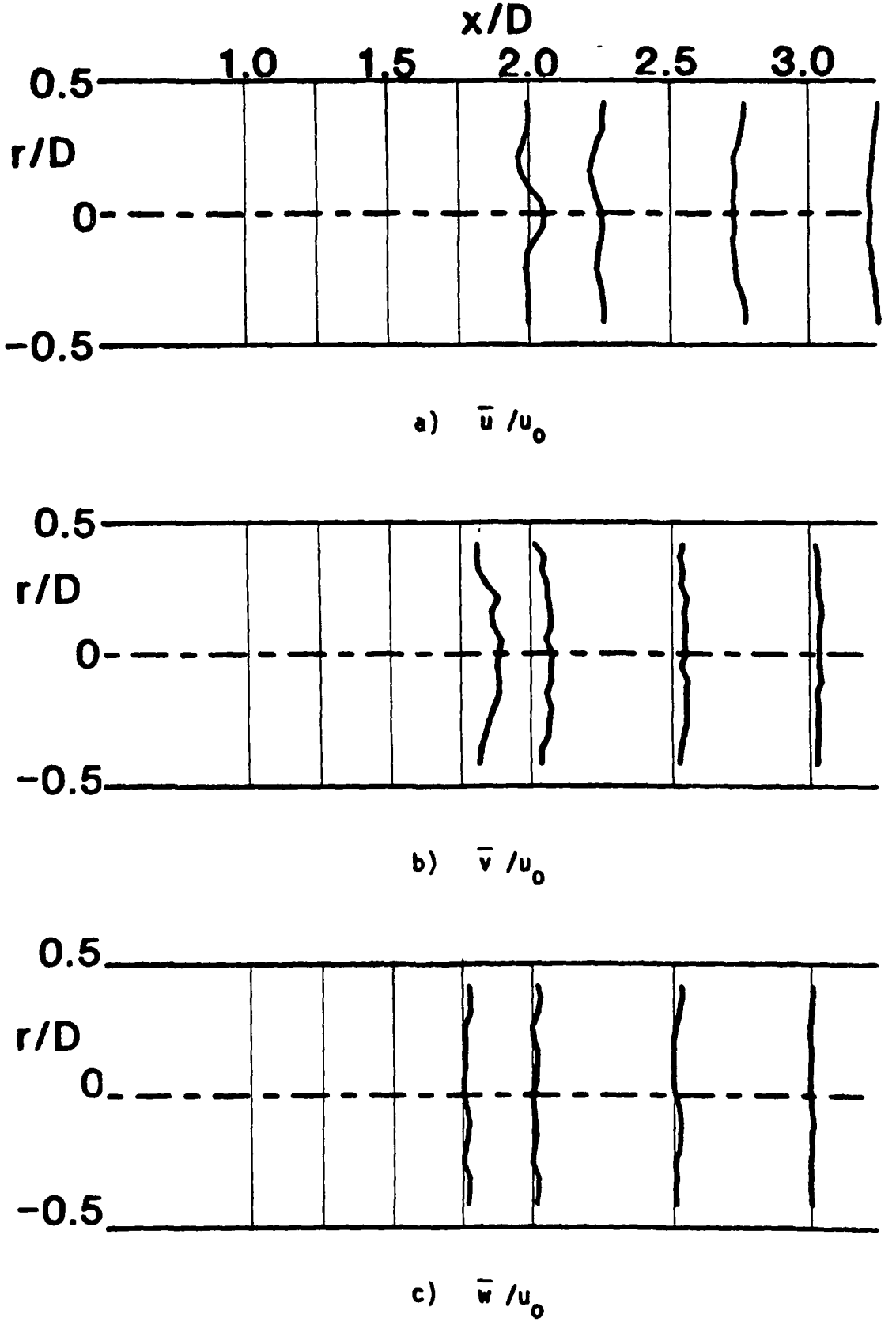

Figure 9. Time-Mean and Turbulent Flowfield, R = 4, ϕ = 0 Degrees (Swirler Removed), Traverse Angle θ = 300 Degrees.

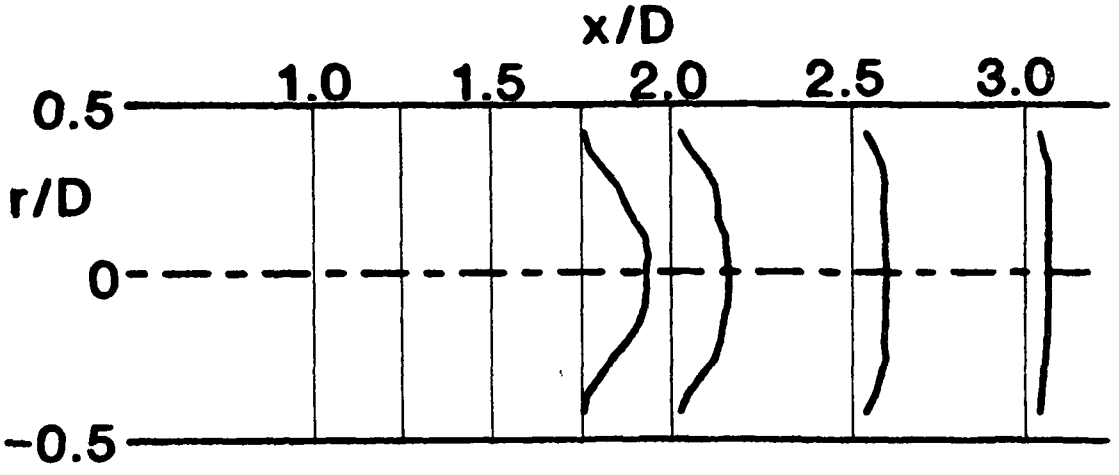

d) $u'_{rms}/u_o \times 2$

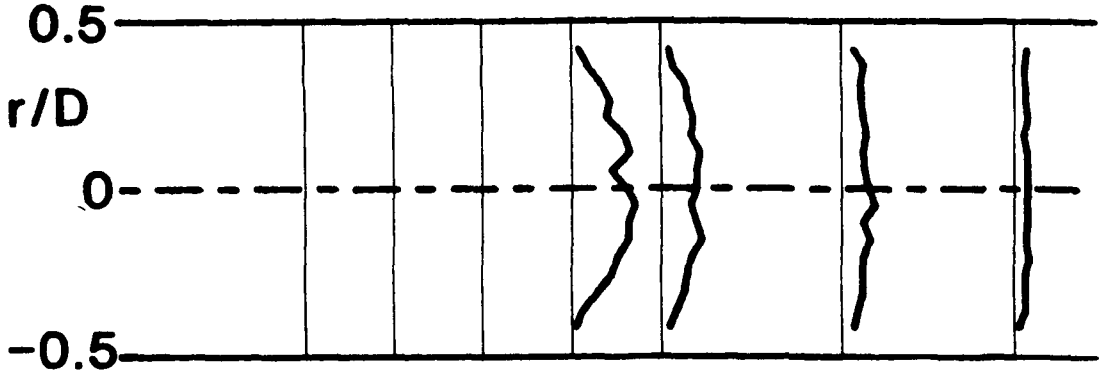

e) $v'_{rms}/u_o \times 2$

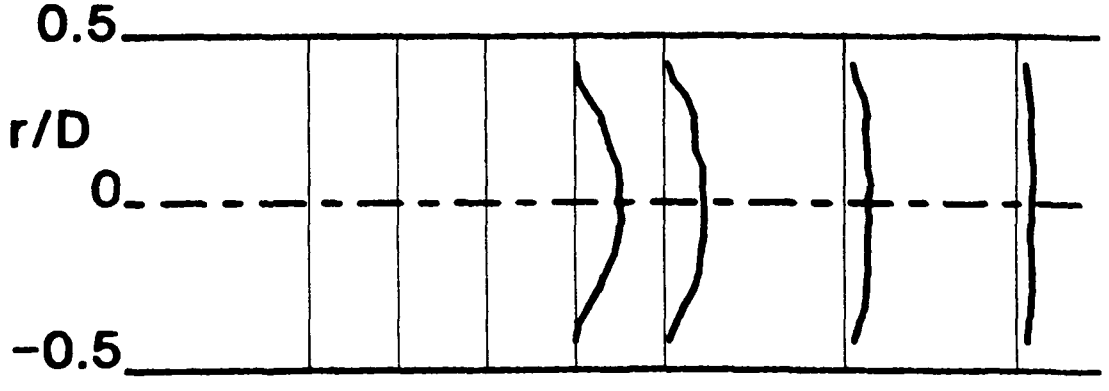

f) $w'_{rms}/u_o \times 2$

Figure 9. (Continued)

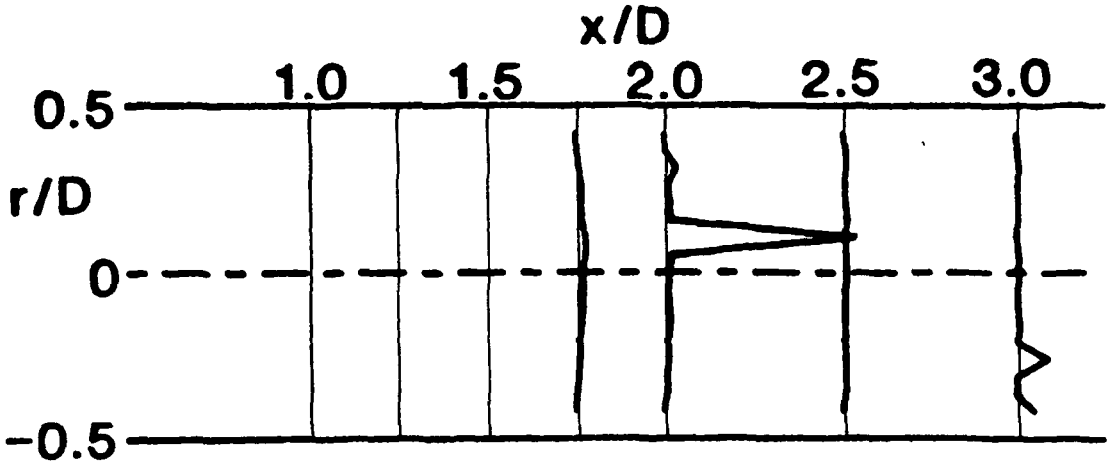

g) $\overline{u'v'}/u_o^2 \times 2$

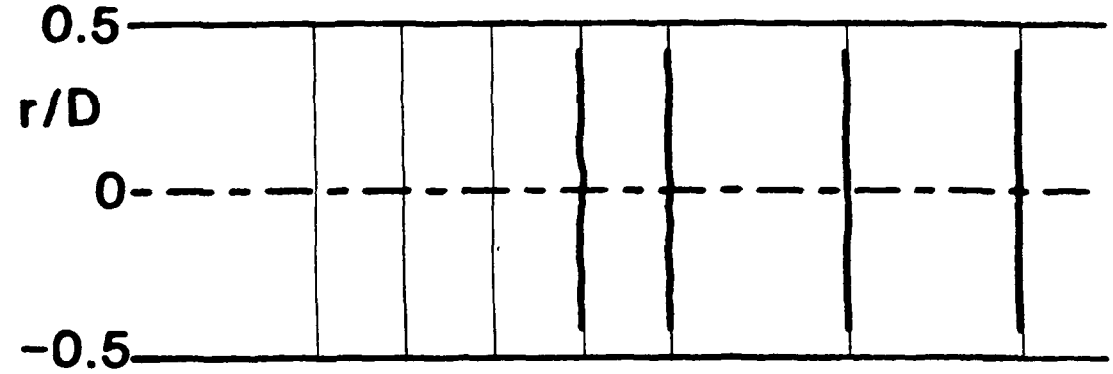

h) $\overline{u'w'}/u_o^2 \times 2$

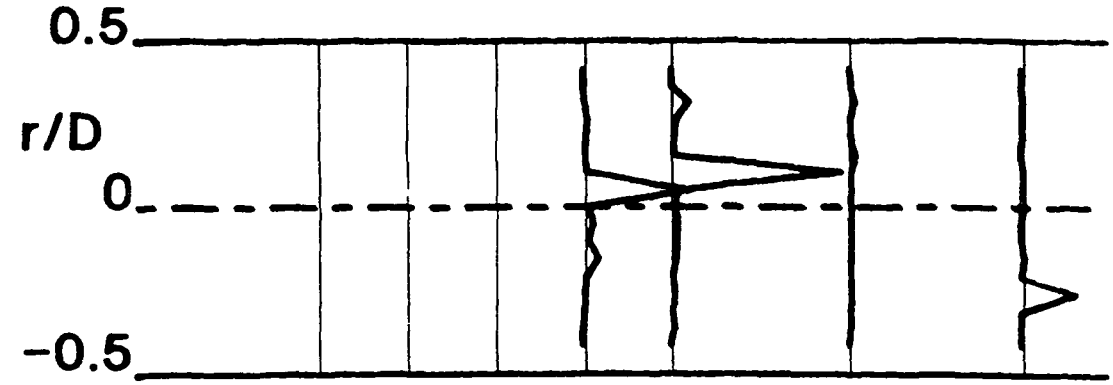

i) $\overline{v'w'}/u_o^2 \times 2$

Figure 9. (Continued)

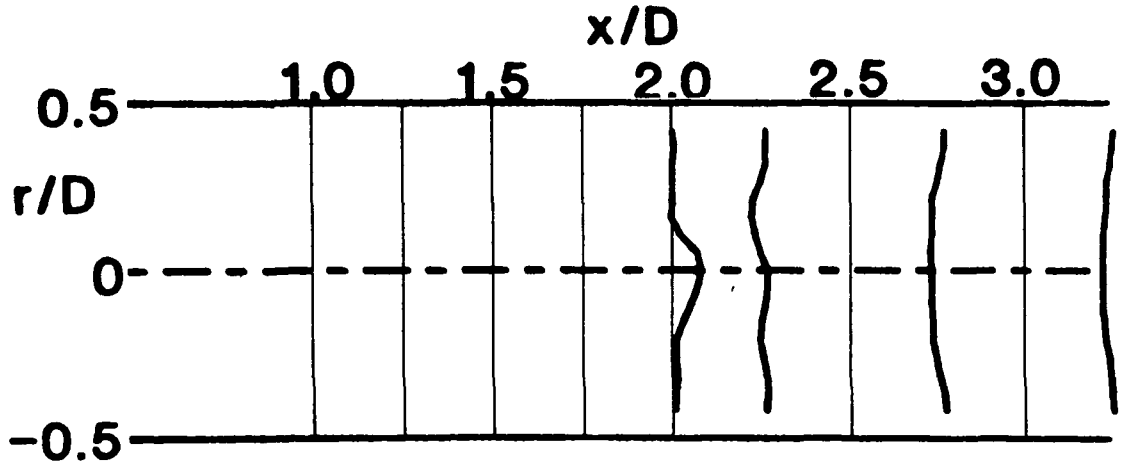

j) $\bar{V} = (\bar{u}^2 + \bar{v}^2 + \bar{w}^2)^{1/2}/u_o$

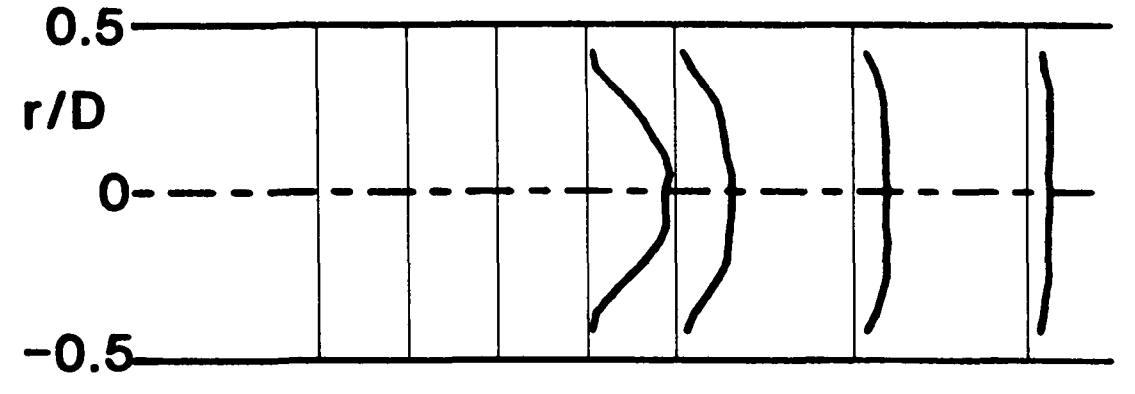

k) $u'_{rms}/\bar{u} \times 2$

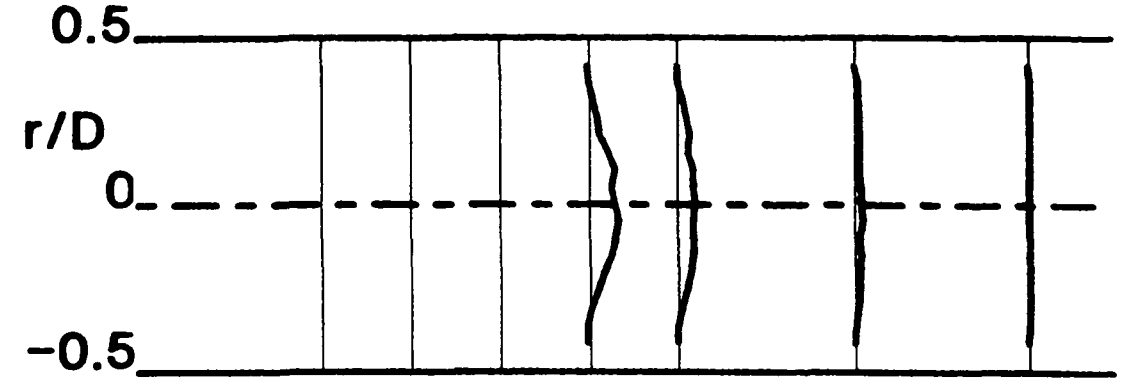

l) $\frac{1}{2}(u'^2_{rms} + v'^2_{rms} + w'^2_{rms})/u_o^2 \times 2$

Figure 9. (Continued)

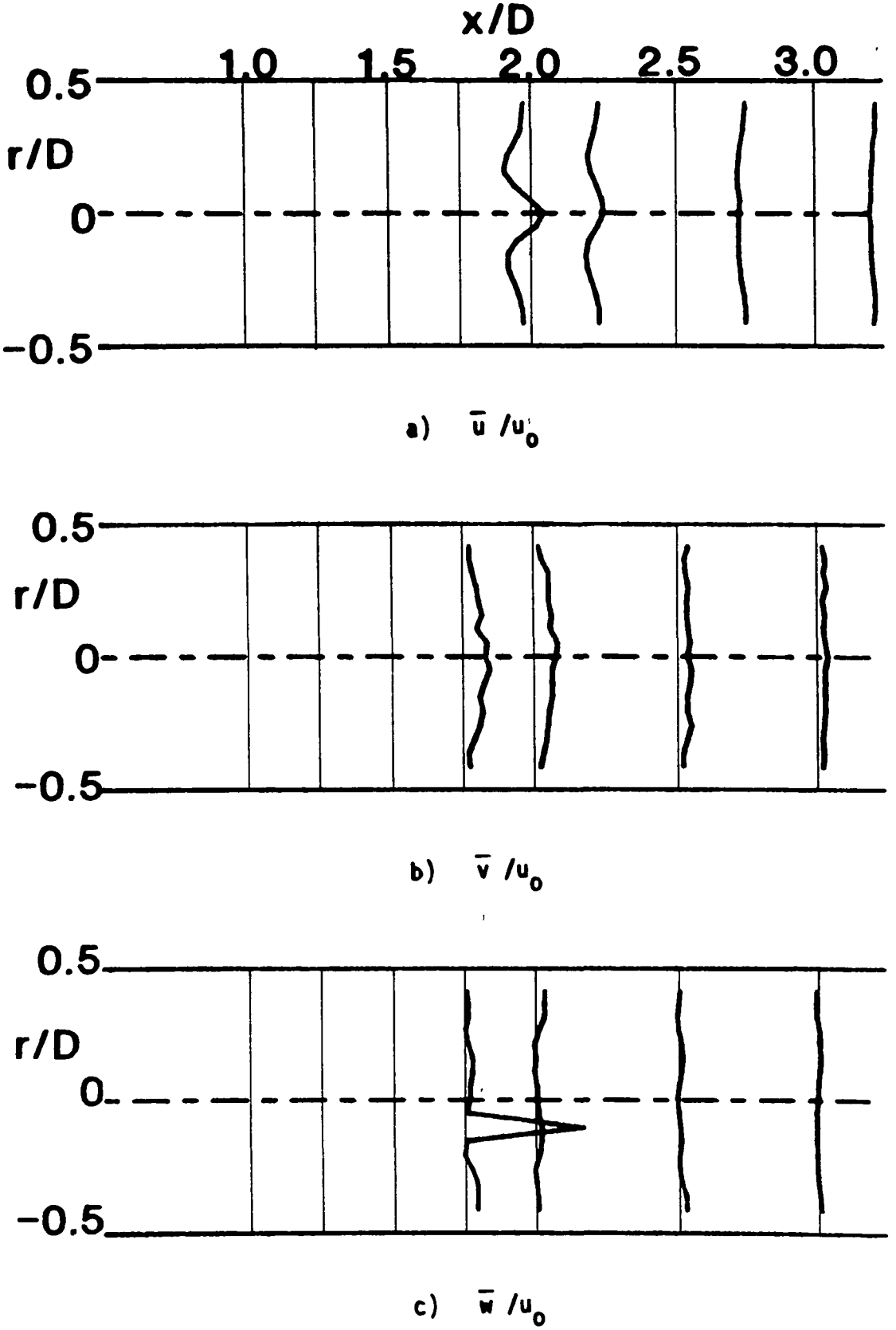

Figure 10. Time-Mean and Turbulent Flowfield, R = 4, ϕ = 0 Degrees (Swirler Removed), Traverse Angle θ = 330 Degrees.

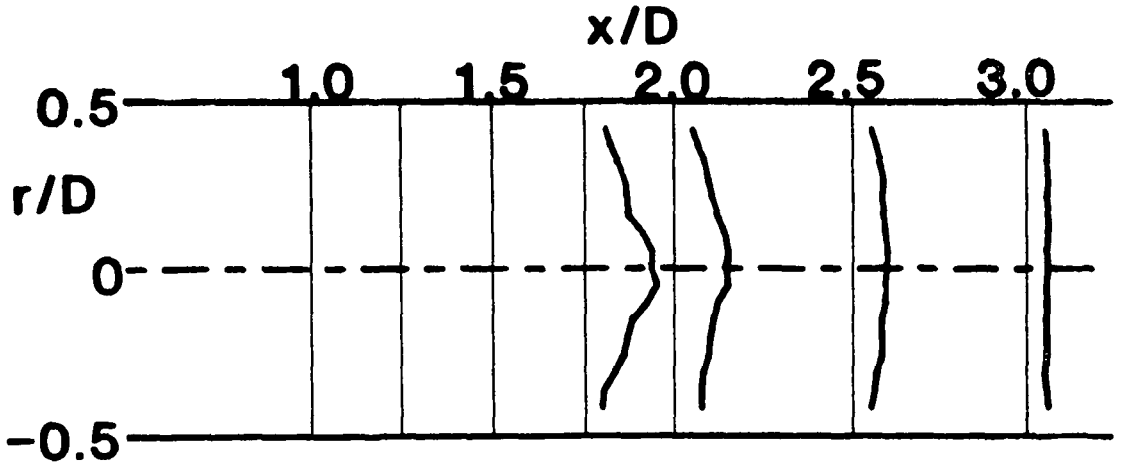

d) u'_{rms}/u_o x 2

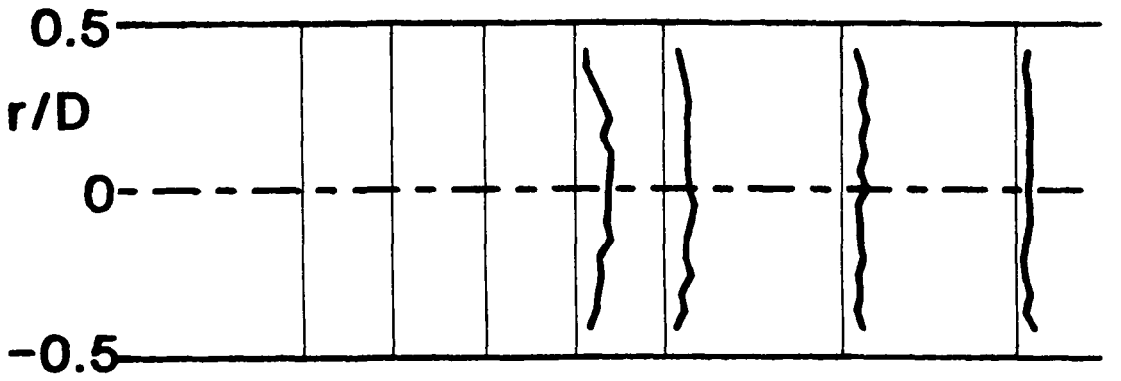

e) v'_{rms}/u_o x 2

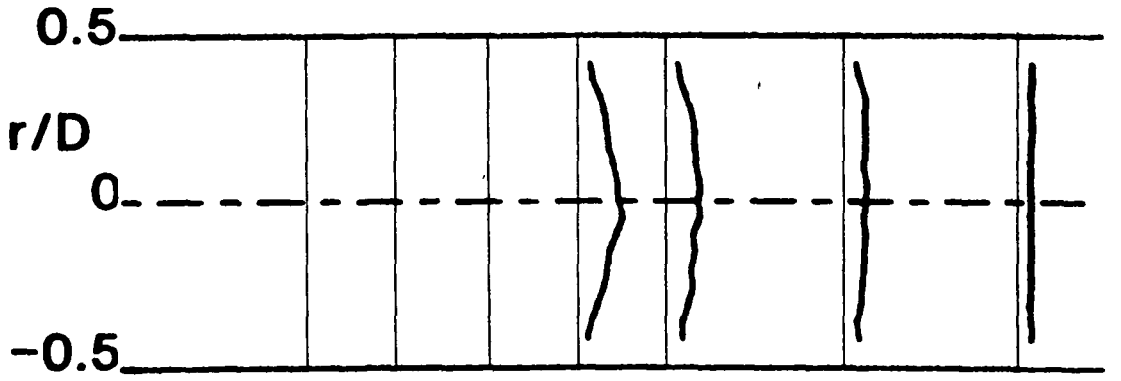

f) w'_{rms}/u_o x 2

Figure 10. (Continued)

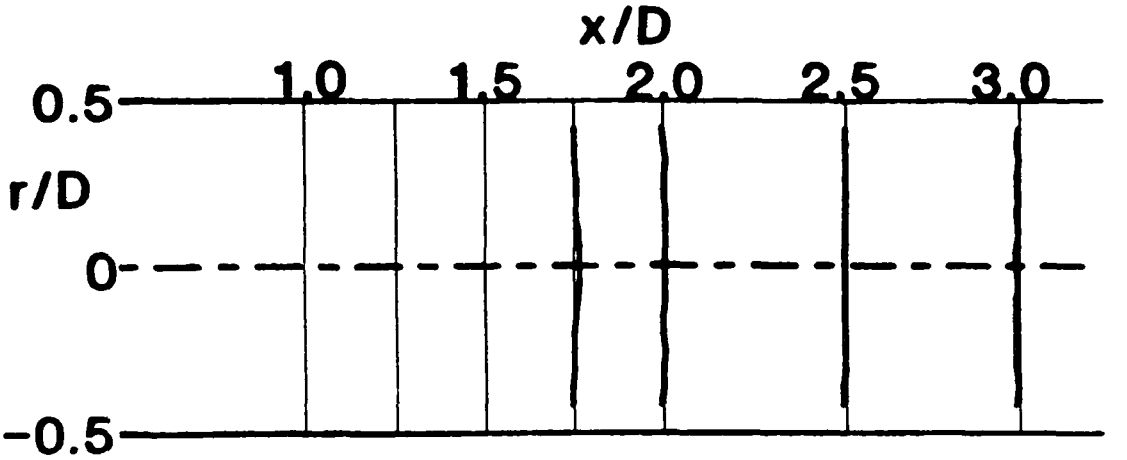

g) $\overline{u'v'}/u_o^2 \times 2$

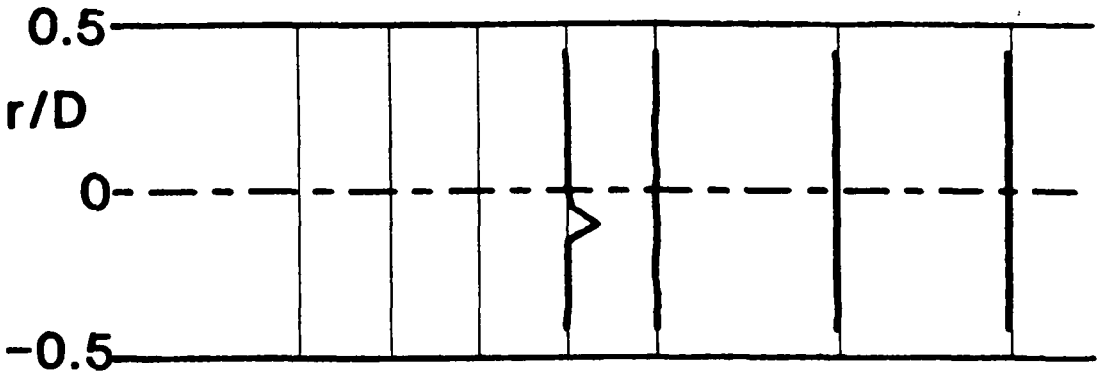

h) $\overline{u'w'}/u_o^2 \times 2$

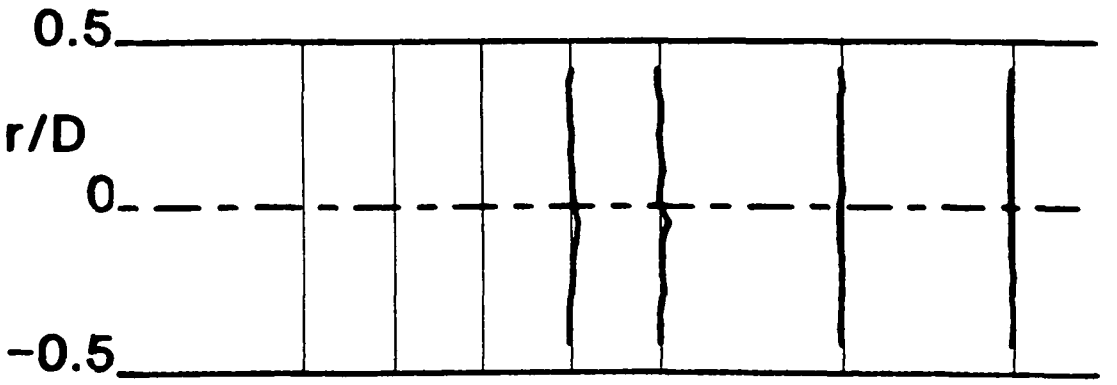

i) $\overline{v'w'}/u_o^2 \times 2$

Figure 10. (Continued)

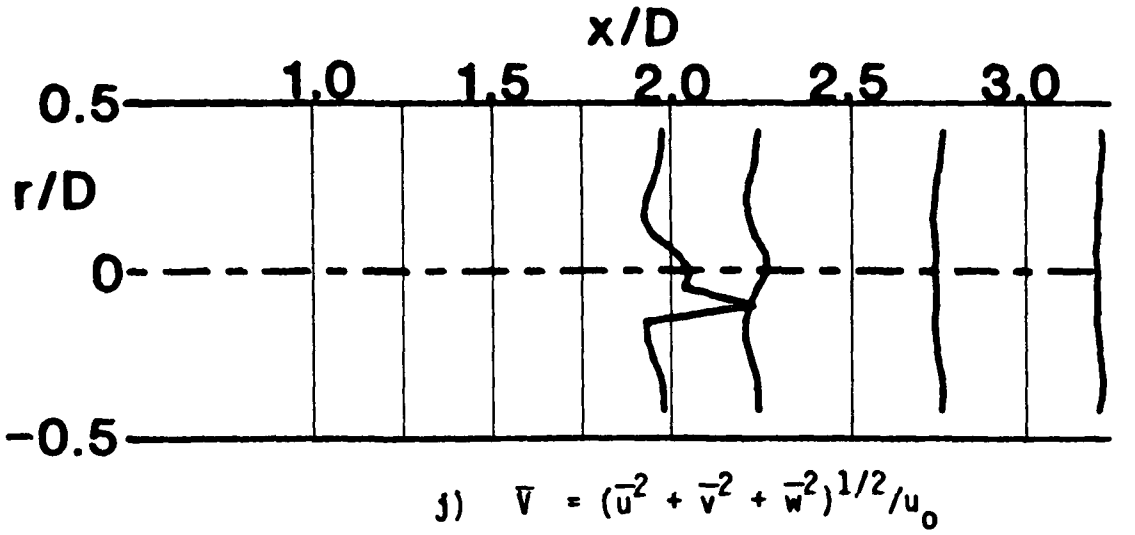

j) $\bar{V} = (\bar{u}^2 + \bar{v}^2 + \bar{w}^2)^{1/2}/u_o$

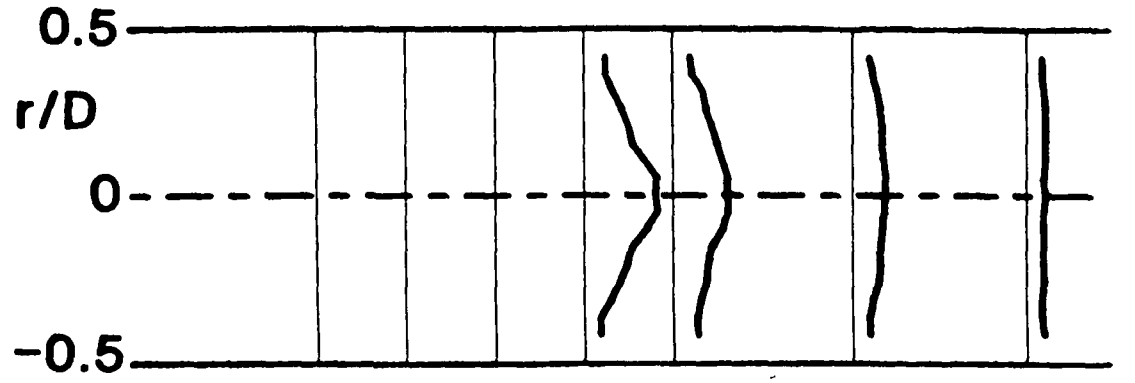

k) $u'_{rms}/\bar{u} \times 2$

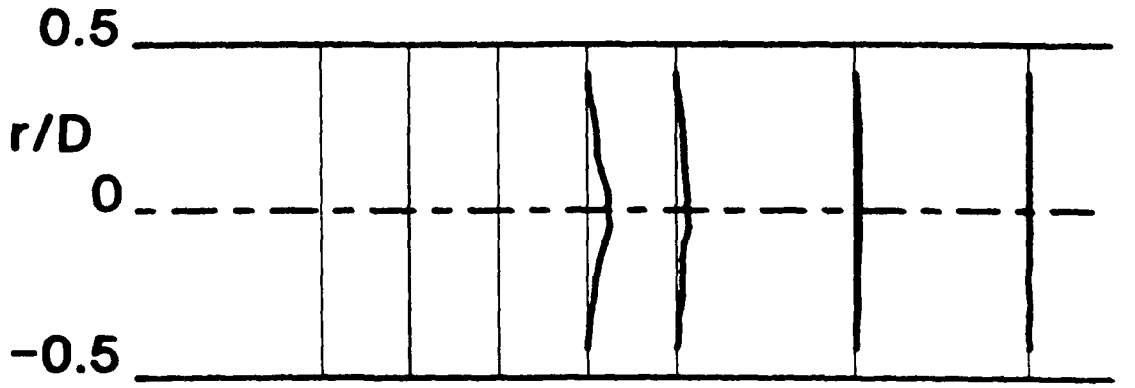

l) $\frac{1}{2}(u'_{rms}{}^2 + v'_{rms}{}^2 + w'_{rms}{}^2)/u_o^2 \times 2$

Figure 10. (Continued)

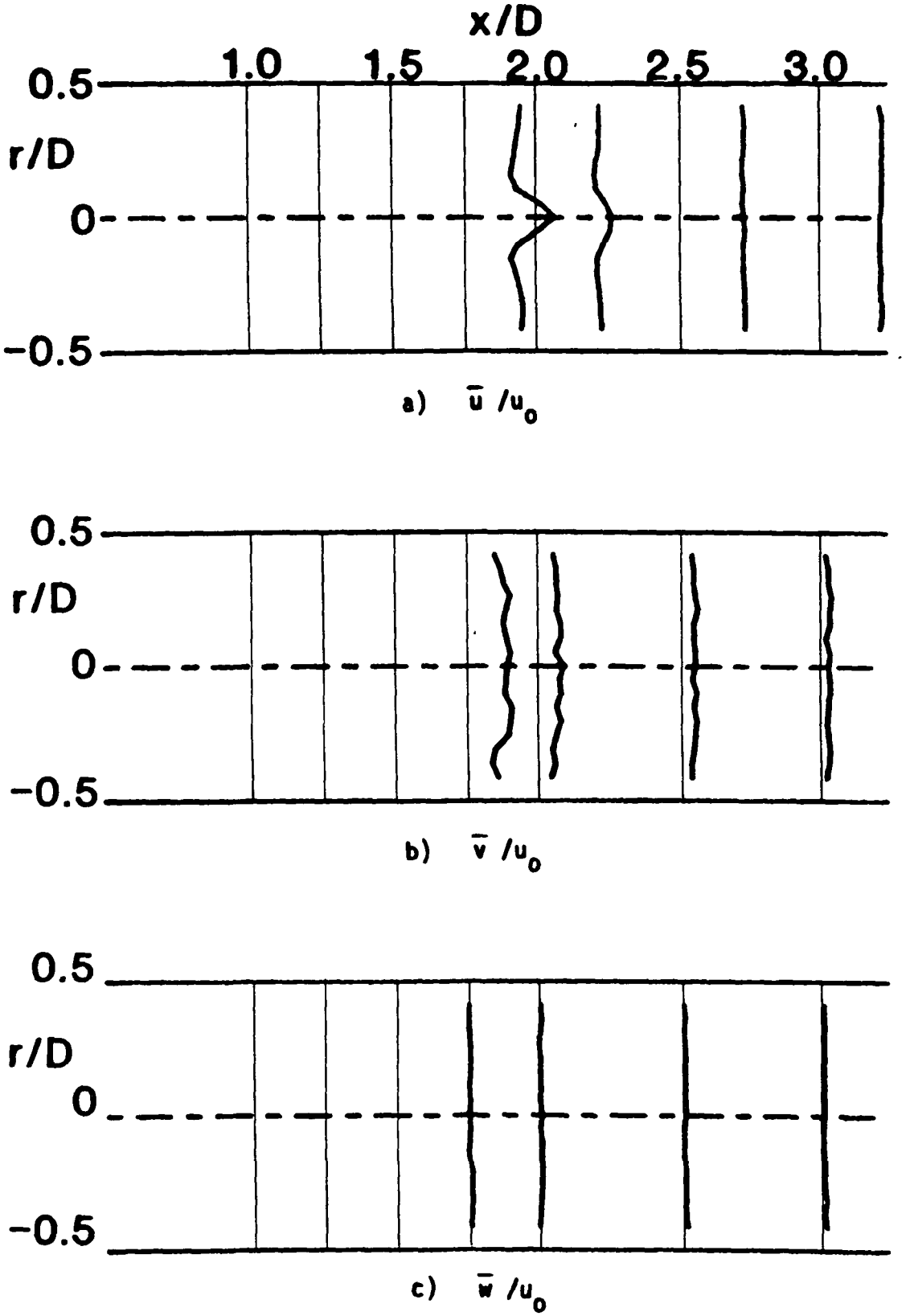

Figure 11. Time-Mean and Turbulent Flowfield, R = 4, ϕ = 0 Degrees (Swirler Removed), Traverse Angle θ = 0 Degrees.

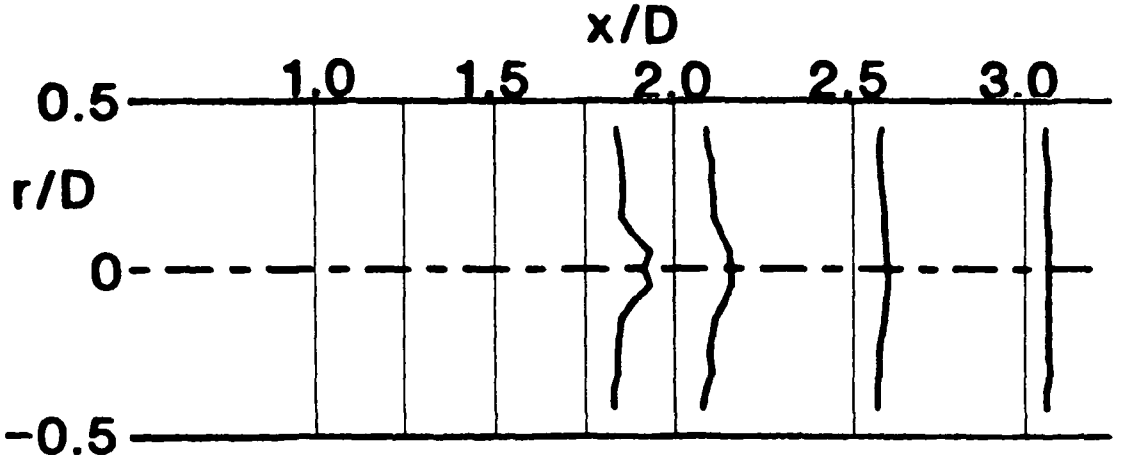

d) u'_{rms}/u_o x 2

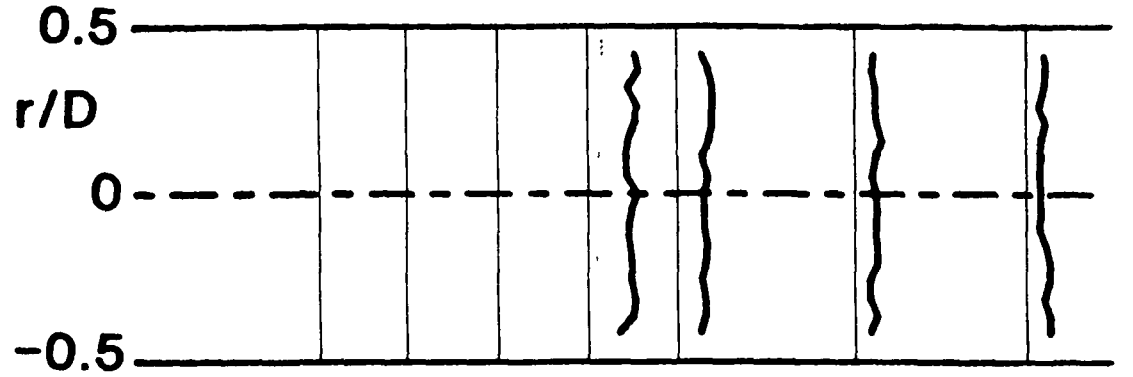

e) v'_{rms}/u_o x 2

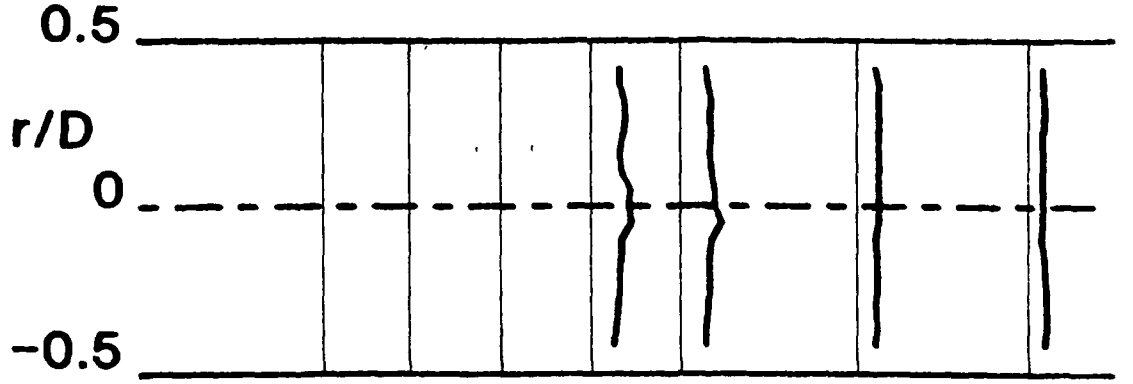

f) w'_{rms}/u_o x 2

Figure 11. (Continued)

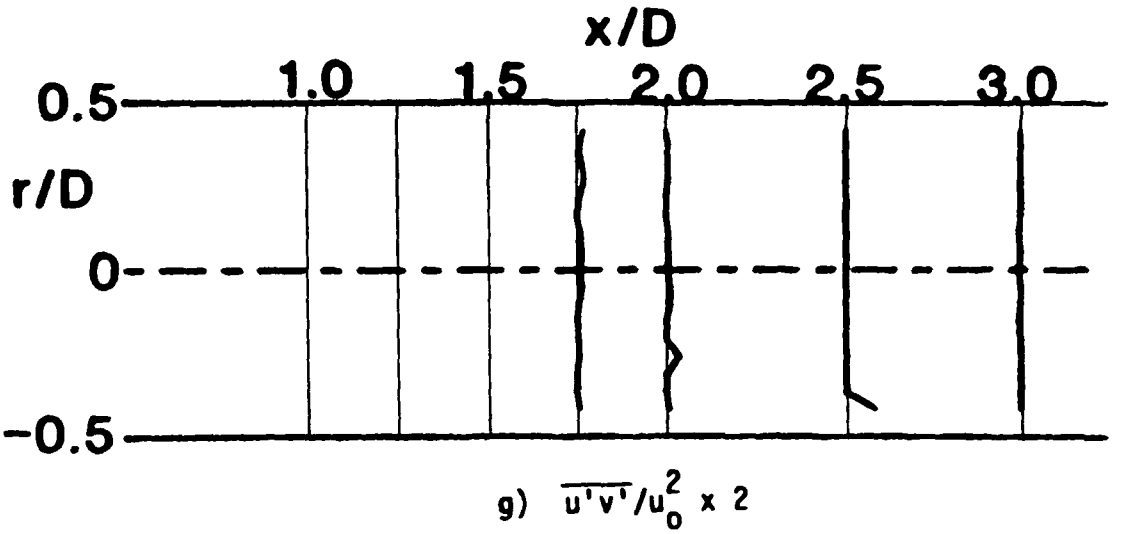

g) $\overline{u'v'}/u_o^2 \times 2$

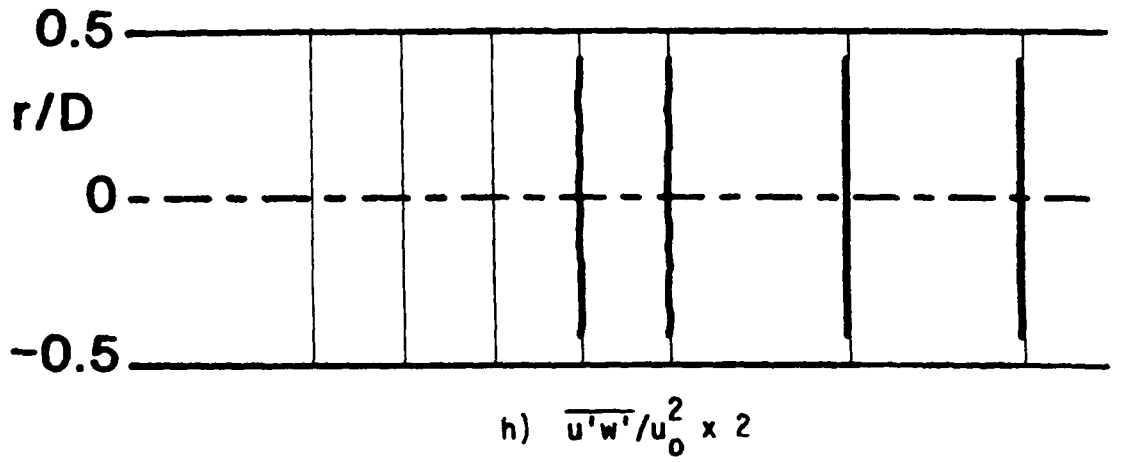

h) $\overline{u'w'}/u_o^2 \times 2$

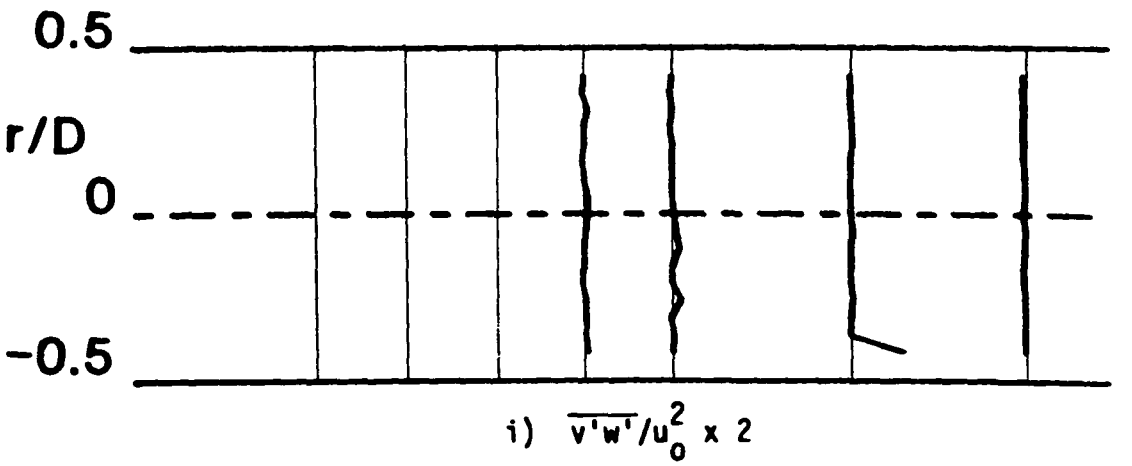

i) $\overline{v'w'}/u_o^2 \times 2$

Figure 11. (Continued)

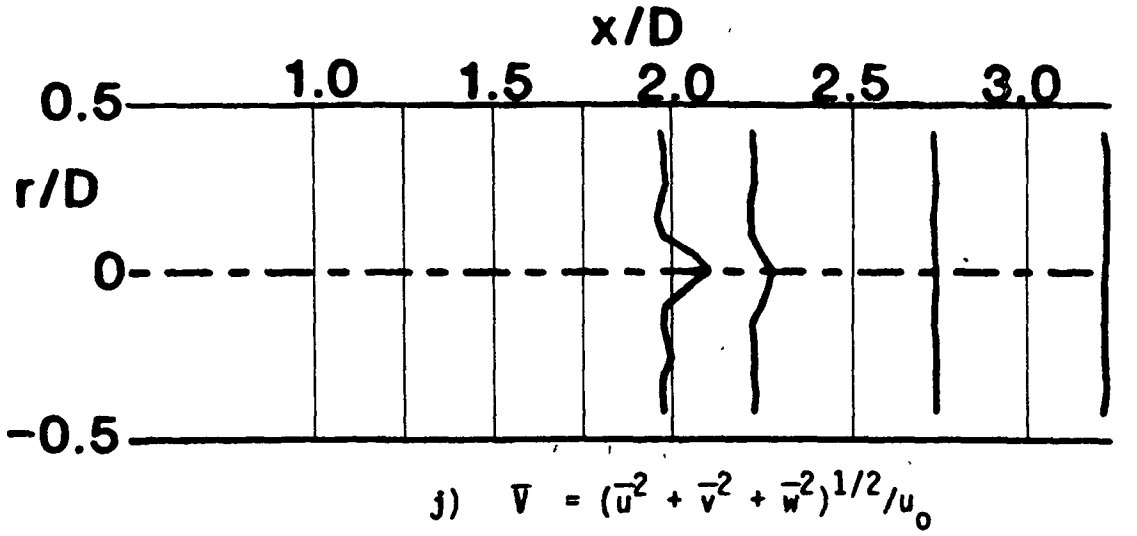

j) $\bar{V} = (\bar{u}^2 + \bar{v}^2 + \bar{w}^2)^{1/2}/u_o$

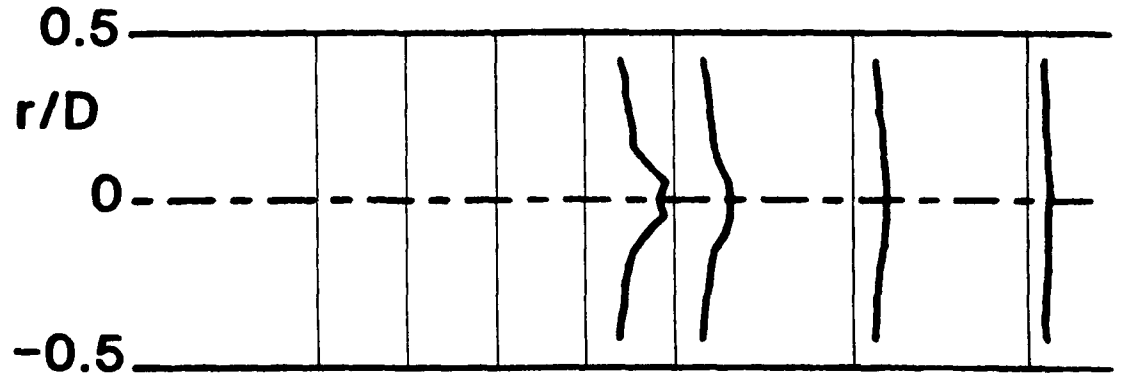

k) $u'_{rms}/\bar{u} \times 2$

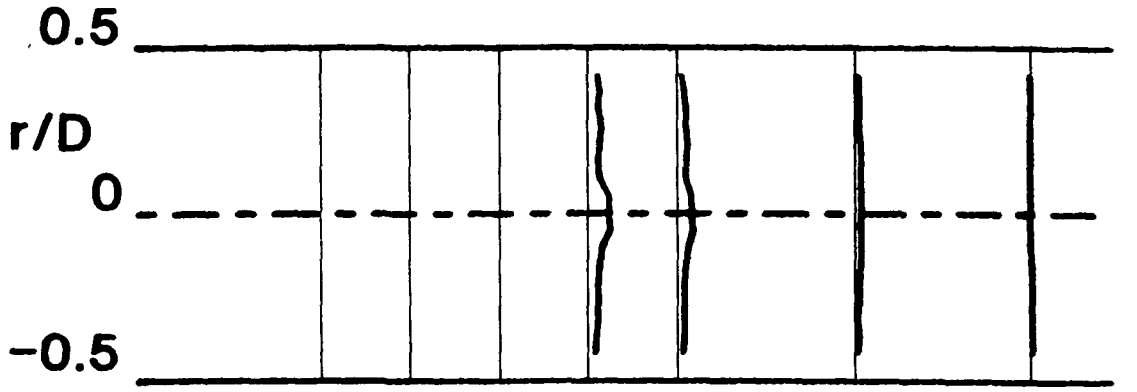

l) $\frac{1}{2}(u'^2_{rms} + v'^2_{rms} + w'^2_{rms})/u_o^2 \times 2$

Figure 11. (Continued)

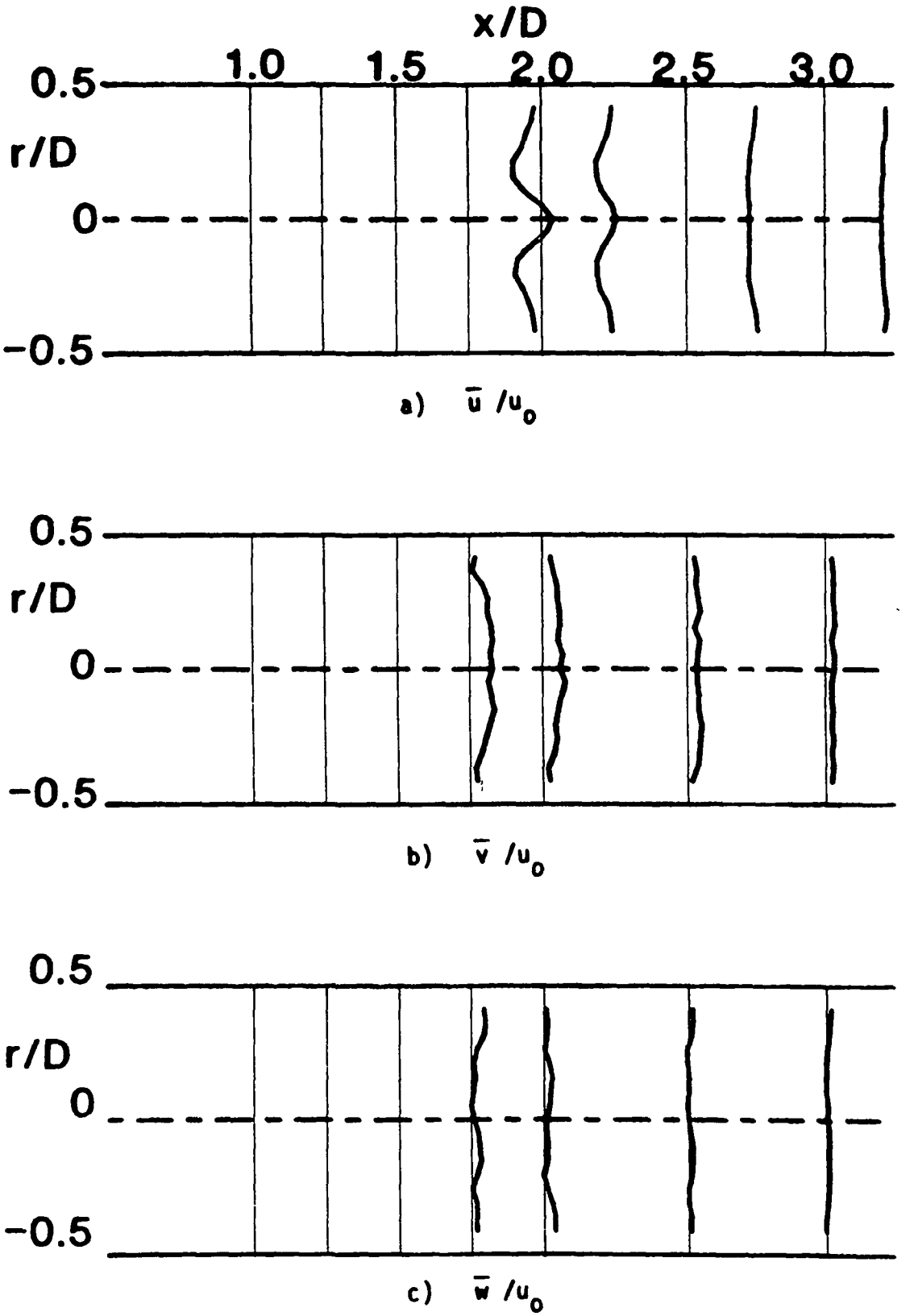

Figure 12. Time-Mean and Turbulent Flowfield, R = 4, ϕ = 0 Degrees (Swirler Removed), Traverse Angle θ = 30 Degrees.

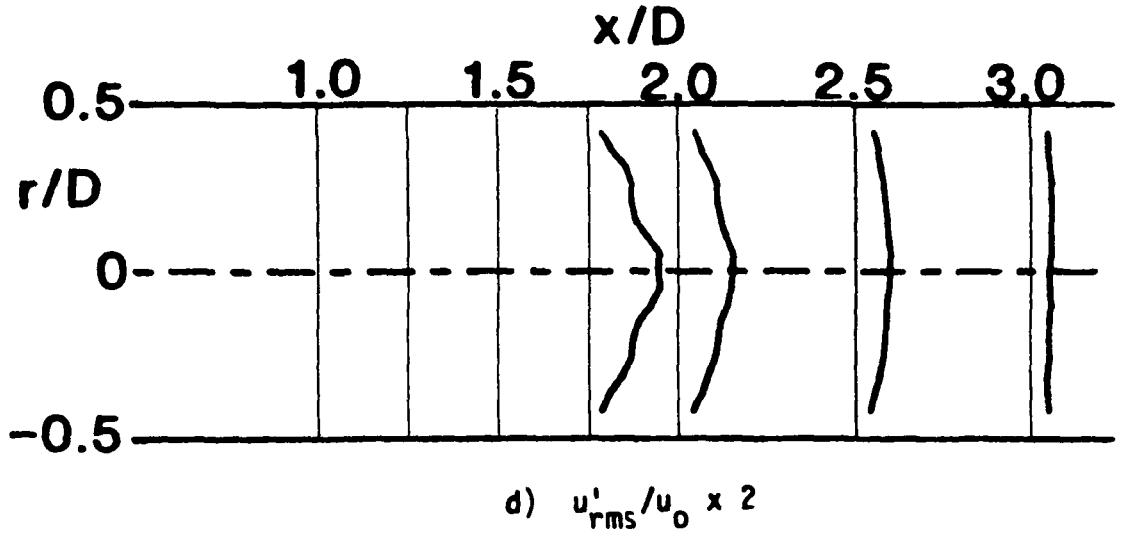

d) u'_{rms}/u_o x 2

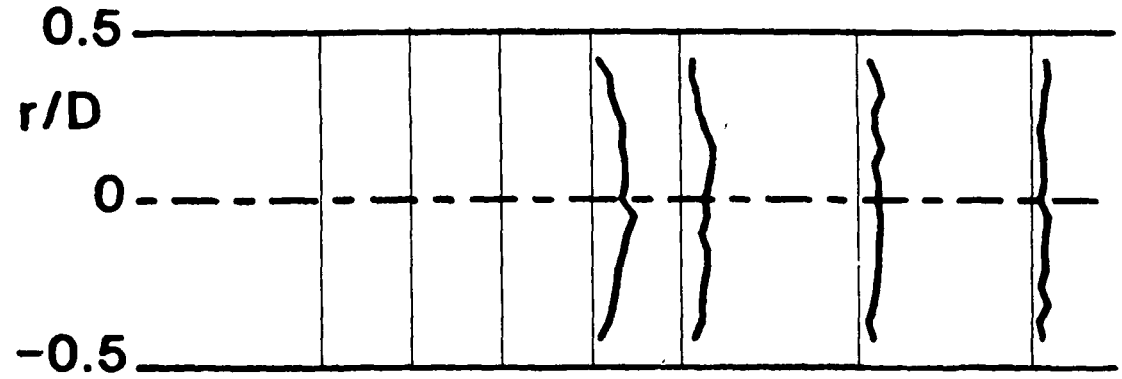

e) v'_{rms}/u_o x 2

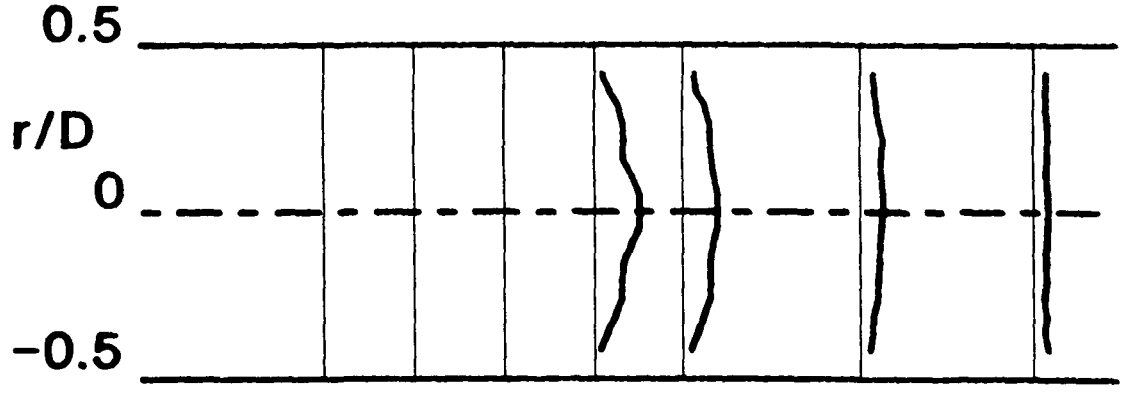

f) w'_{rms}/u_o x 2

Figure 12. (Continued)

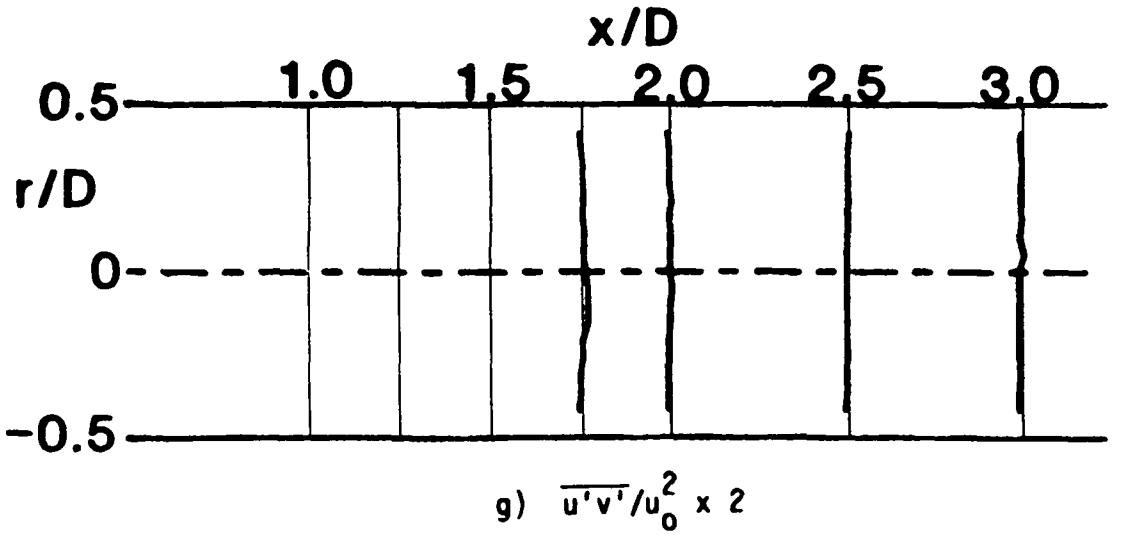

g) $\overline{u'v'}/u_o^2 \times 2$

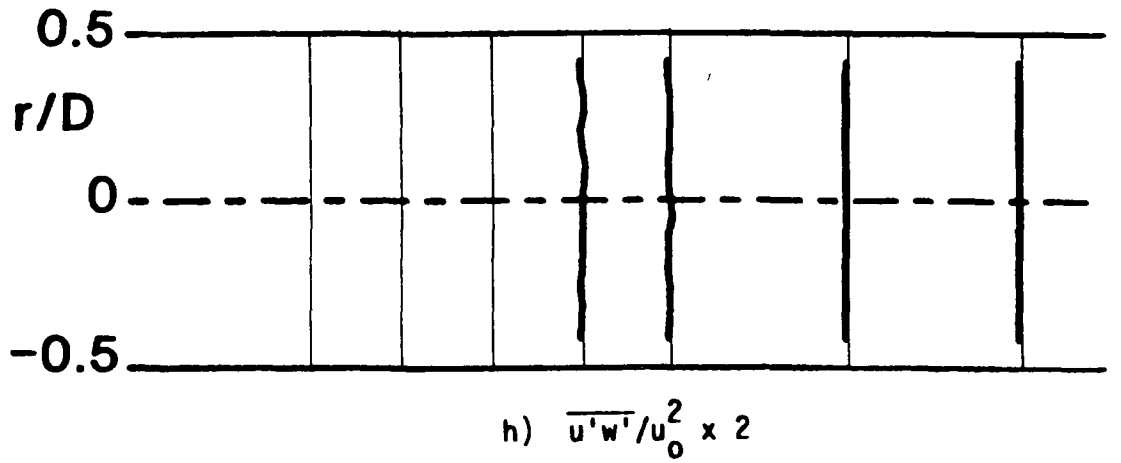

h) $\overline{u'w'}/u_o^2 \times 2$

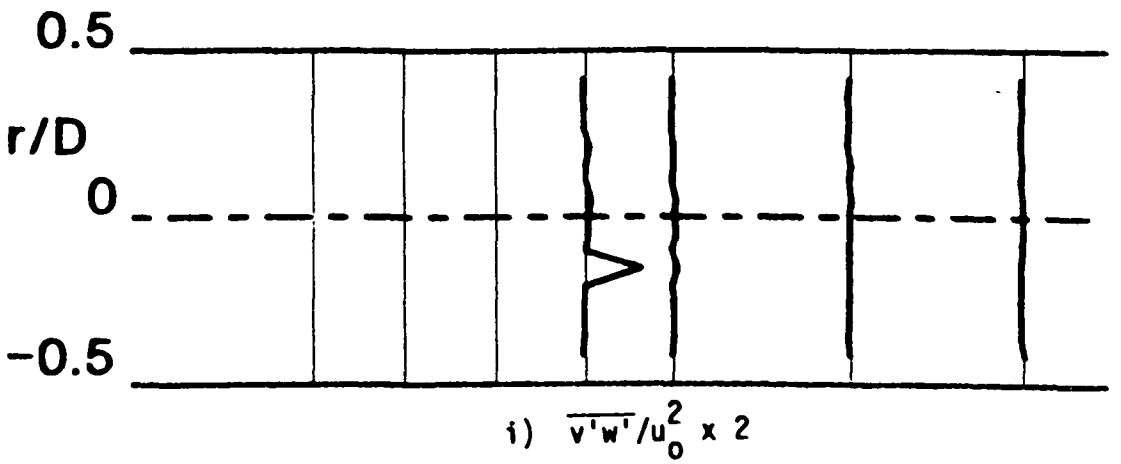

i) $\overline{v'w'}/u_o^2 \times 2$

Figure 12. (Continued)

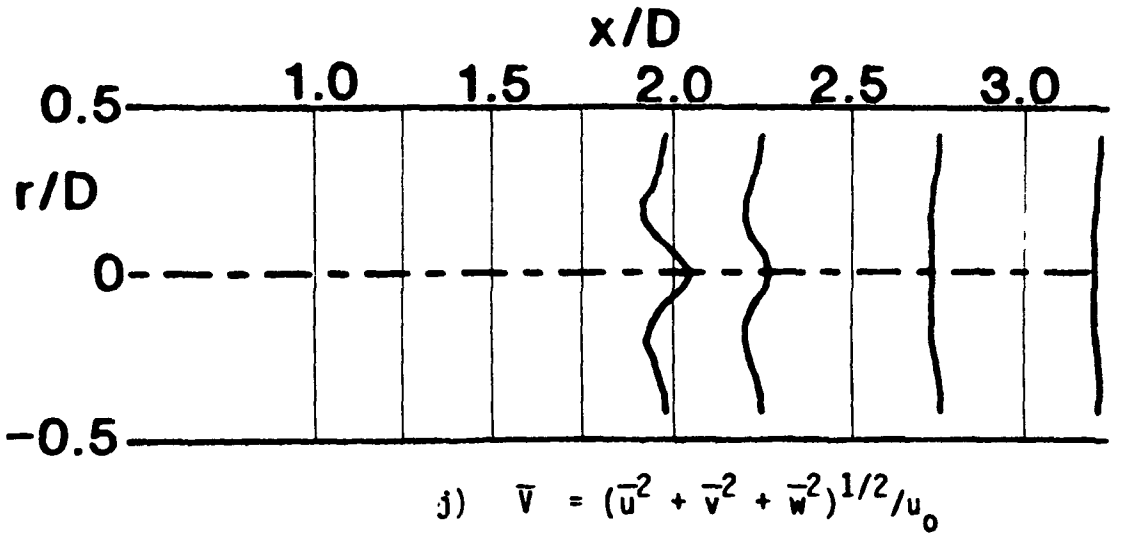

j) $\bar{V} = (\bar{u}^2 + \bar{v}^2 + \bar{w}^2)^{1/2}/u_o$

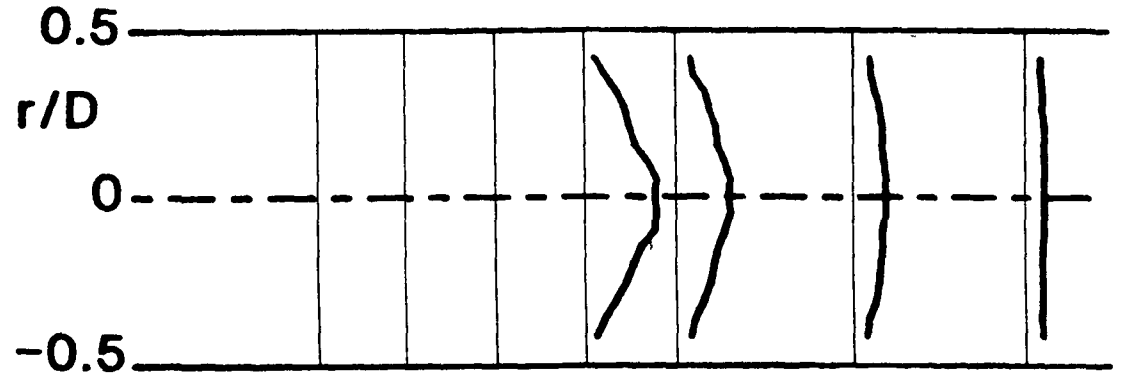

k) $u'_{rms}/\bar{u} \times 2$

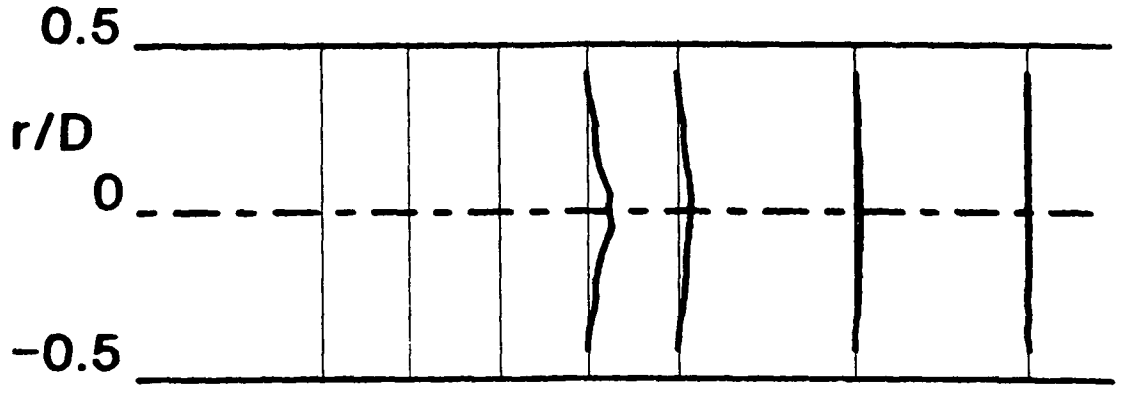

l) $\frac{1}{2}(u'^2_{rms} + v'^2_{rms} + w'^2_{rms})/u_o^2 \times 2$

Figure 12. (Continued)

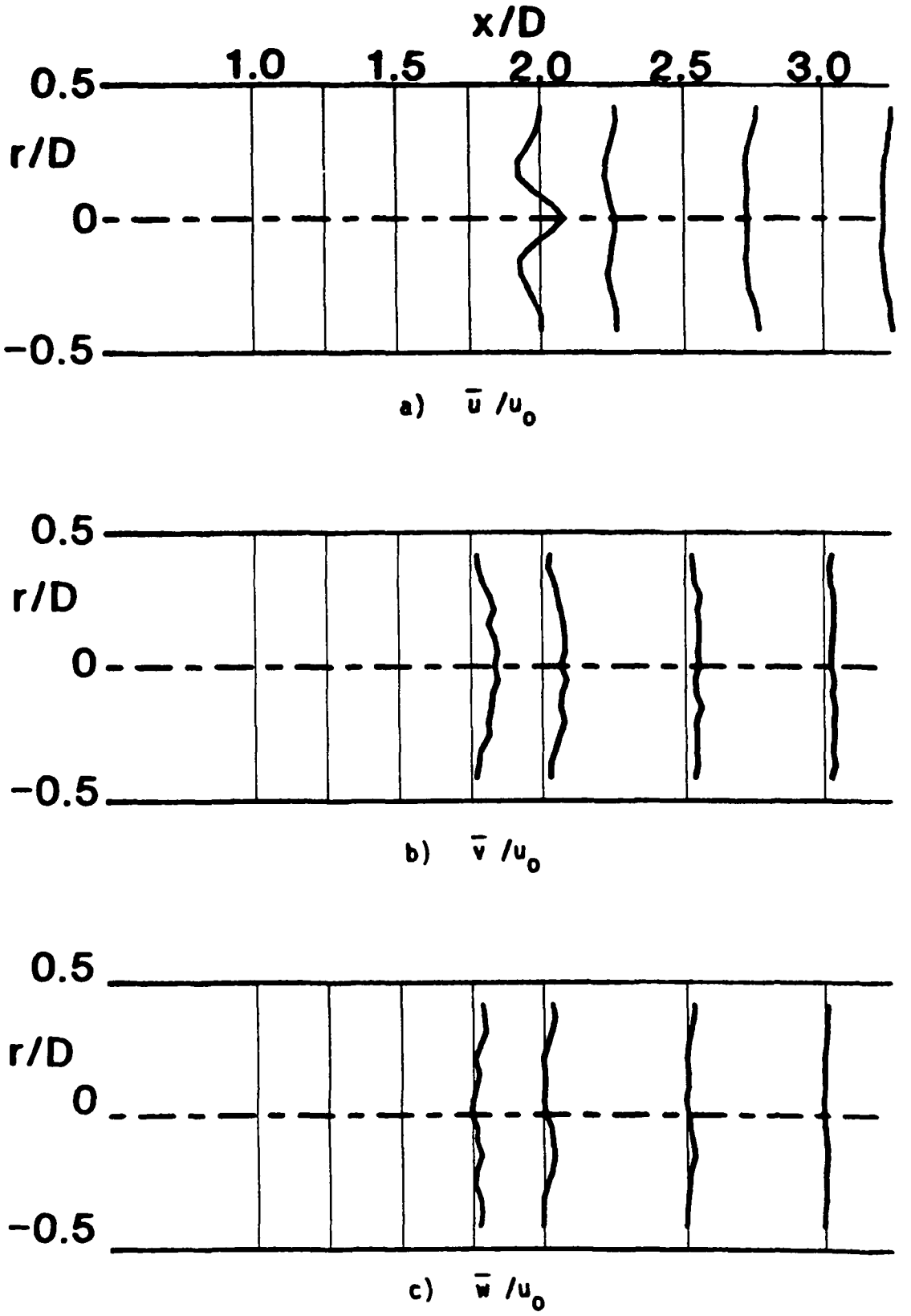

Figure 13. Time-Mean and Turbulent Flowfield, R = 4, ϕ = 0 Degrees (Swirler Removed), Traverse Angle θ = 60 Degrees.

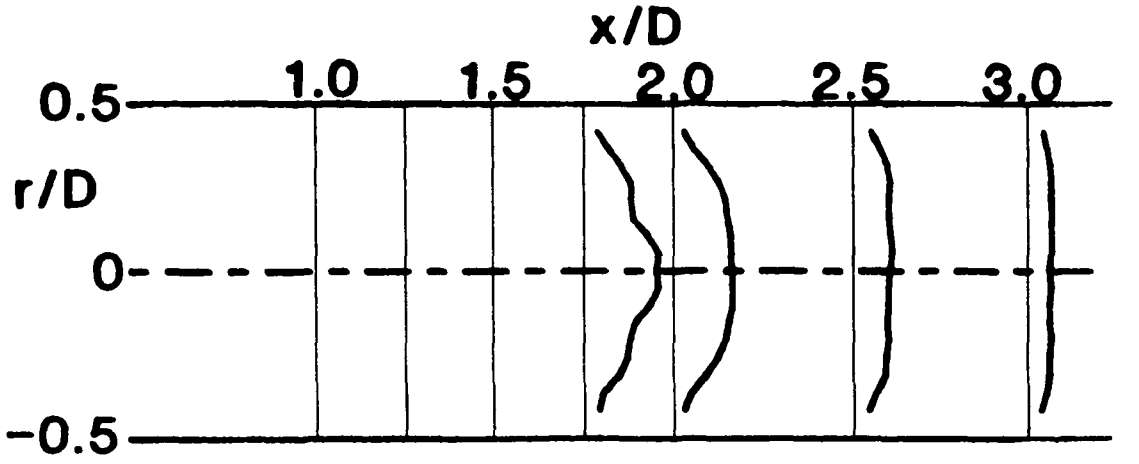

d) u'_{rms}/u_o x 2

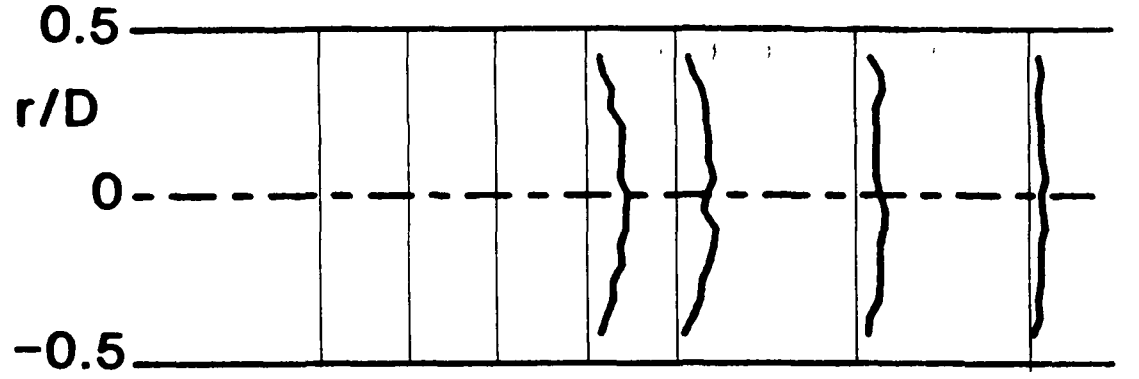

e) v'_{rms}/u_o x 2

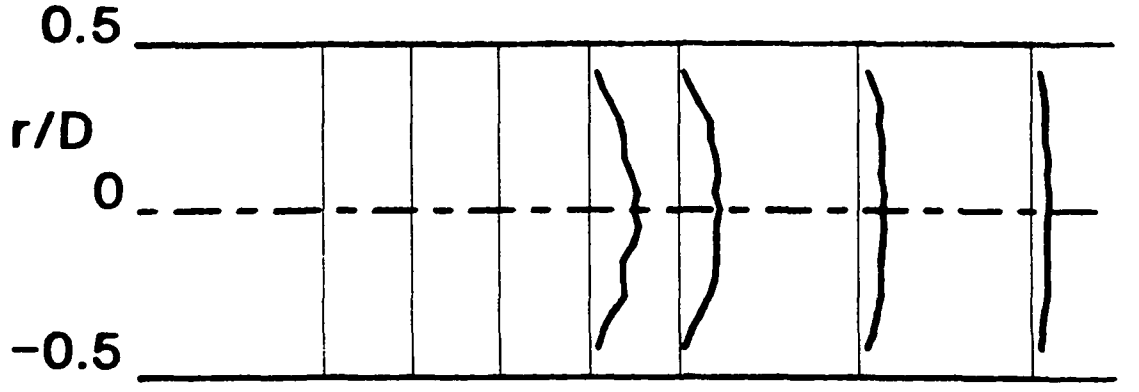

f) w'_{rms}/u_o x 2

Figure 13. (Continued)

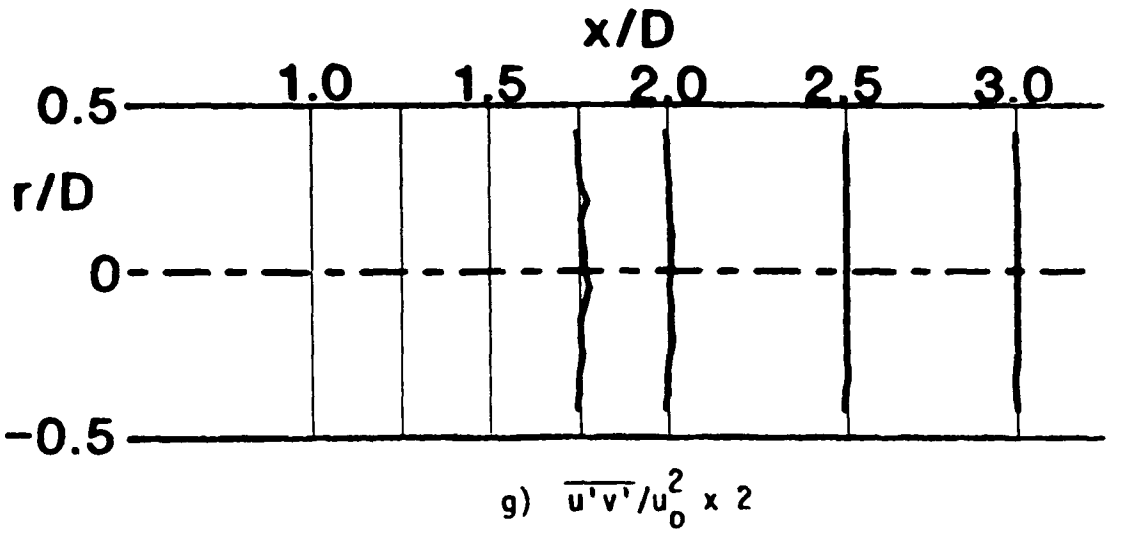

g) $\overline{u'v'}/u_o^2 \times 2$

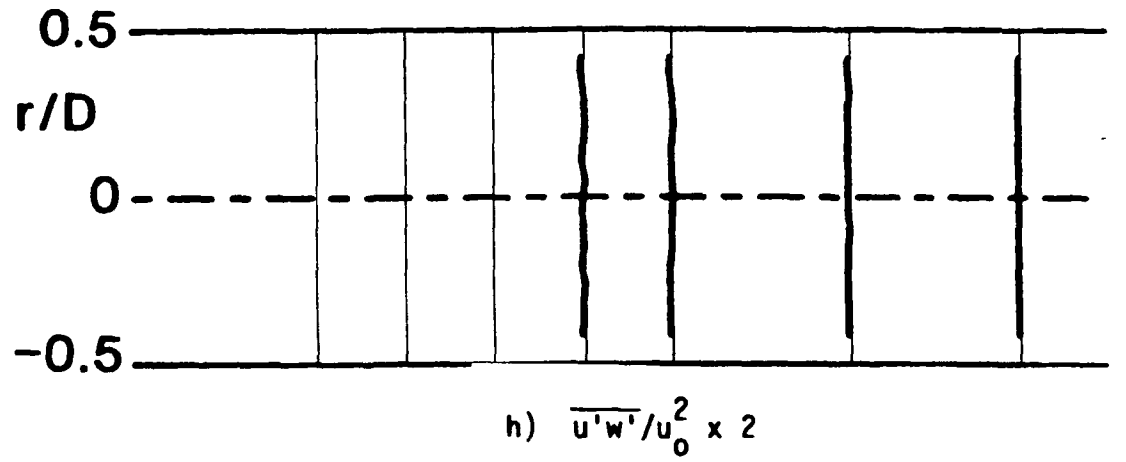

h) $\overline{u'w'}/u_o^2 \times 2$

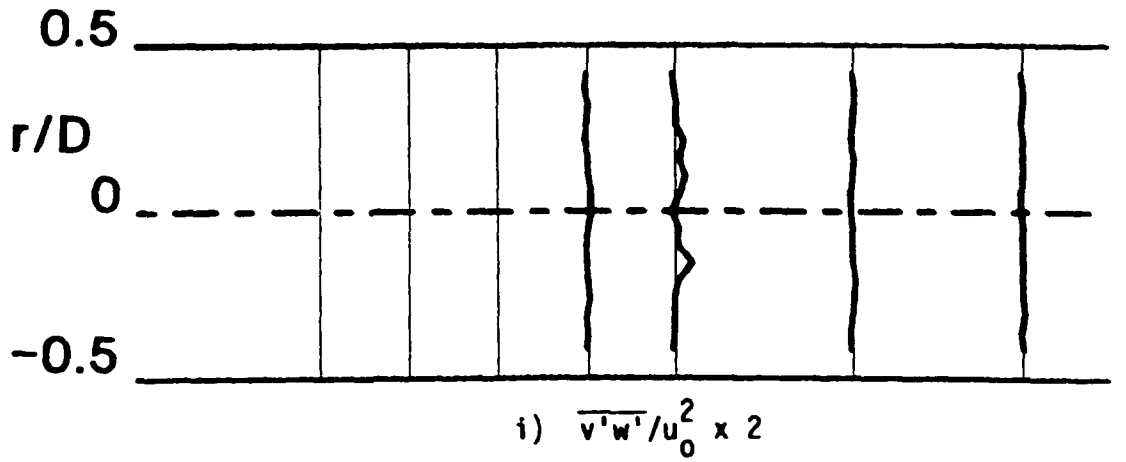

i) $\overline{v'w'}/u_o^2 \times 2$

Figure 13. (Continued)

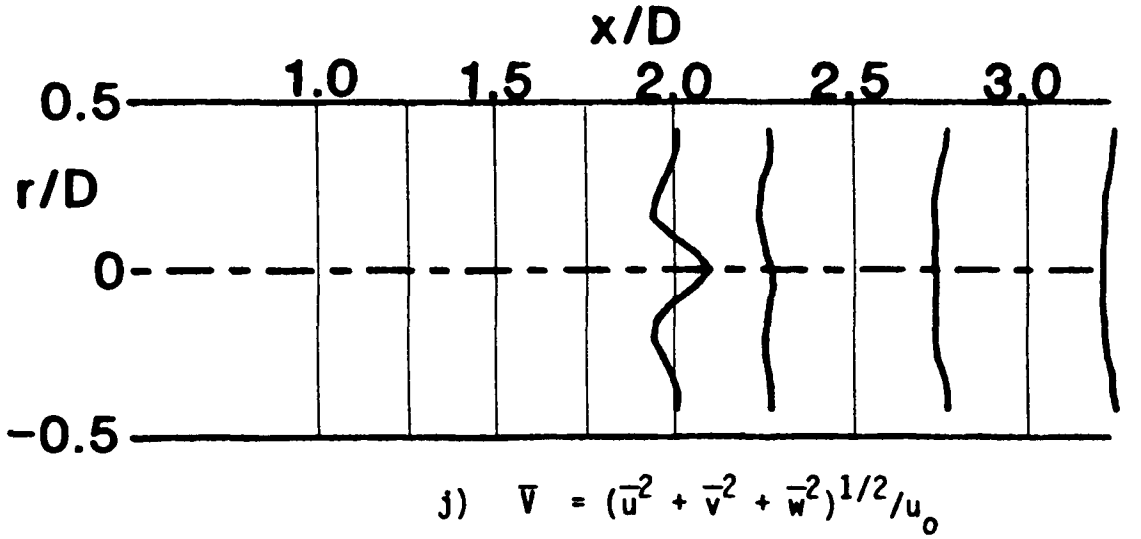

j) $\bar{V} = (\bar{u}^2 + \bar{v}^2 + \bar{w}^2)^{1/2}/u_o$

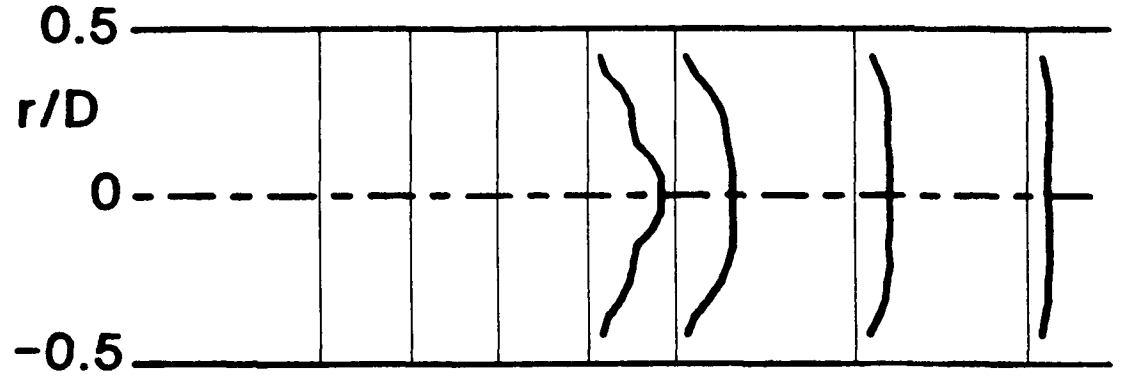

k) $u'_{rms}/\bar{u} \times 2$

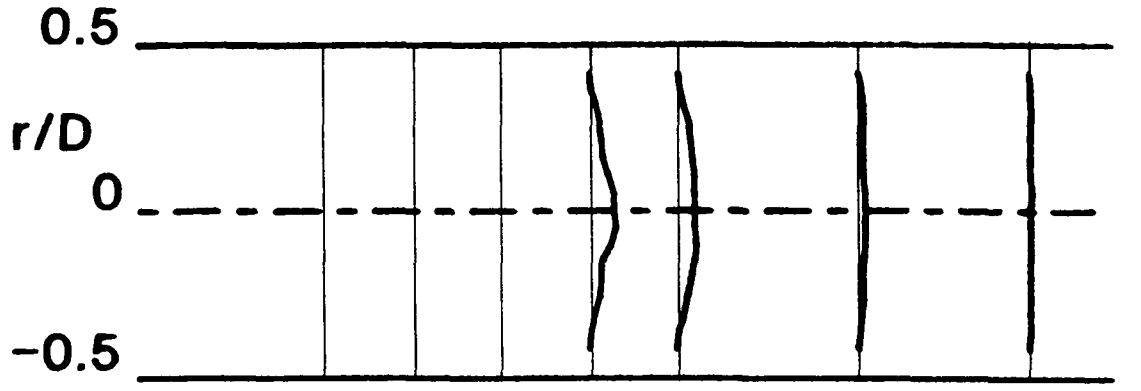

l) $\frac{1}{2}(u'^2_{rms} + v'^2_{rms} + w'^2_{rms})/u_o^2 \times 2$

Figure 13. (Continued)

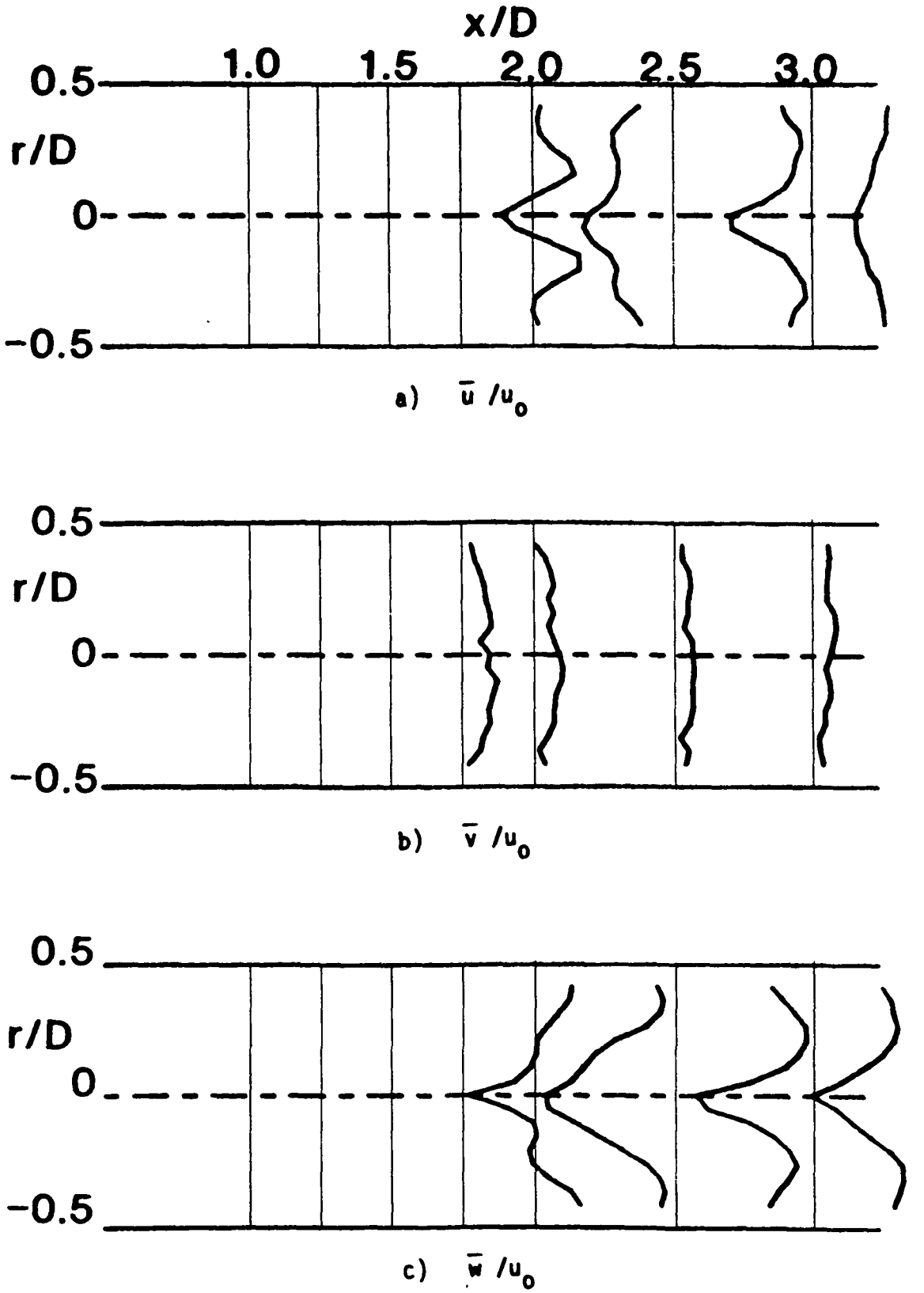

Figure 14. Time-Mean and Turbulent Flowfield, R = 4, ϕ = 45 Degrees, Traverse Angle θ = 270 Degrees.

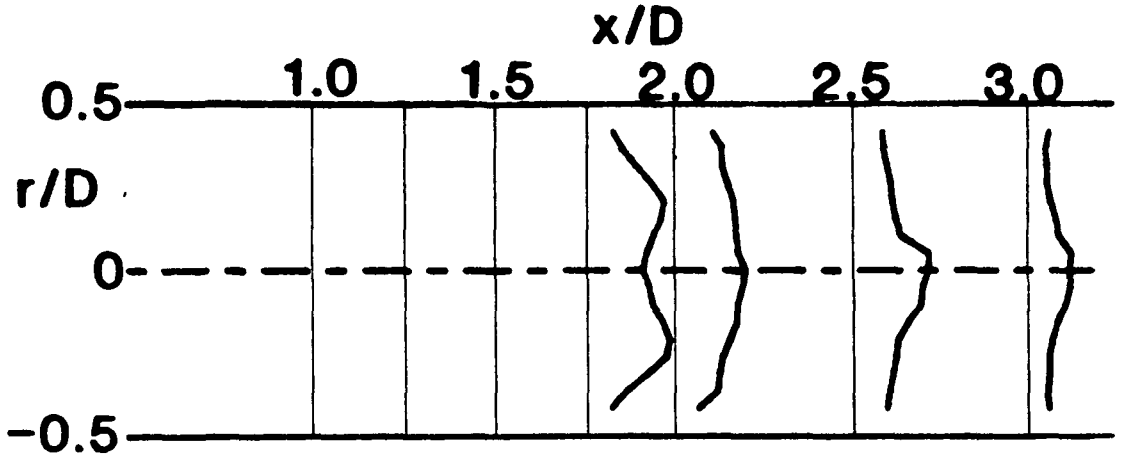

d) u'_{rms}/u_o x 2

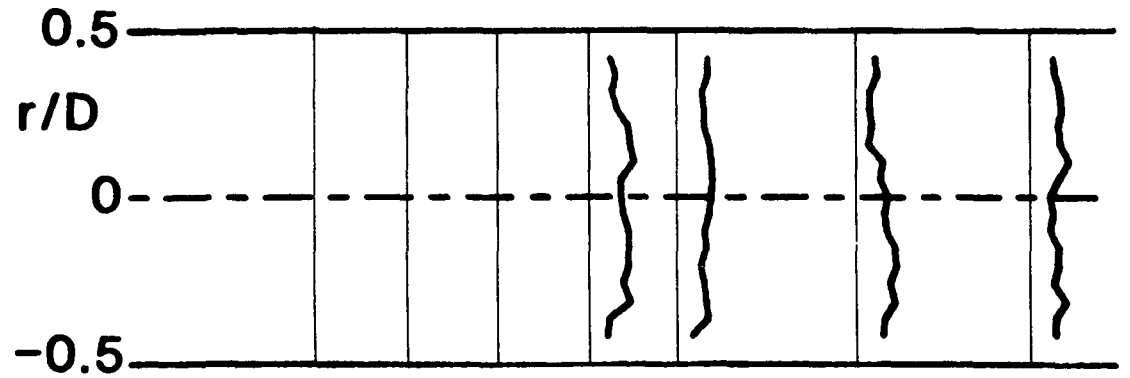

e) v'_{rms}/u_o x 2

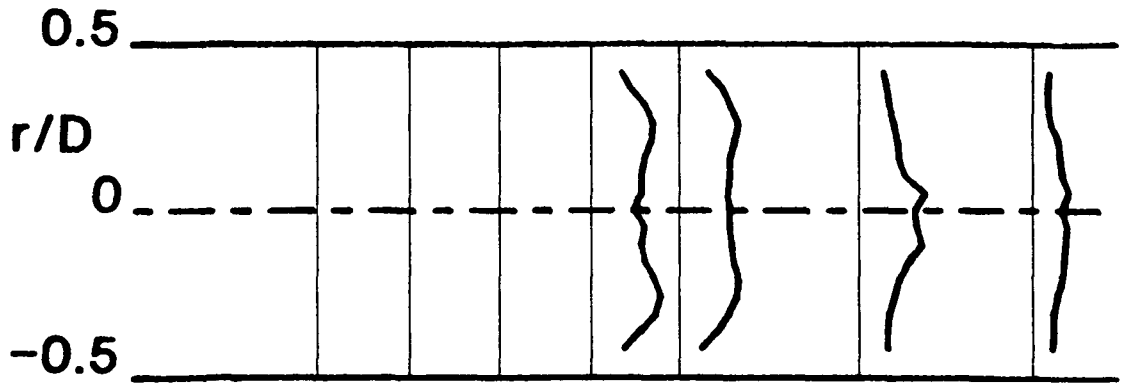

f) w'_{rms}/u_o x 2

Figure 14. (Continued)

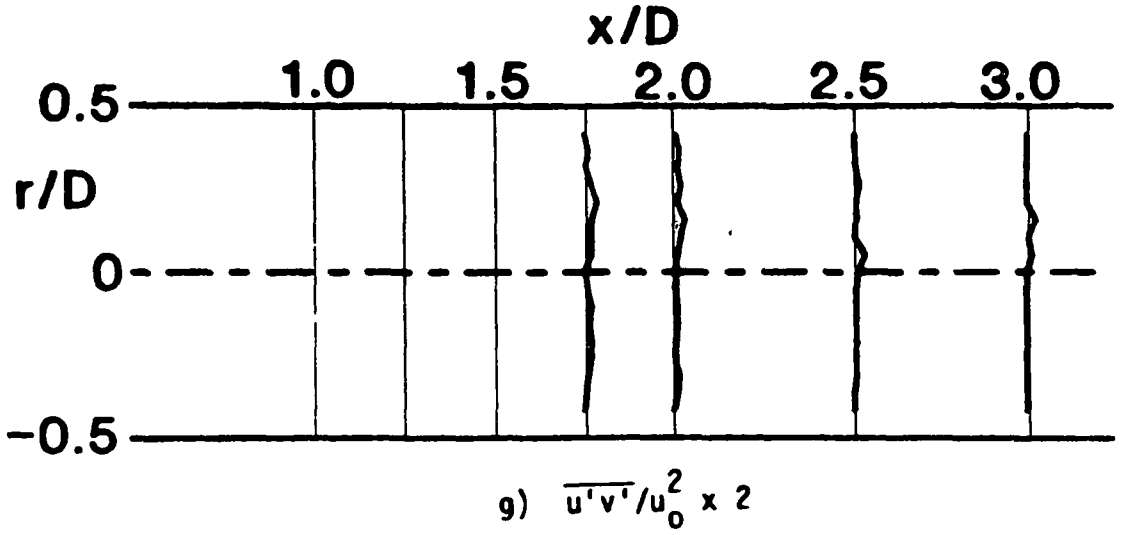

g) $\overline{u'v'}/u_o^2 \times 2$

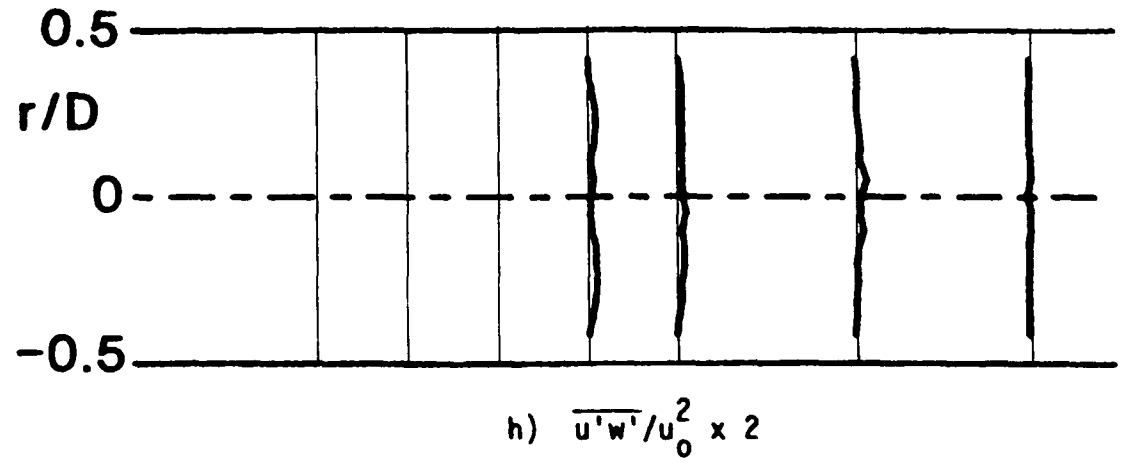

h) $\overline{u'w'}/u_o^2 \times 2$

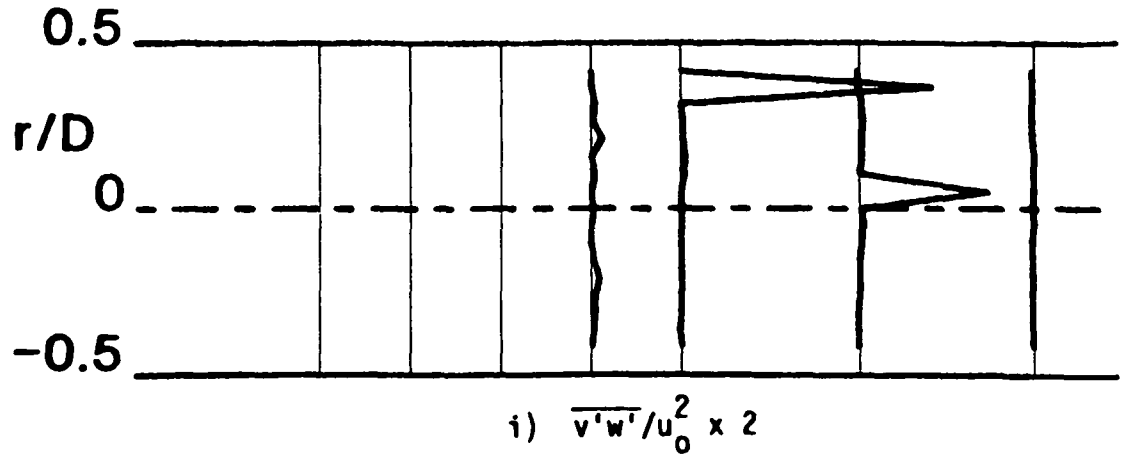

i) $\overline{v'w'}/u_o^2 \times 2$

Figure 14. (Continued)

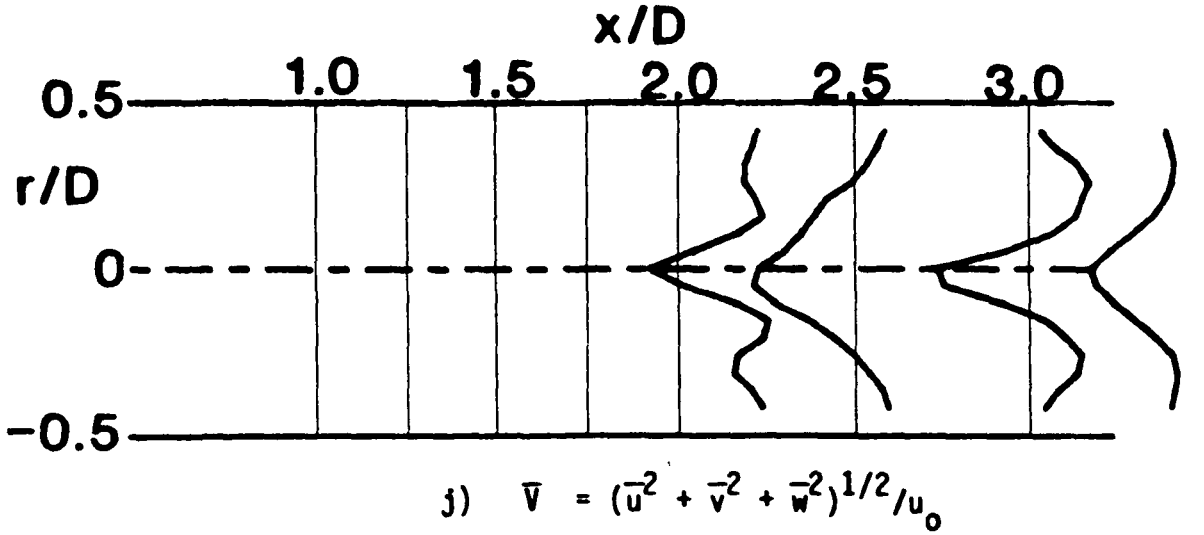

j) $\bar{V} = (\bar{u}^2 + \bar{v}^2 + \bar{w}^2)^{1/2}/u_o$

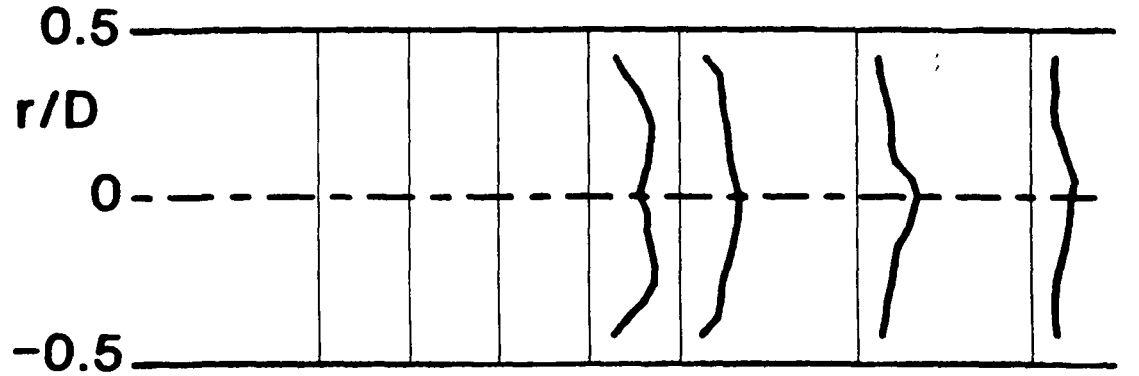

k) $u'_{rms}/\bar{u} \times 2$

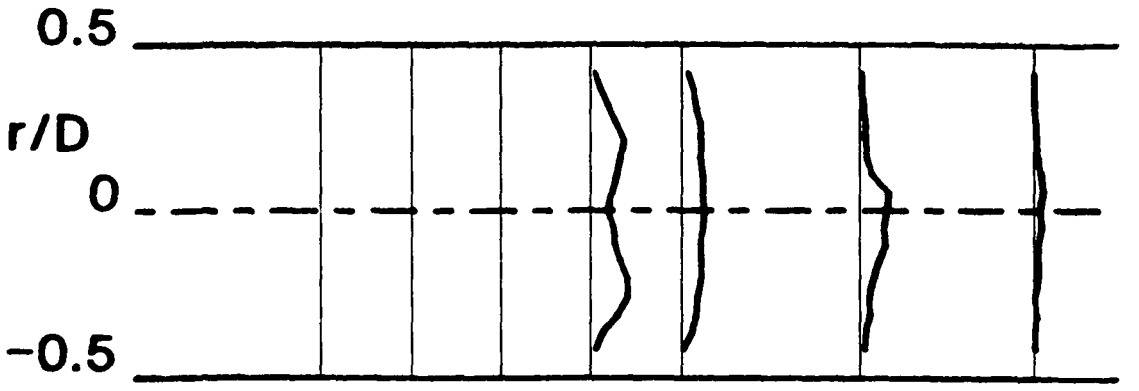

l) $\frac{1}{2}(u'^2_{rms} + v'^2_{rms} + w'^2_{rms})/u_o^2 \times 2$

Figure 14. (Continued)

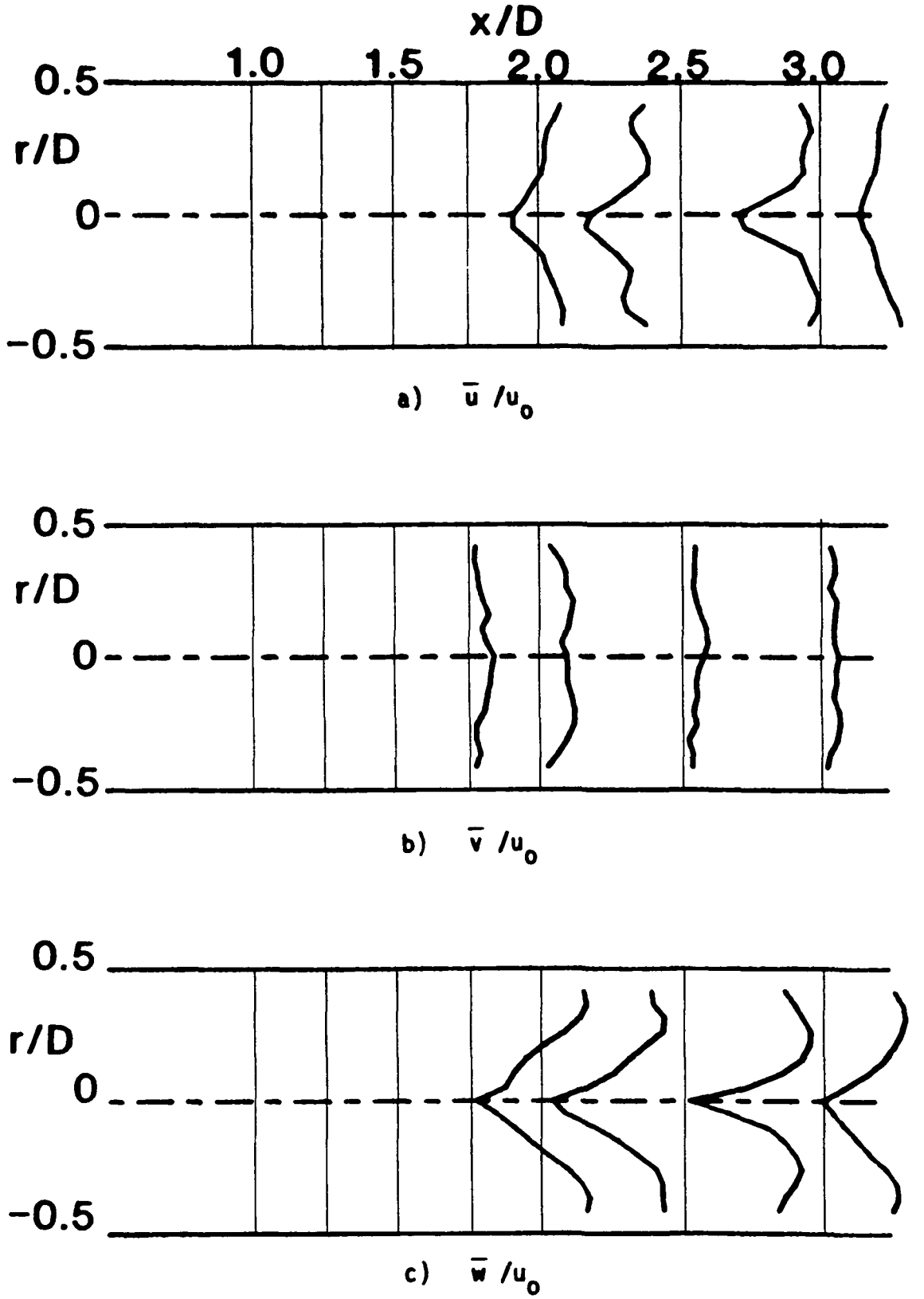

Figure 15. Time-Mean and Turbulent Flowfield, R = 4, ϕ = 45 Degrees, Traverse Angle θ = 300 Degrees.

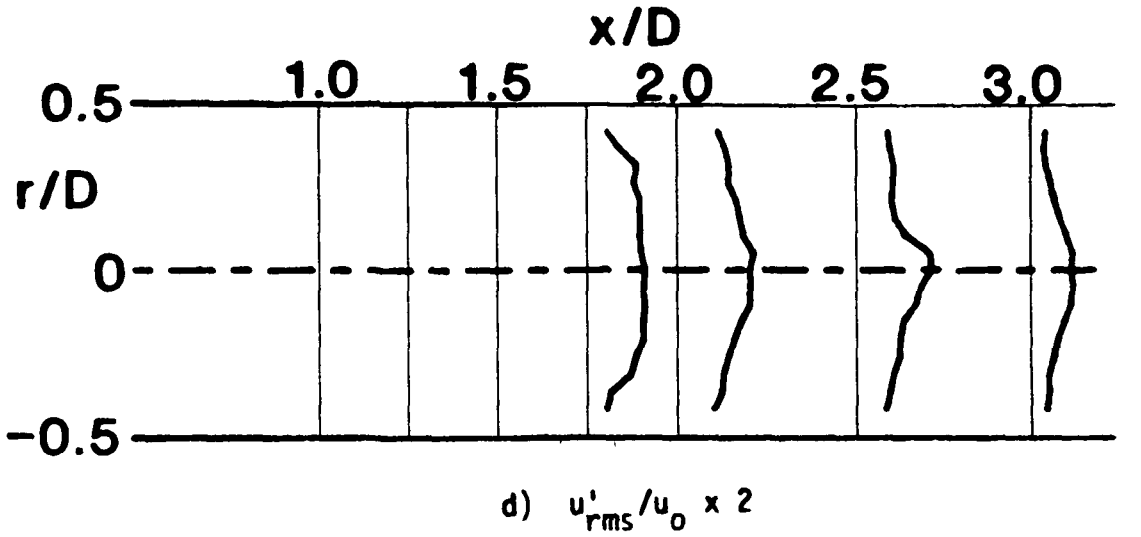

d) u'_{rms}/u_o x 2

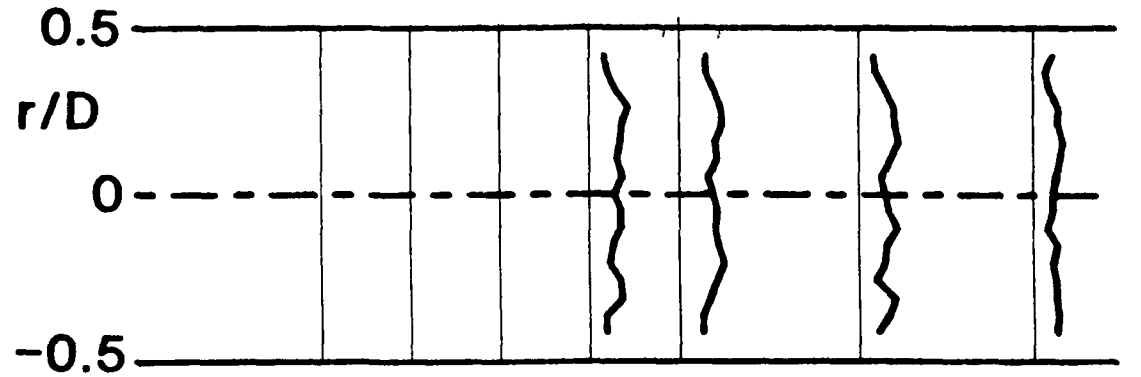

e) v'_{rms}/u_o x 2

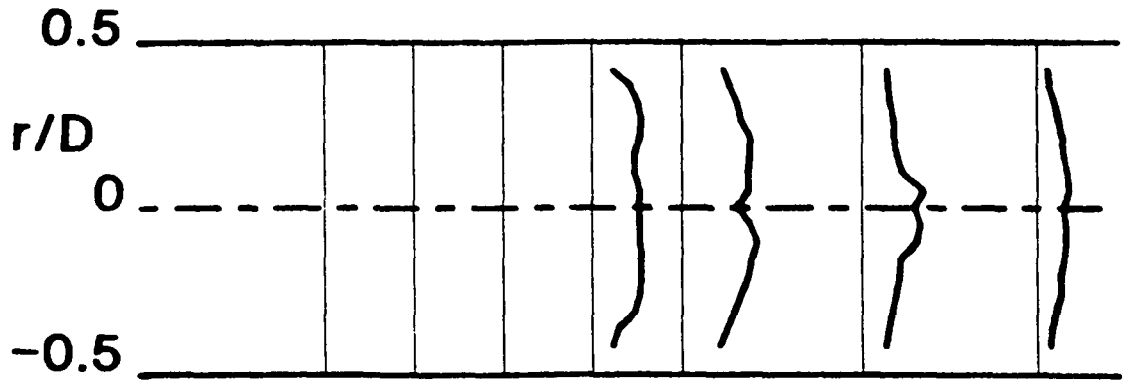

f) w'_{rms}/u_o x 2

Figure 15. (Continued)

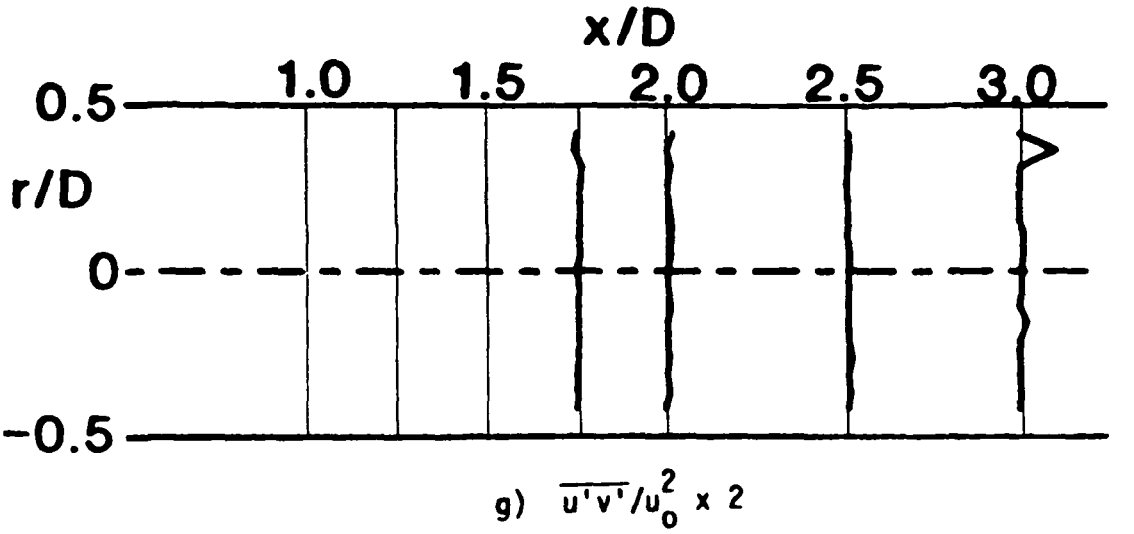

g) $\overline{u'v'}/u_o^2 \times 2$

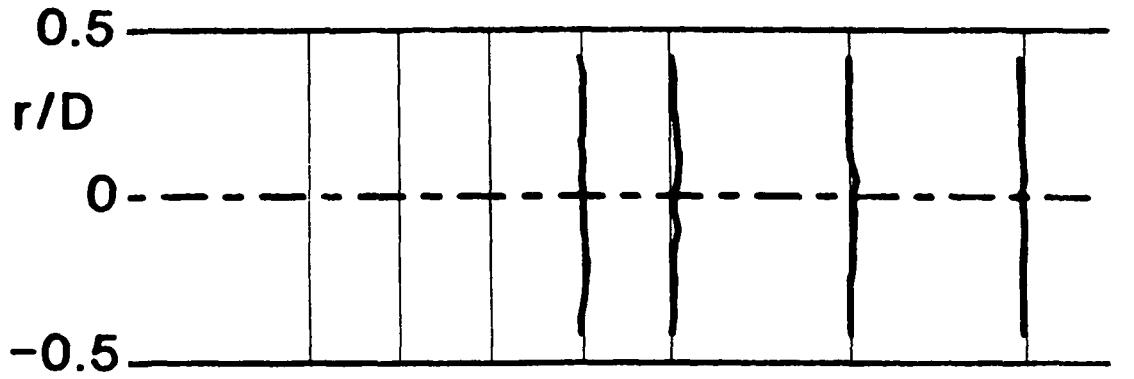

h) $\overline{u'w'}/u_o^2 \times 2$

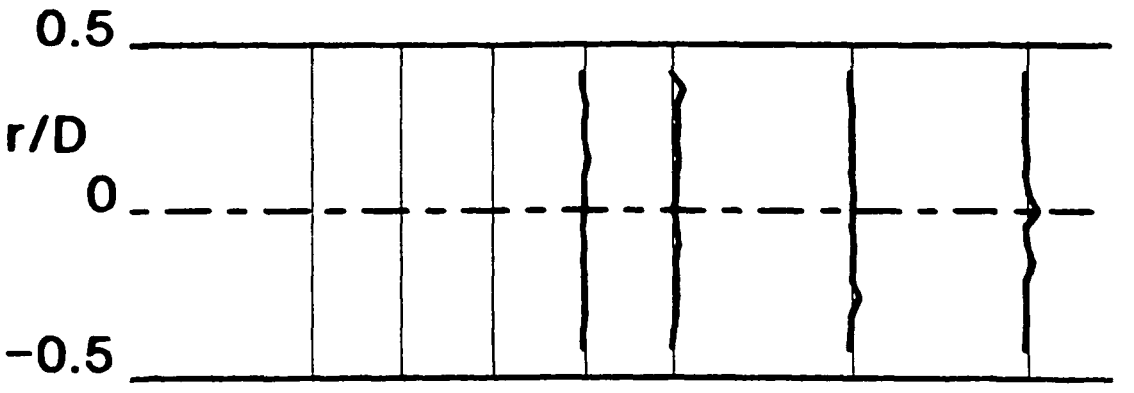

i) $\overline{v'w'}/u_o^2 \times 2$

Figure 15. (Continued)

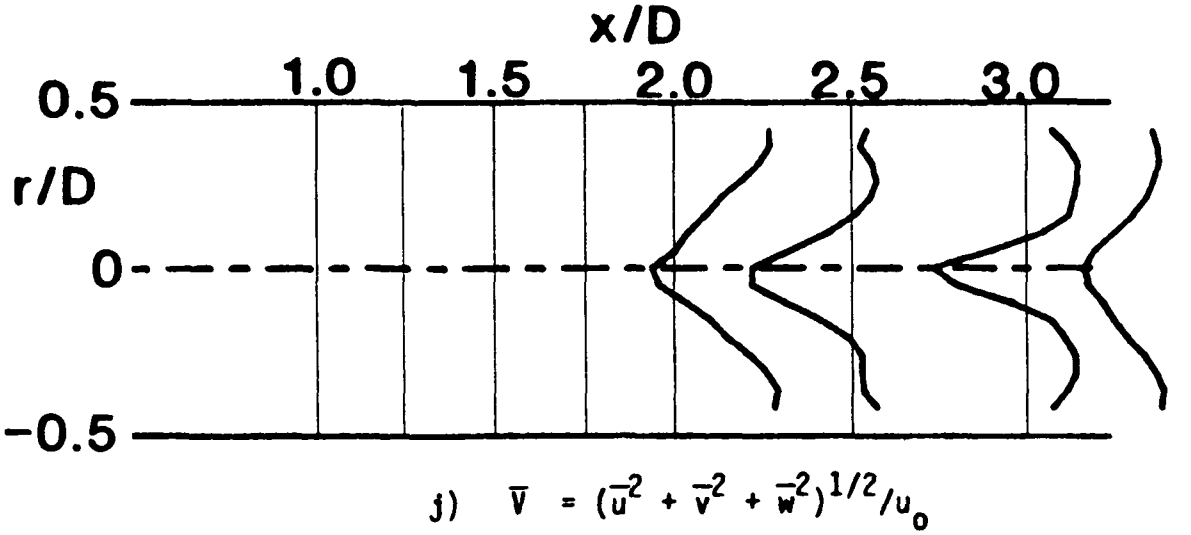

j) $\bar{V} = (\bar{u}^2 + \bar{v}^2 + \bar{w}^2)^{1/2}/u_o$

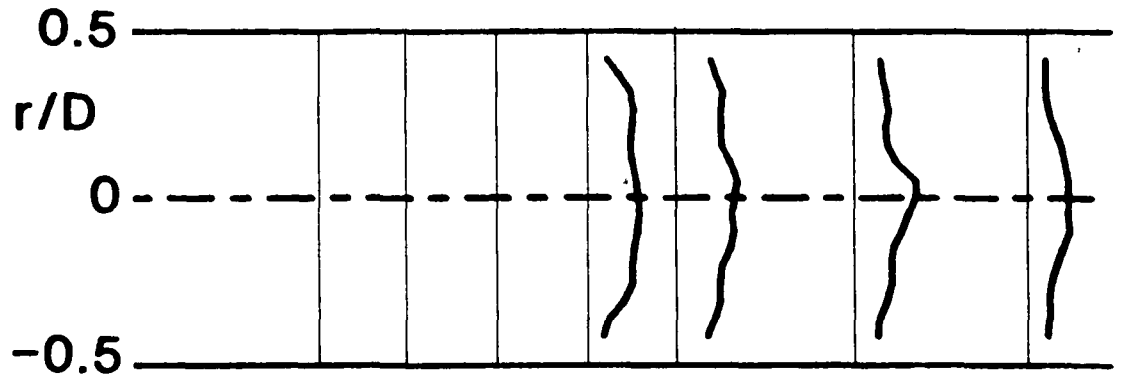

k) $u'_{rms}/\bar{u} \times 2$

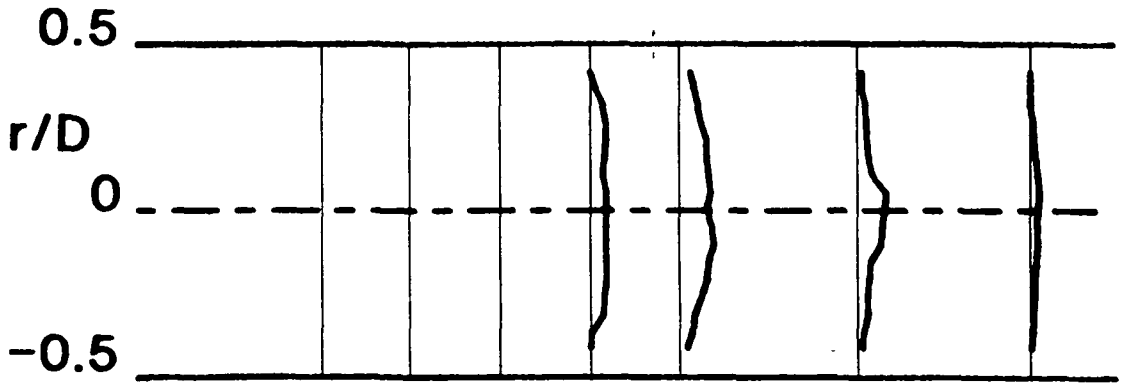

l) $\frac{1}{2}(u'^2_{rms} + v'^2_{rms} + w'^2_{rms})/u_o^2 \times 2$

Figure 15. (Continued)

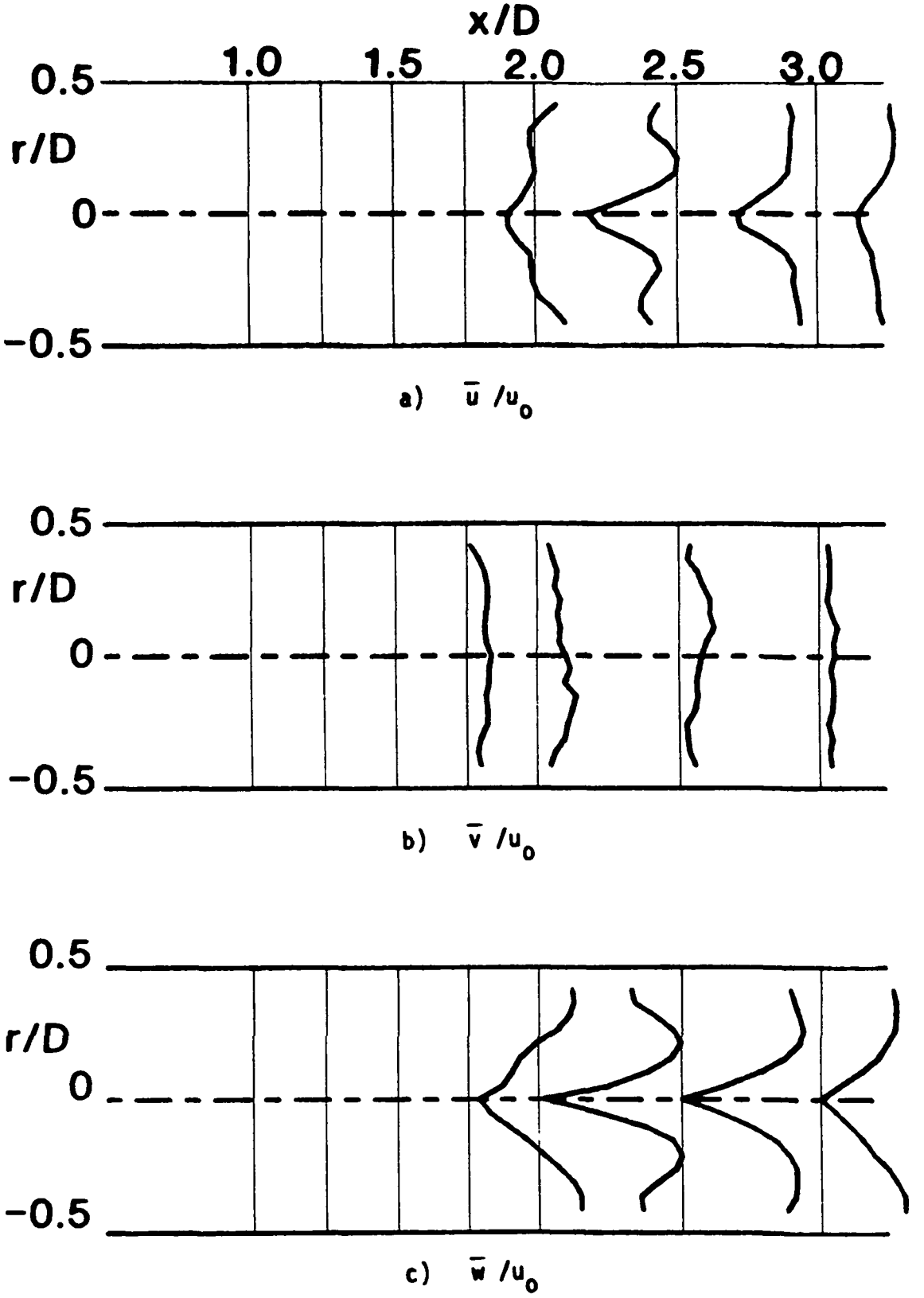

Figure 16. Time-Mean and Turbulent Flowfield, R = 4, ϕ = 45 Degrees, Traverse Angle θ = 330 Degrees.

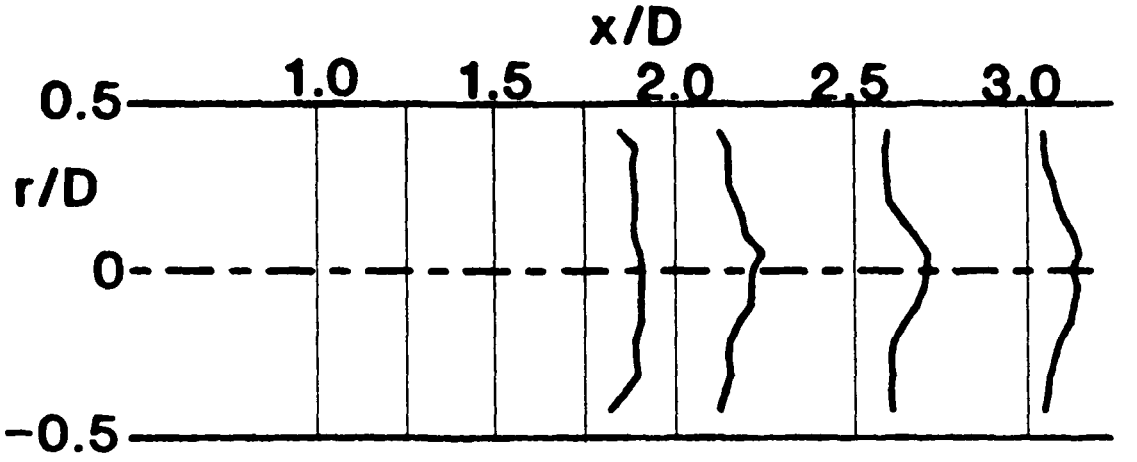

d) u'_{rms}/u_o x 2

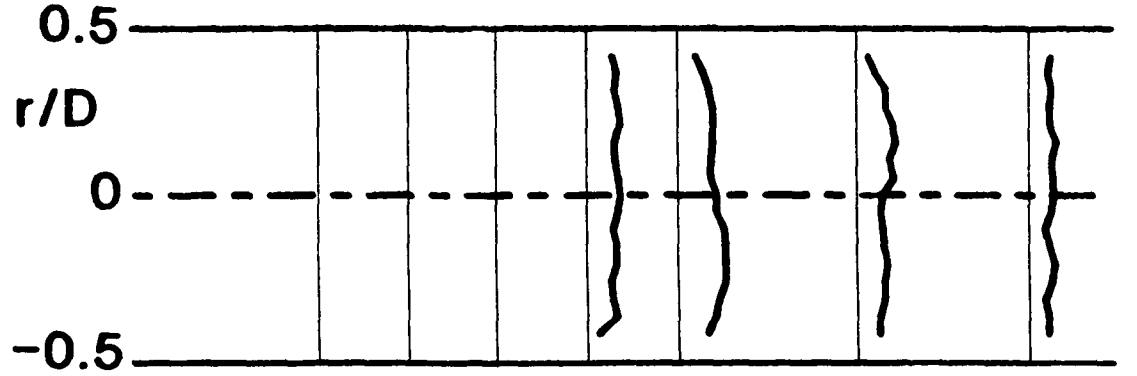

e) v'_{rms}/u_o x 2

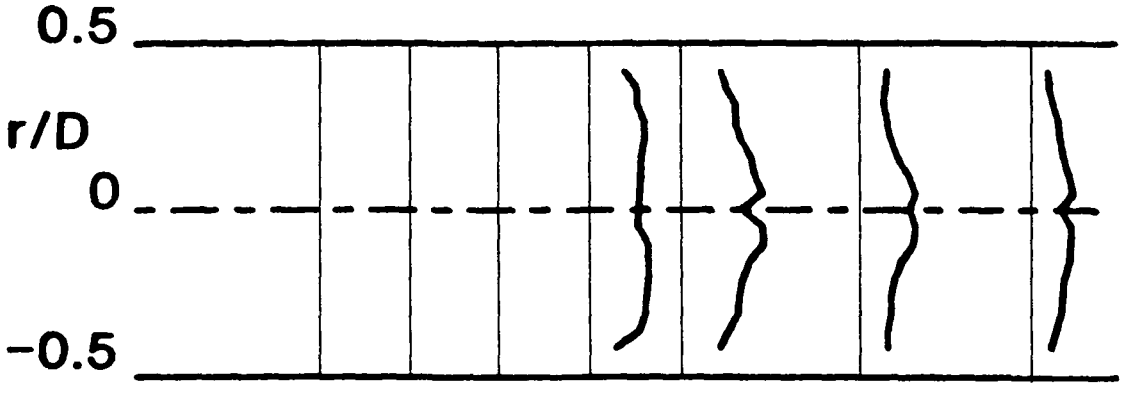

f) w'_{rms}/u_o x 2

Figure 16. (Continued)

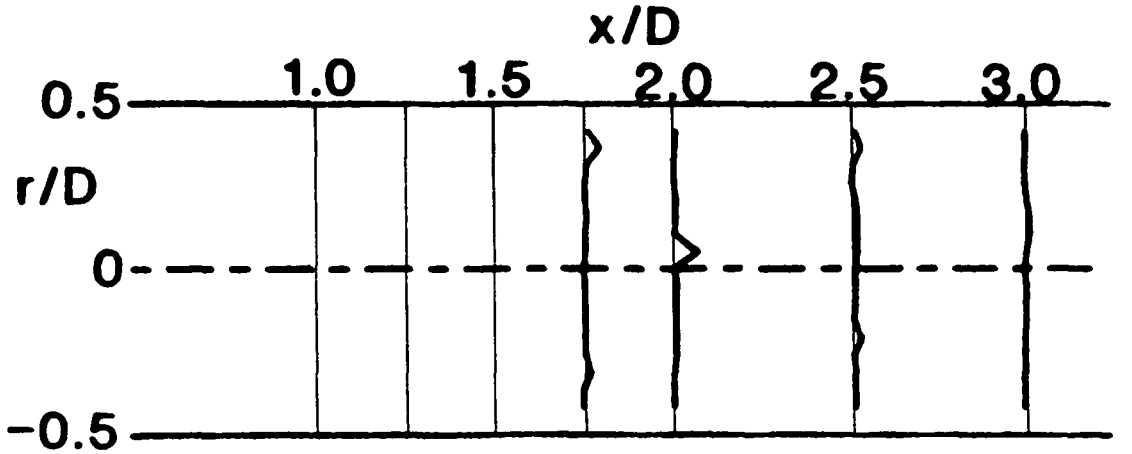

g) $\overline{u'v'}/u_o^2 \times 2$

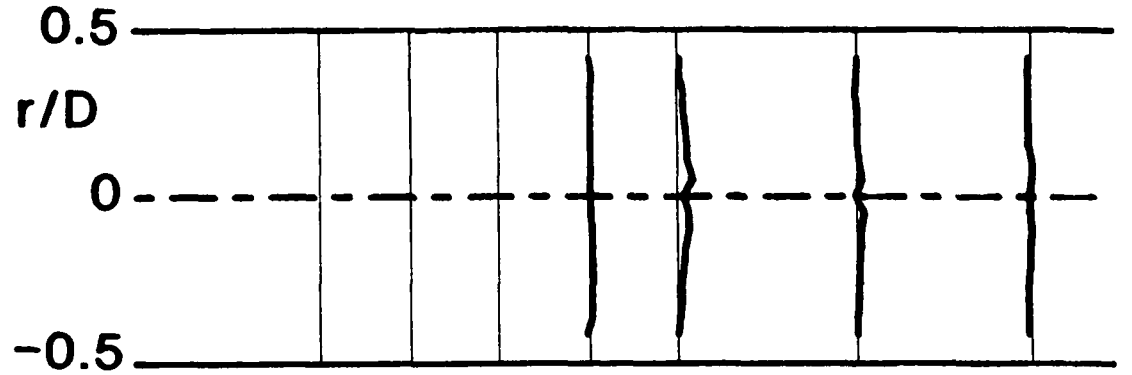

h) $\overline{u'w'}/u_o^2 \times 2$

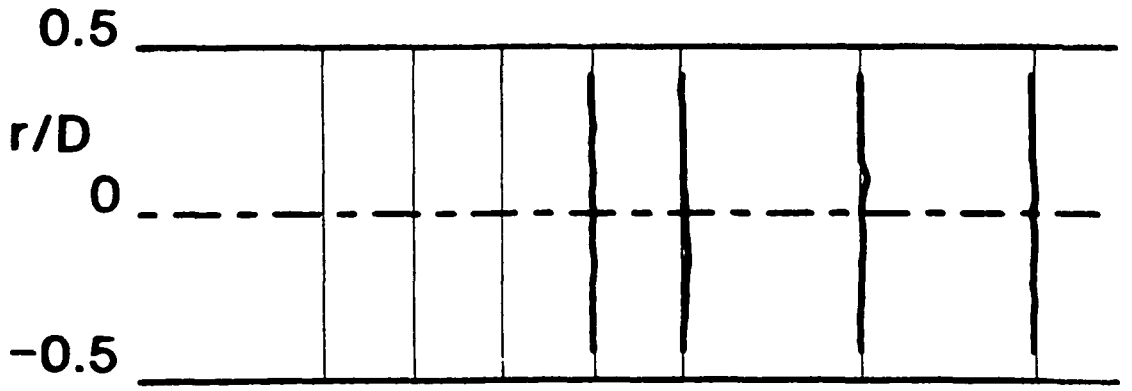

i) $\overline{v'w'}/u_o^2 \times 2$

Figure 16. (Continued)

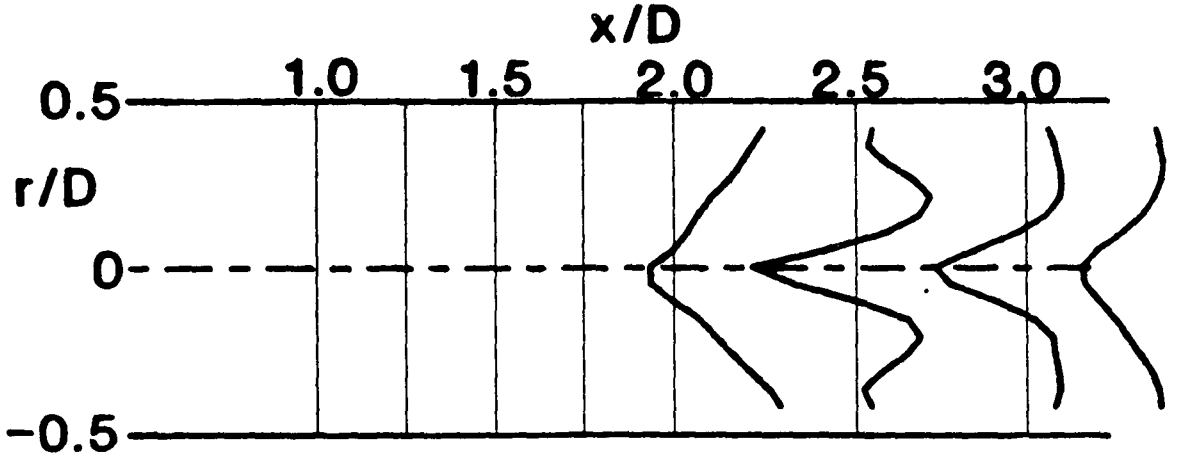

j) $\bar{V} = (\bar{u}^2 + \bar{v}^2 + \bar{w}^2)^{1/2}/u_o$

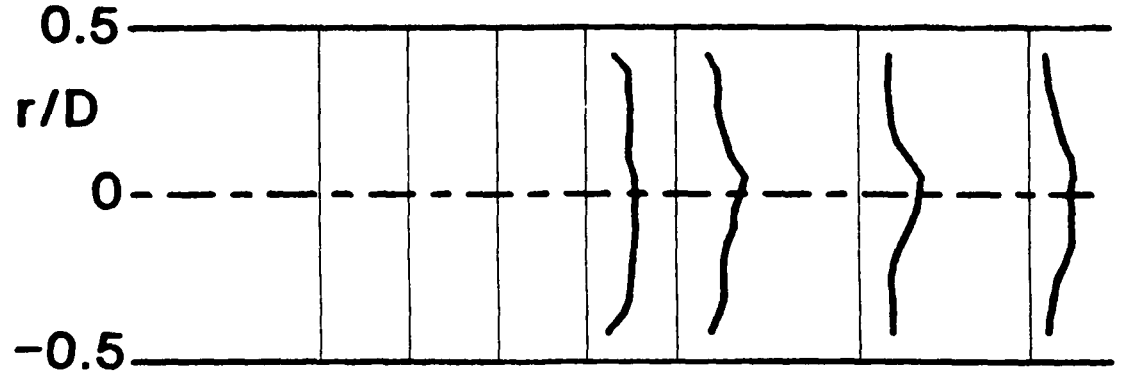

k) $u'_{rms}/\bar{u} \times 2$

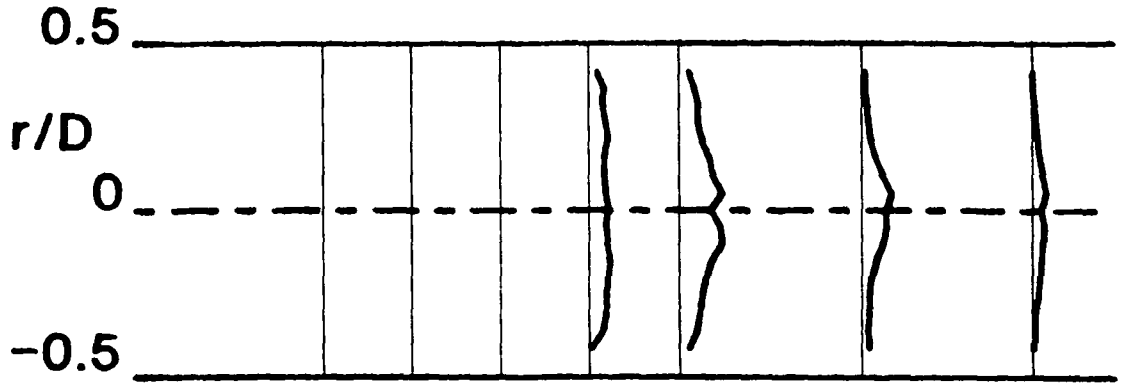

l) $\frac{1}{2}(u'^2_{rms} + v'^2_{rms} + w'^2_{rms})/u_o^2 \times 2$

Figure 16. (Continued)

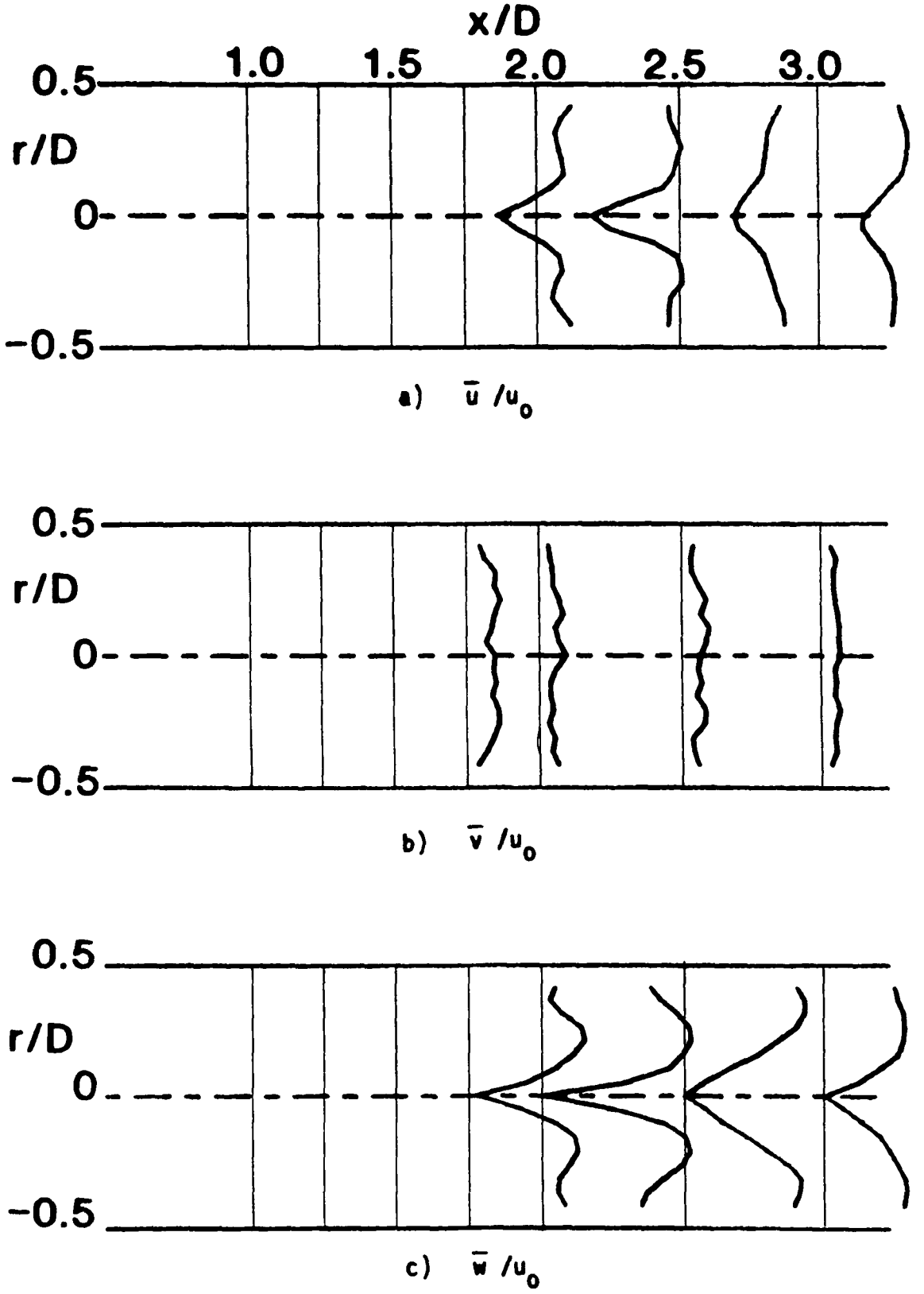

Figure 17. Time-Mean and Turbulent Flowfield, R = 4, ϕ = 45 Degrees, Traverse Angle θ = 0 Degrees.

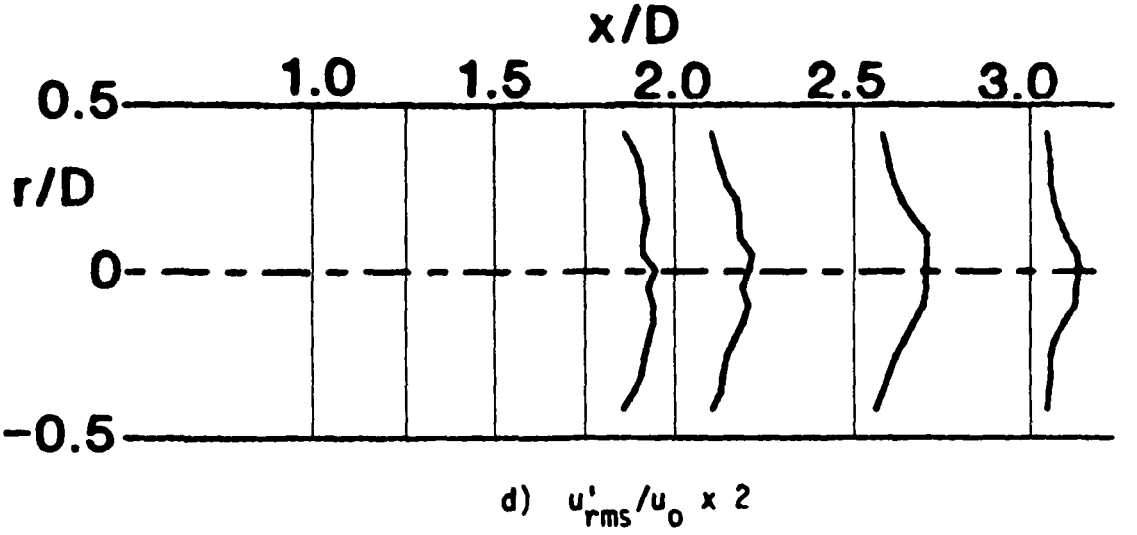

d) u'_{rms}/u_o x 2

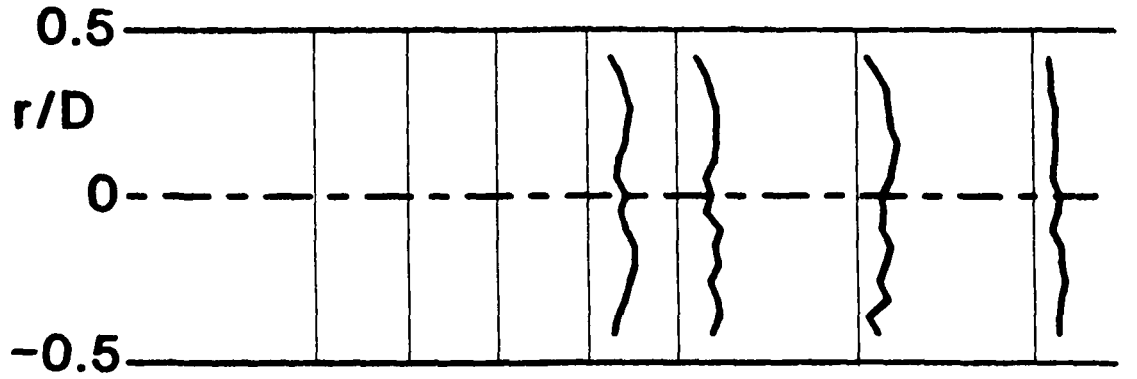

e) v'_{rms}/u_o x 2

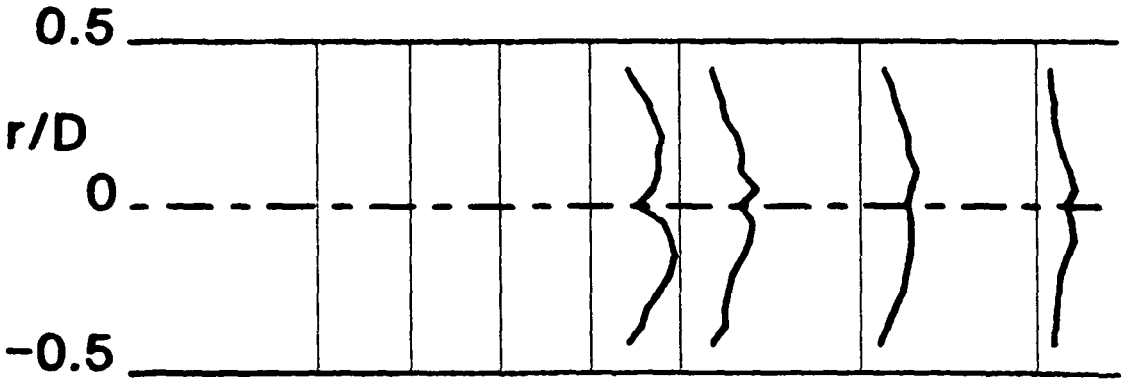

f) w'_{rms}/u_o x 2

Figure 17. (Continued)

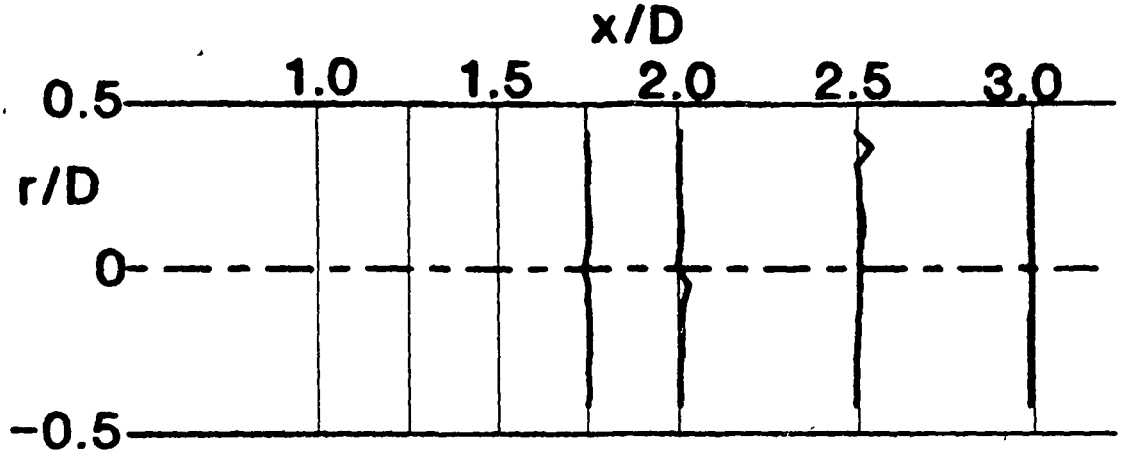

g) $\overline{u'v'}/u_o^2 \times 2$

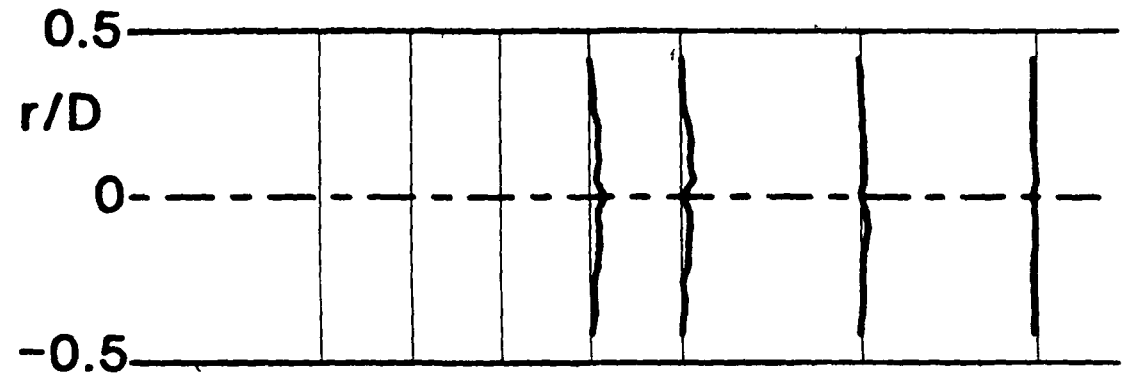

h) $\overline{u'w'}/u_o^2 \times 2$

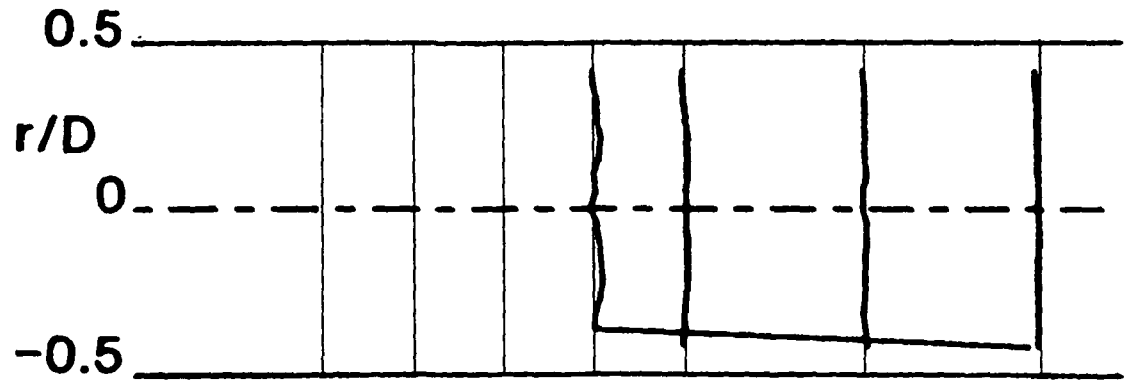

i) $\overline{v'w'}/u_o^2 \times 2$

Figure 17. (Continued)

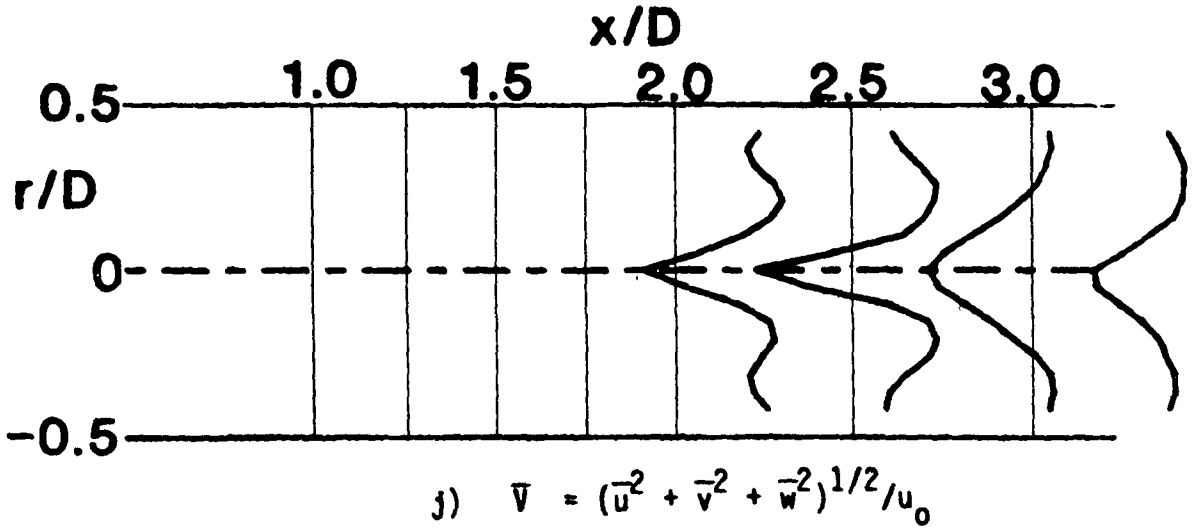

j) $\bar{V} = (\bar{u}^2 + \bar{v}^2 + \bar{w}^2)^{1/2}/u_o$

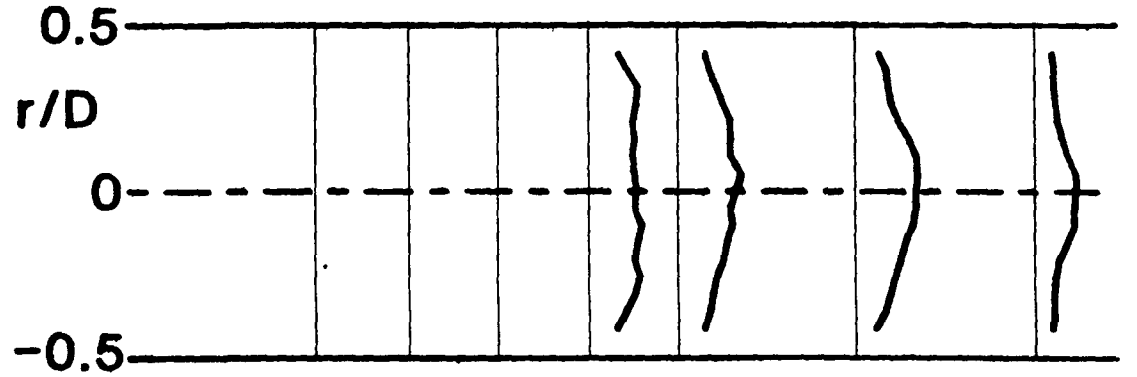

k) $u'_{rms}/\bar{u} \times 2$

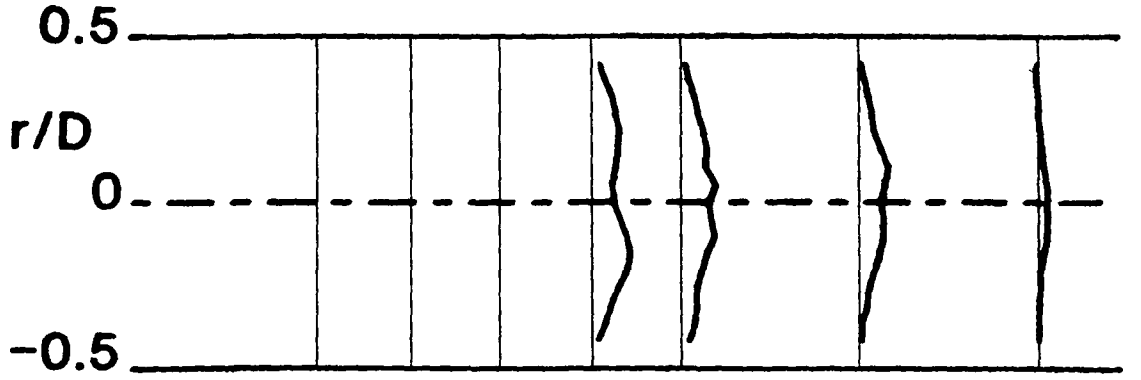

l) $\frac{1}{2}(u'^2_{rms} + v'^2_{rms} + w'^2_{rms})/u_o^2 \times 2$

Figure 17. (Continued)

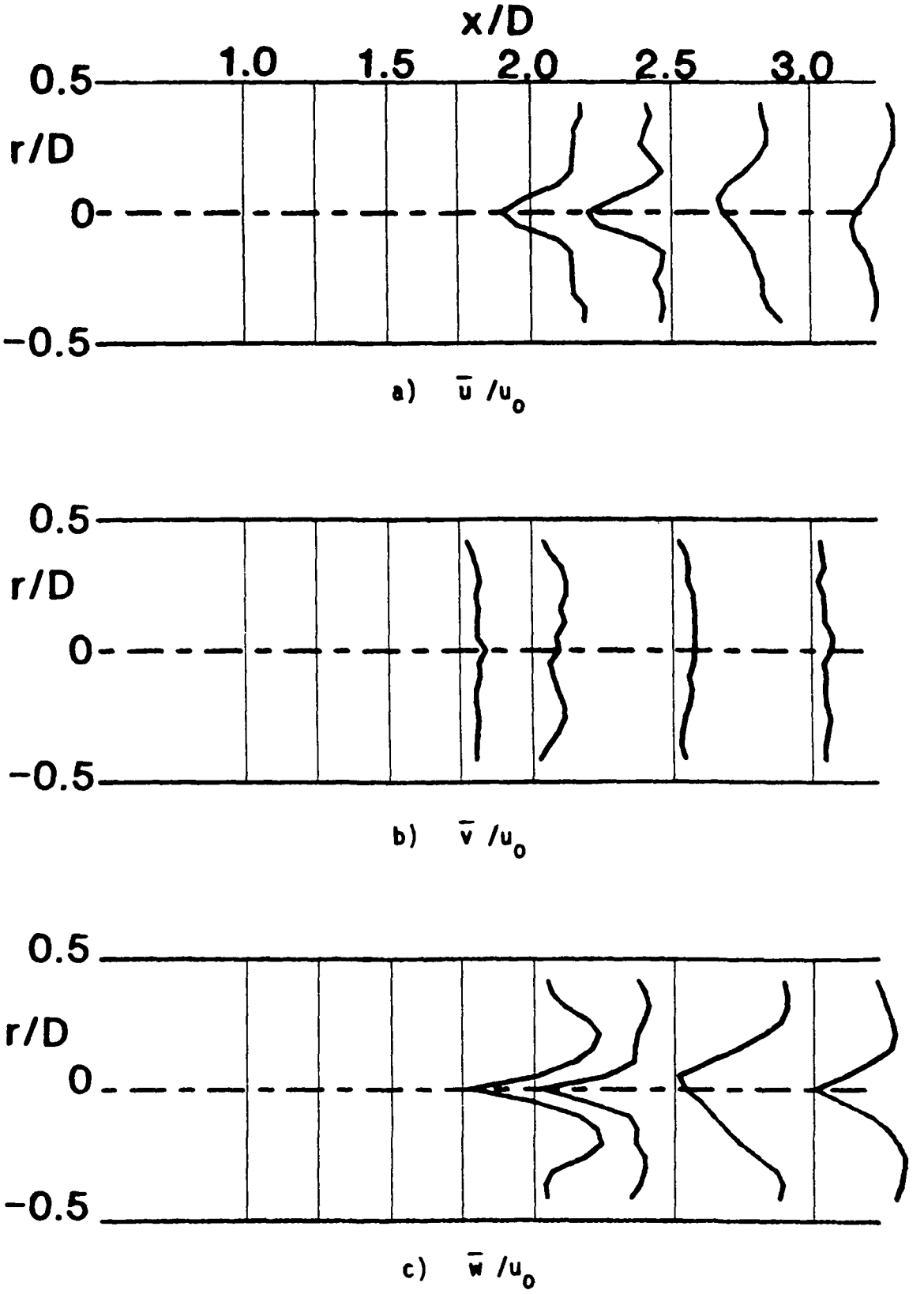

Figure 18. Time-Mean and Turbulent Flowfield, R = 4, ϕ = 45 Degrees, Traverse Angle θ = 30 Degrees.

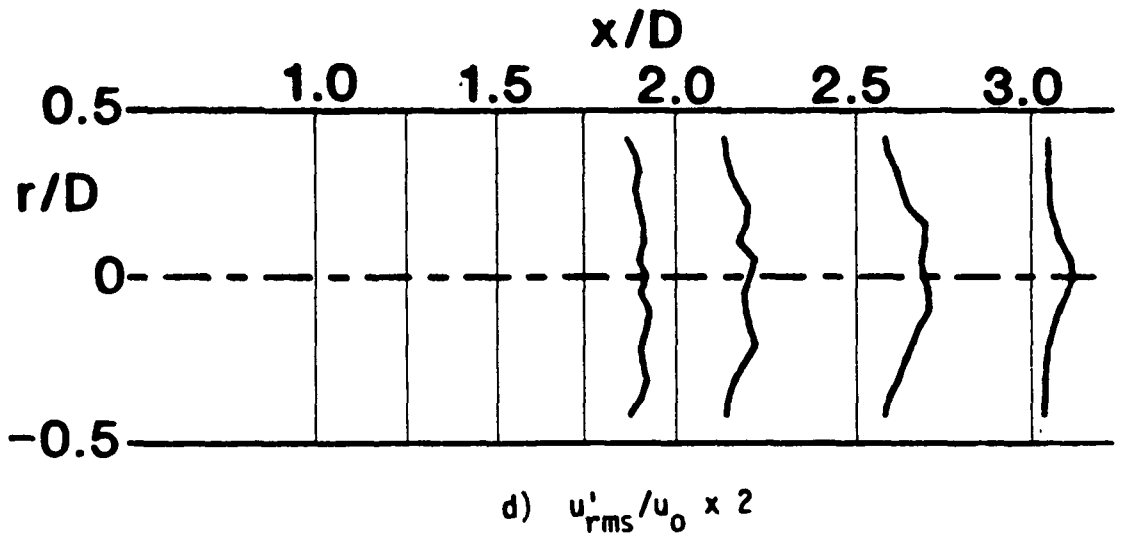

d) u'_{rms}/u_o x 2

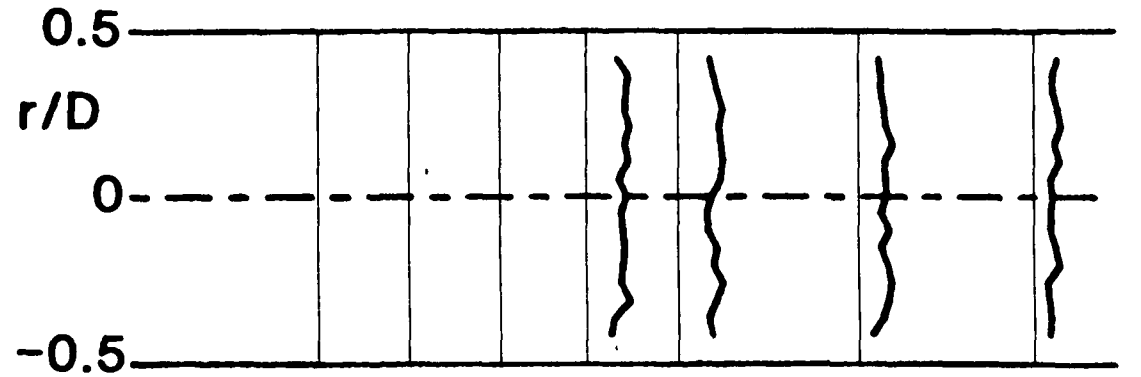

e) v'_{rms}/u_o x 2

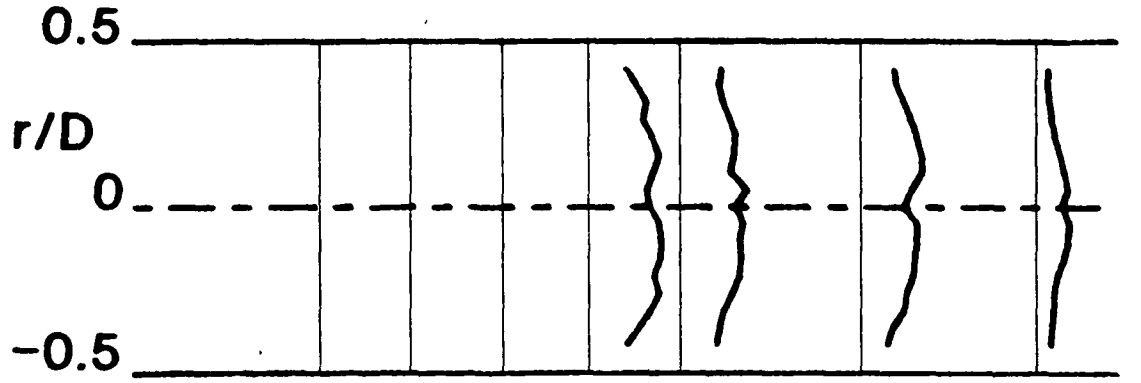

f) w'_{rms}/u_o x 2

Figure 18. (Continued)

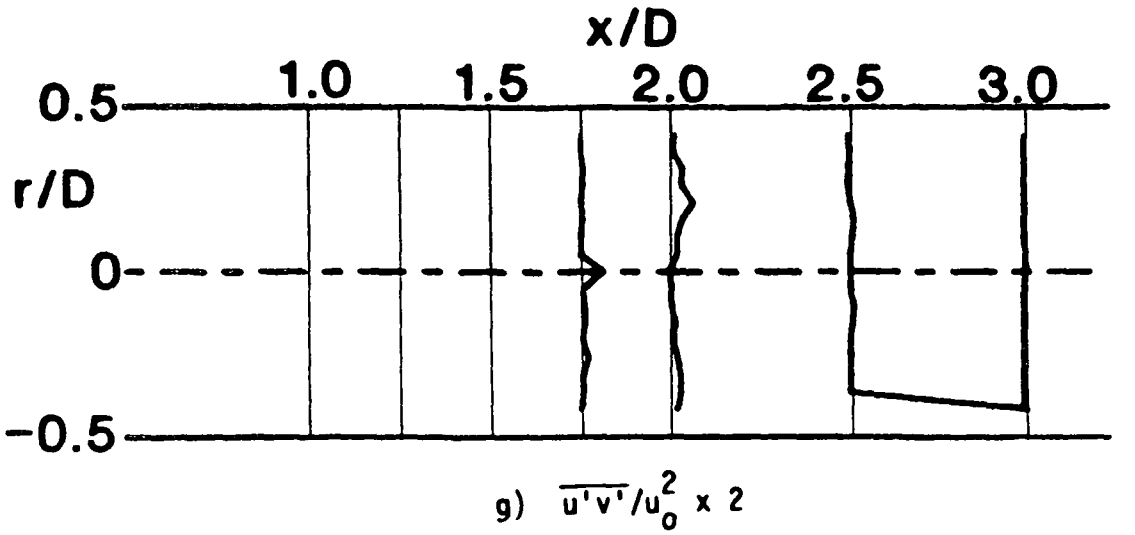

g) $\overline{u'v'}/u_o^2 \times 2$

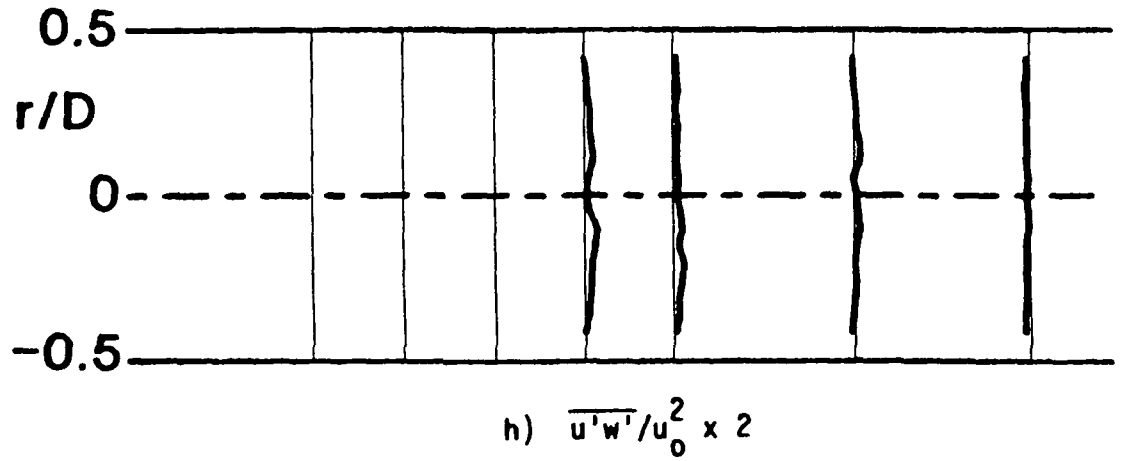

h) $\overline{u'w'}/u_o^2 \times 2$

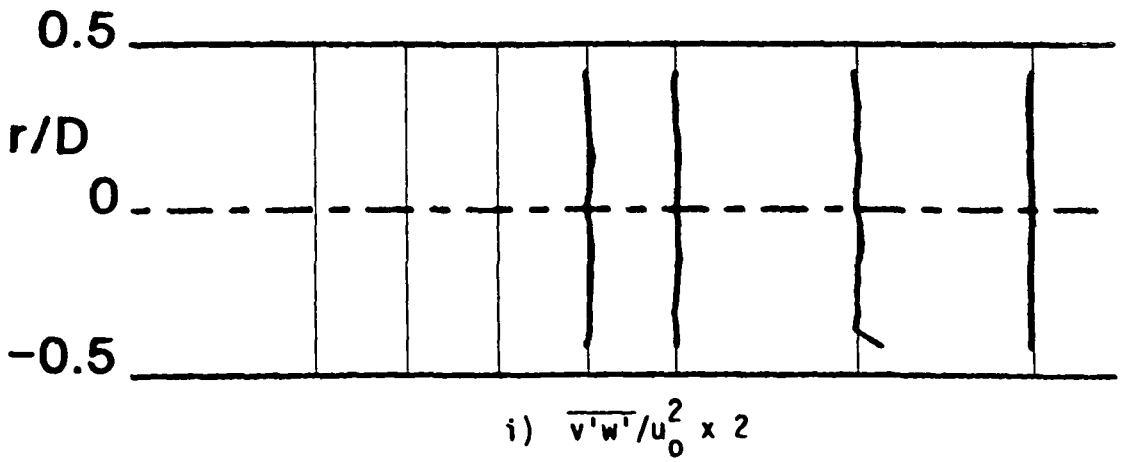

i) $\overline{v'w'}/u_o^2 \times 2$

Figure 18. (Continued)

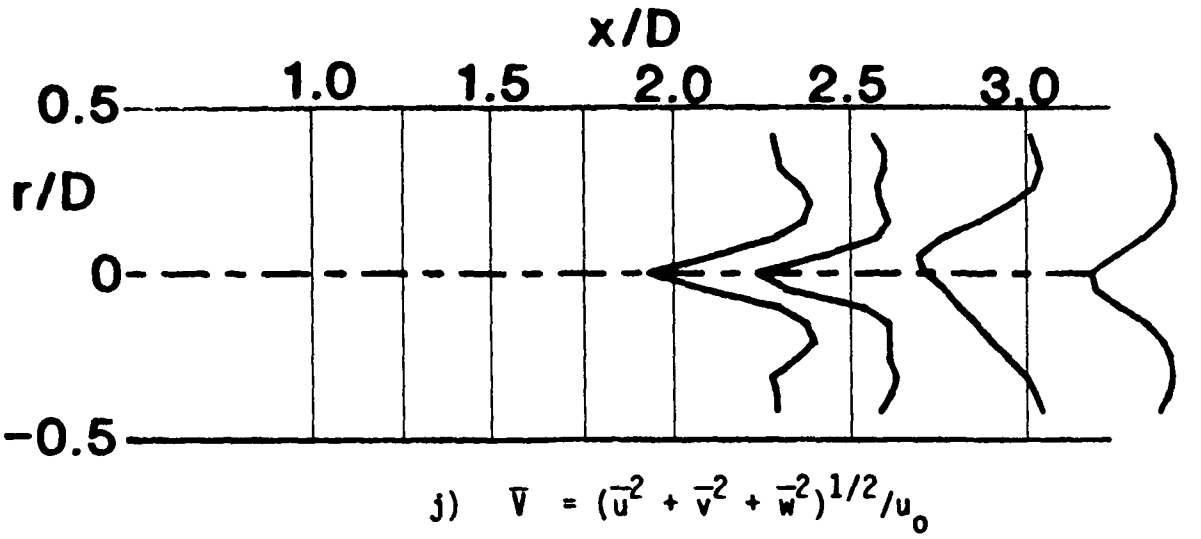

j) $\bar{V} = (\bar{u}^2 + \bar{v}^2 + \bar{w}^2)^{1/2}/u_o$

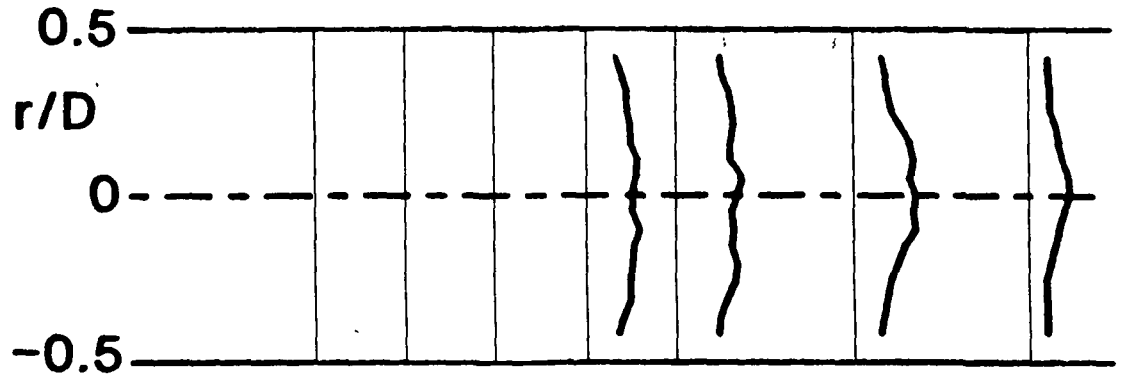

k) $u'_{rms}/\bar{u} \times 2$

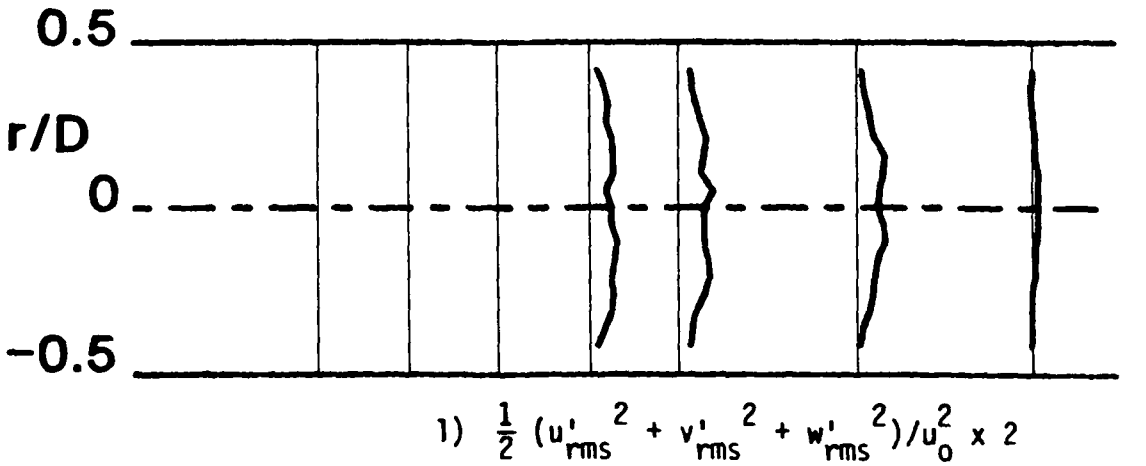

l) $\frac{1}{2}(u'^2_{rms} + v'^2_{rms} + w'^2_{rms})/u_o^2 \times 2$

Figure 18. (Continued)

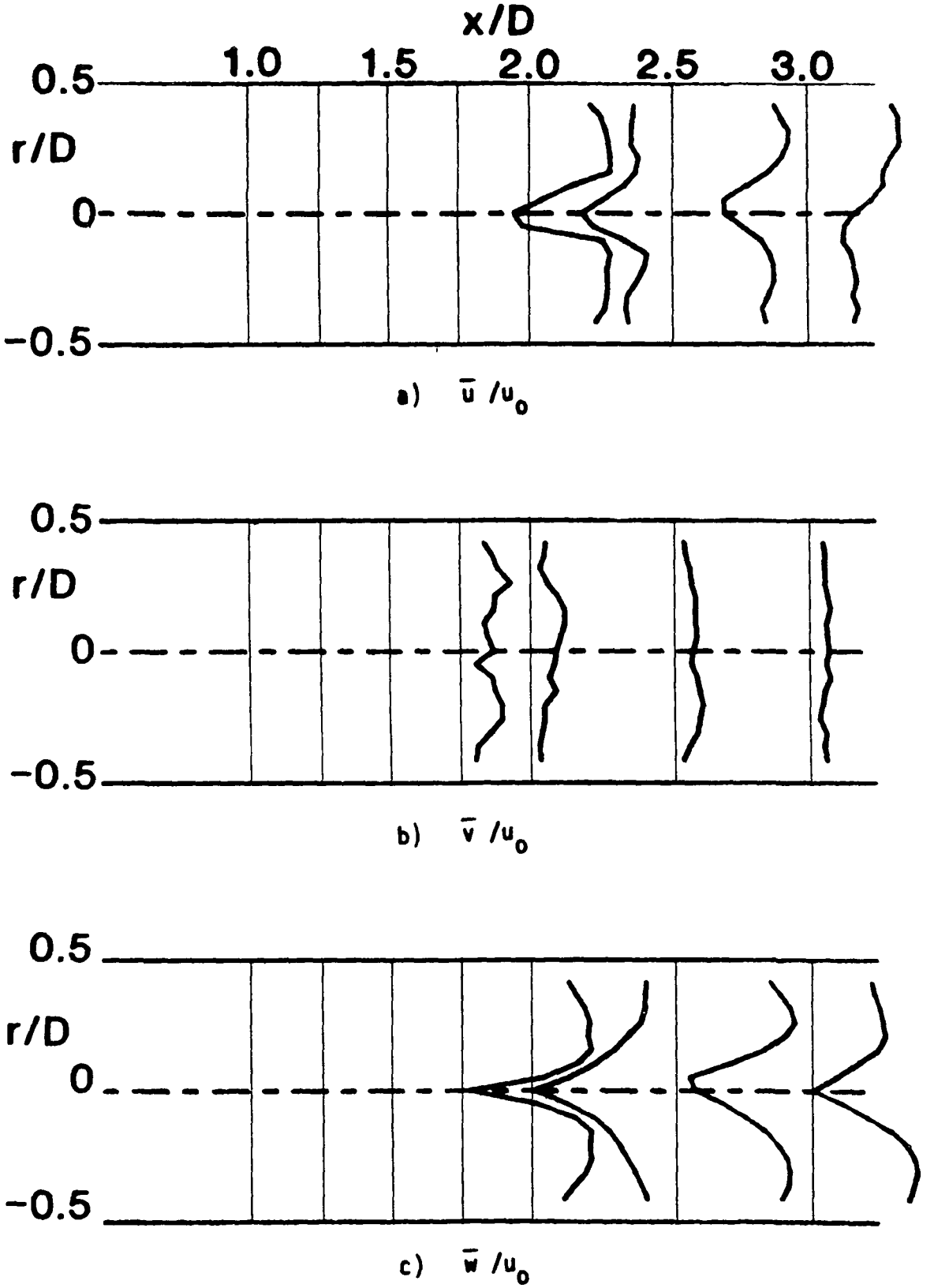

Figure 19. Time-Mean and Turbulent Flowfield, R = 4, ϕ = 45 Degrees, Traverse Angle θ = 60 Degrees.

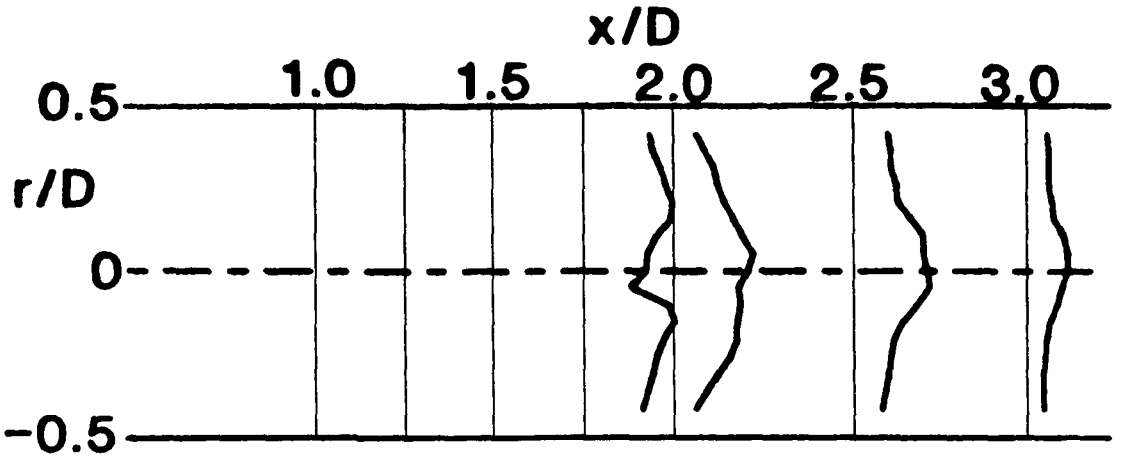

d) $u'_{rms}/u_o \times 2$

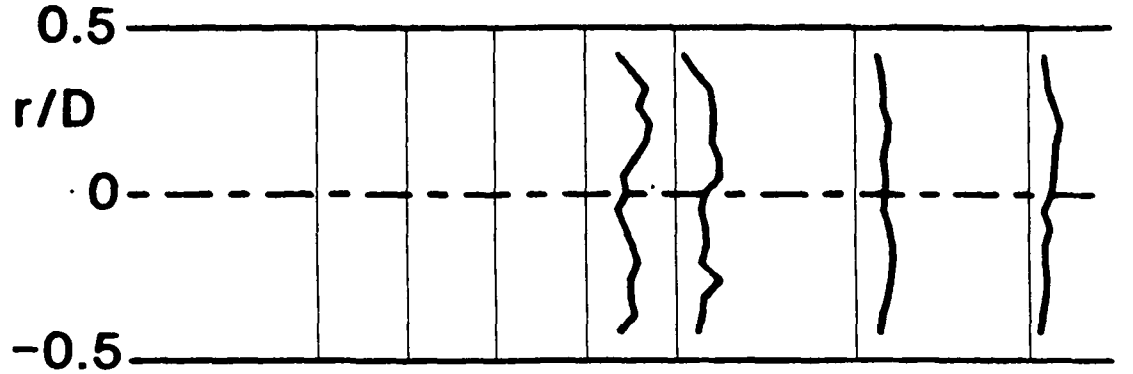

e) $v'_{rms}/u_o \times 2$

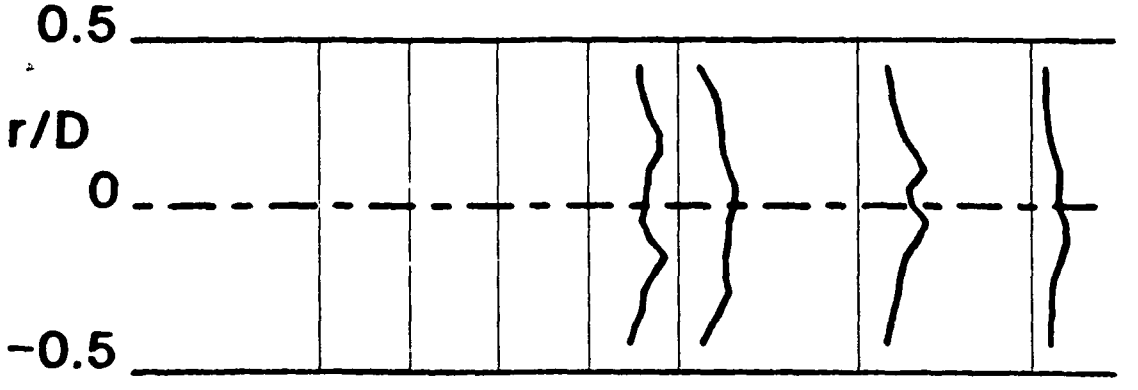

f) $w'_{rms}/u_o \times 2$

Figure 19. (Continued)

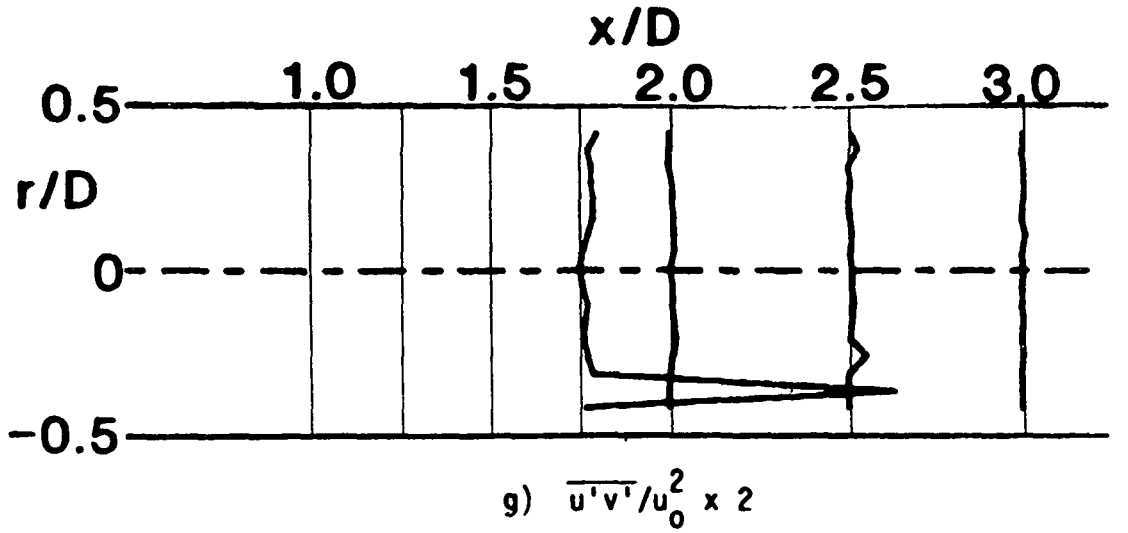

g) $\overline{u'v'}/u_o^2 \times 2$

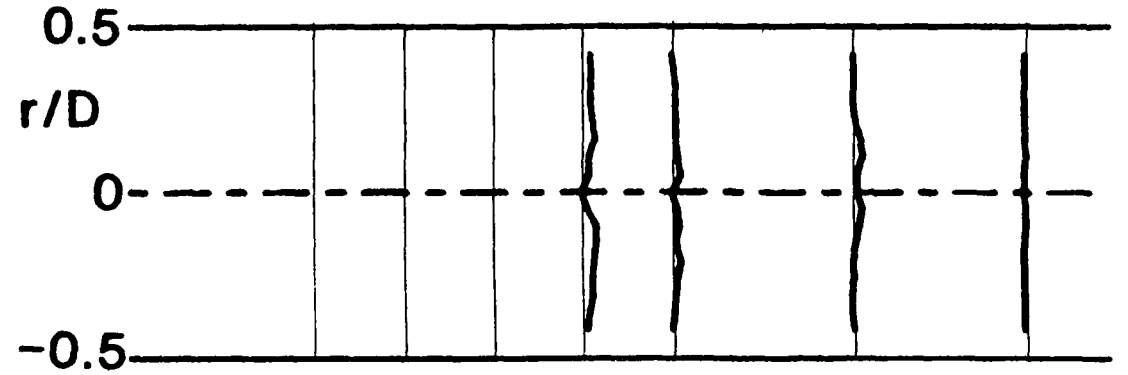

h) $\overline{u'w'}/u_o^2 \times 2$

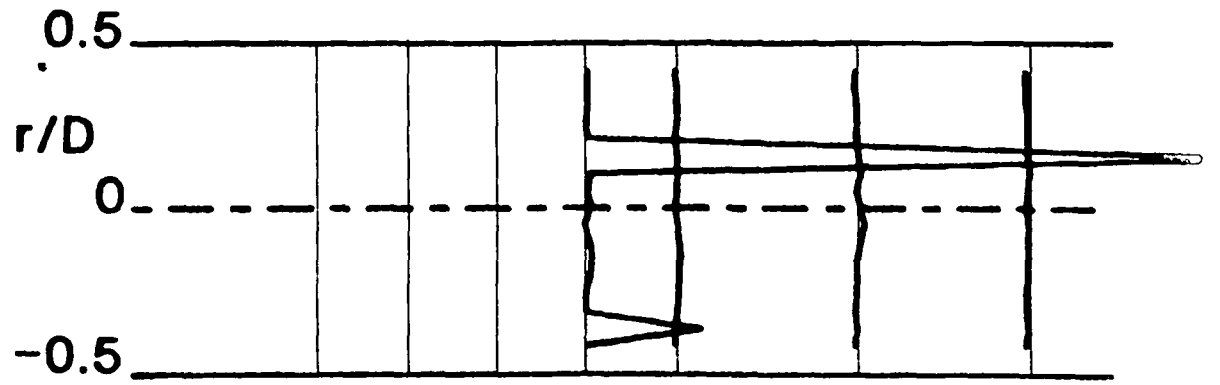

i) $\overline{v'w'}/u_o^2 \times 2$

Figure 19. (Continued)

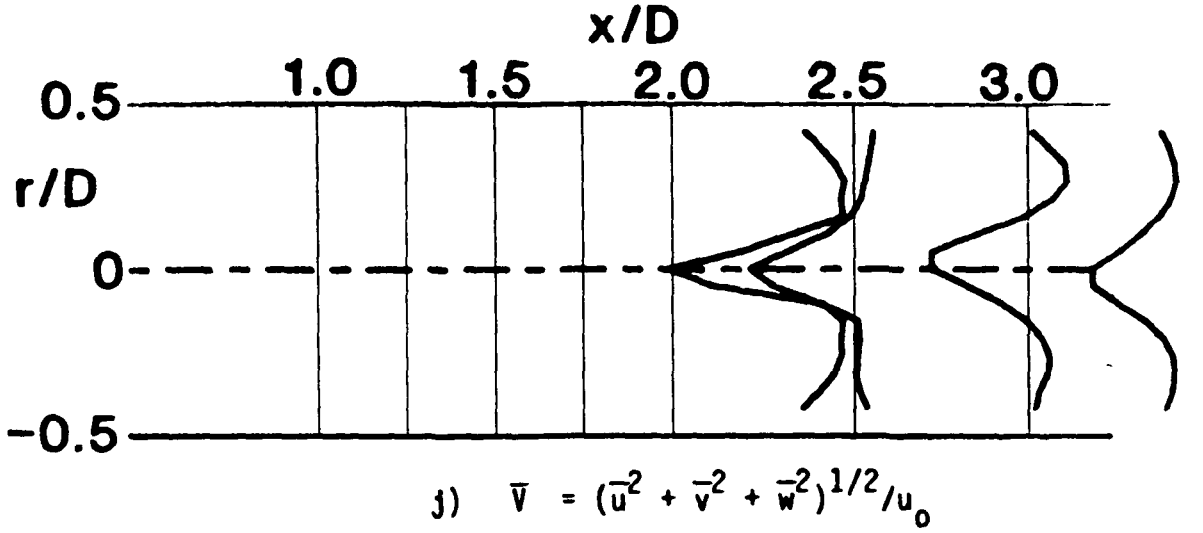

j) $\bar{V} = (\bar{u}^2 + \bar{v}^2 + \bar{w}^2)^{1/2}/u_o$

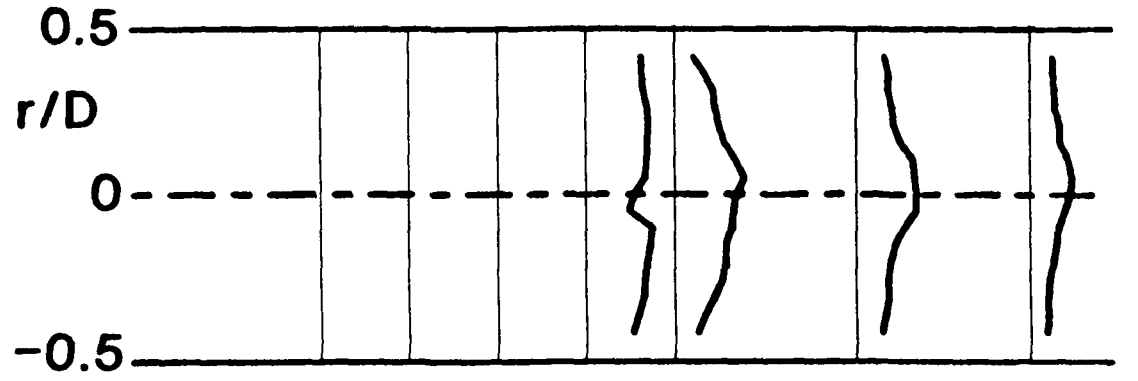

k) $u'_{rms}/\bar{u} \times 2$

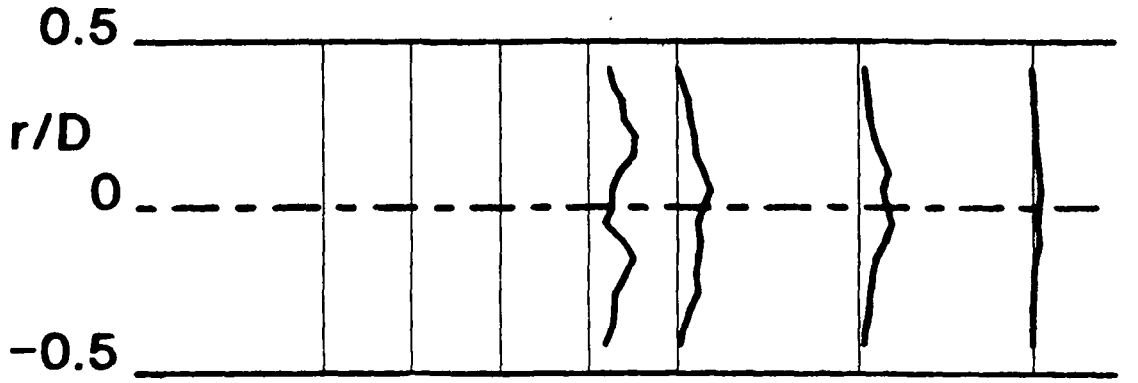

l) $\frac{1}{2}(u'^2_{rms} + v'^2_{rms} + w'^2_{rms})/u_o^2 \times 2$

Figure 19. (Continued)

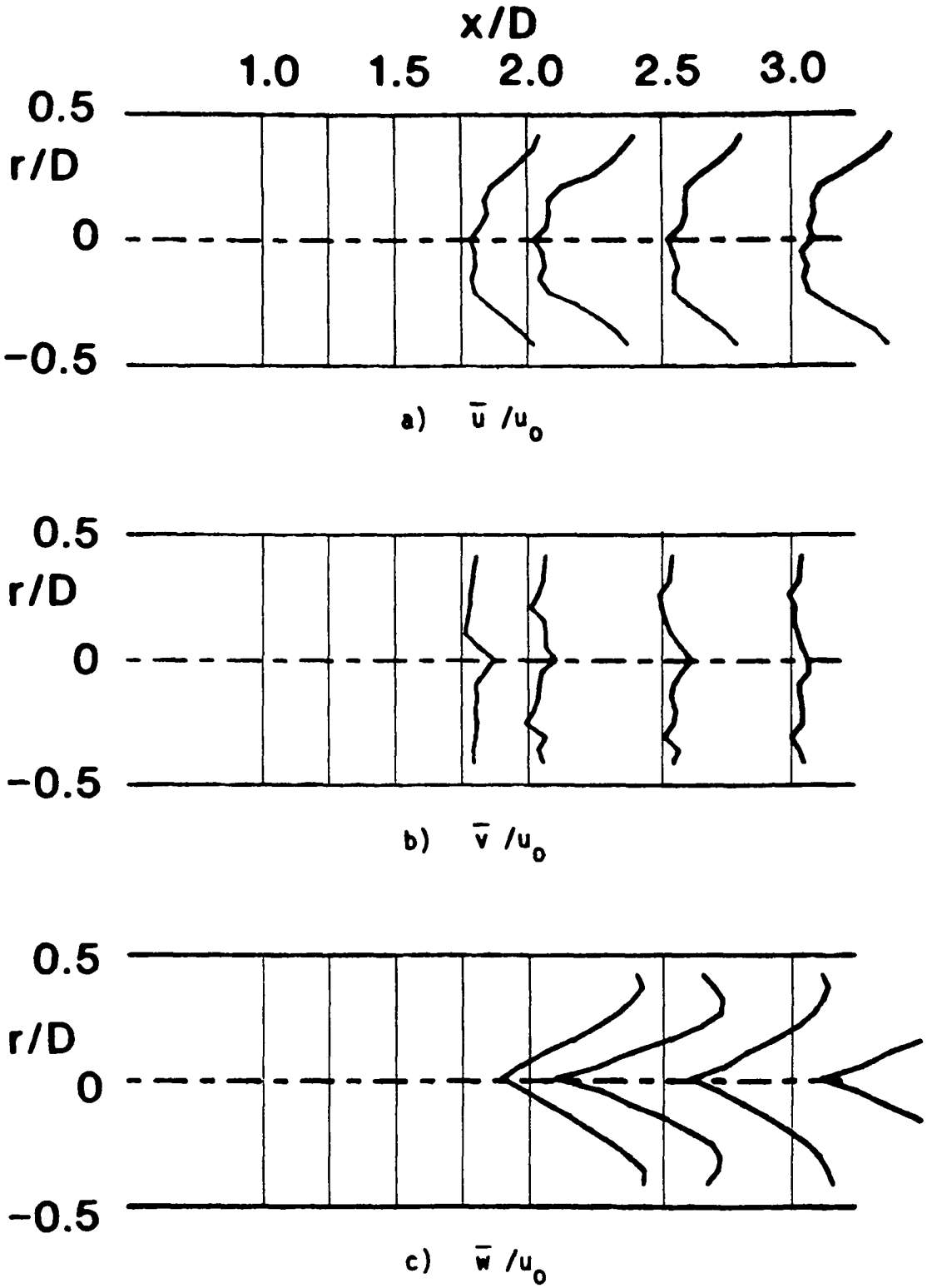

Figure 20. Time-Mean and Turbulent Flowfield, R = 4, ϕ = 70 Degrees, Traverse Angle θ = 270 Degrees.

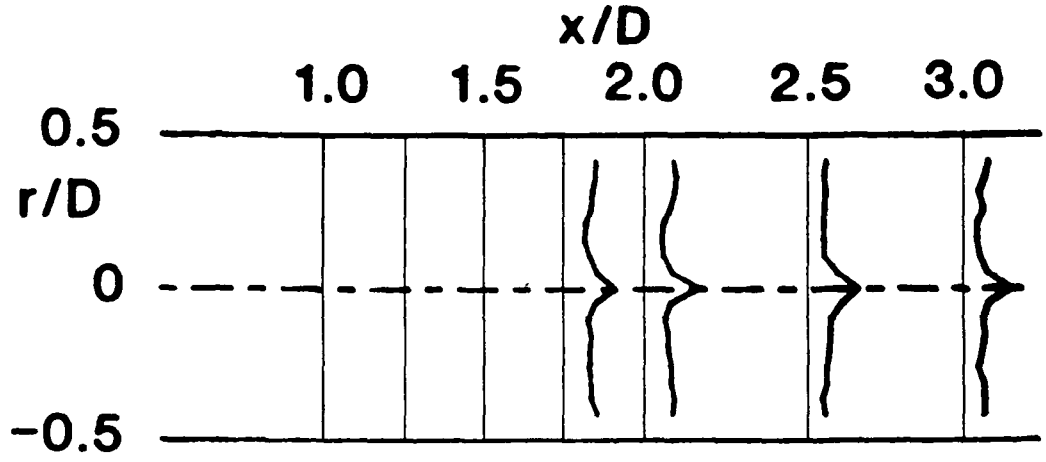

d) u'_{rms}/u_o x 2

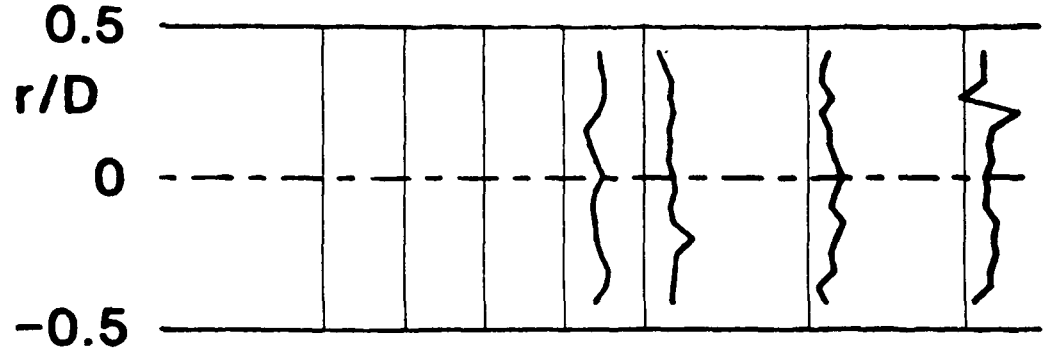

e) v'_{rms}/u_o x 2

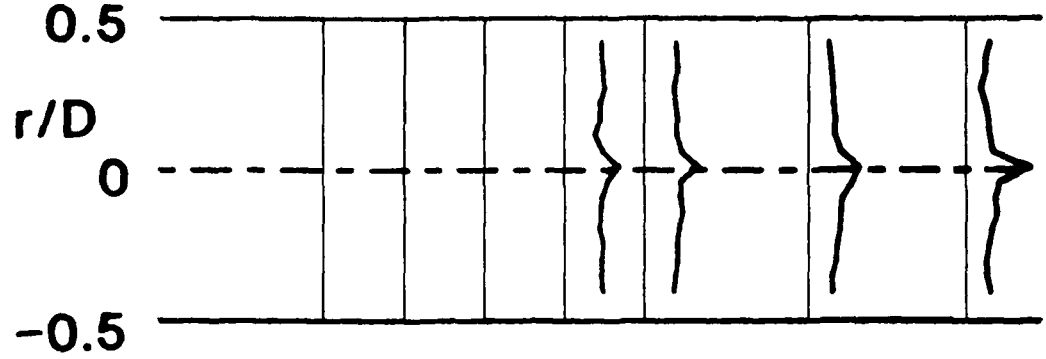

f) w'_{rms}/u_o x 2

Figure 20. (Continued)

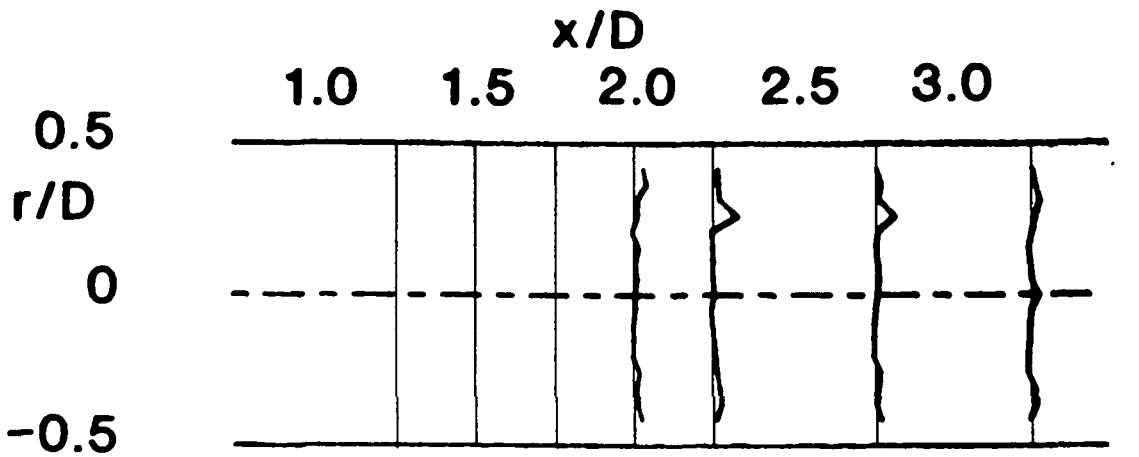

g) $\overline{u'v'}/u_o^2 \times 2$

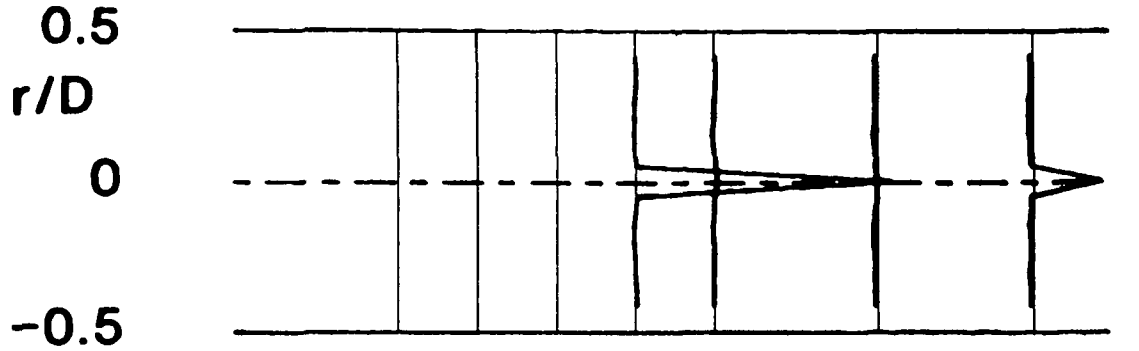

h) $\overline{u'w'}/u_o^2 \times 2$

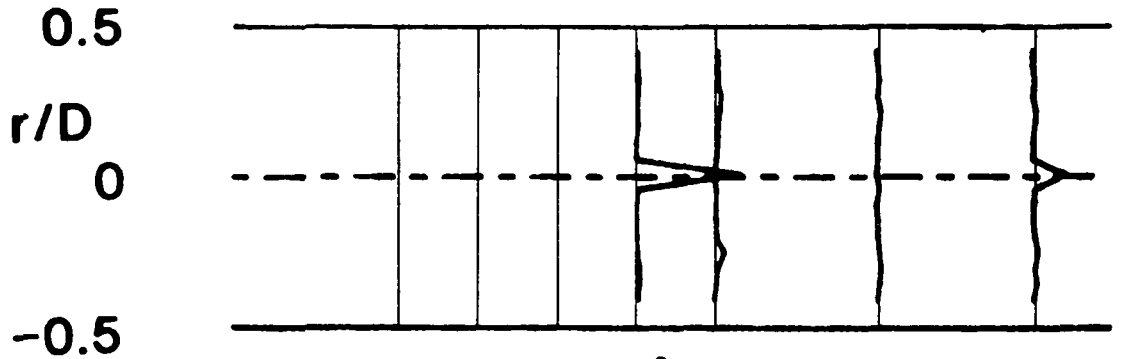

i) $\overline{v'w'}/u_o^2 \times 2$

Figure 20. (Continued)

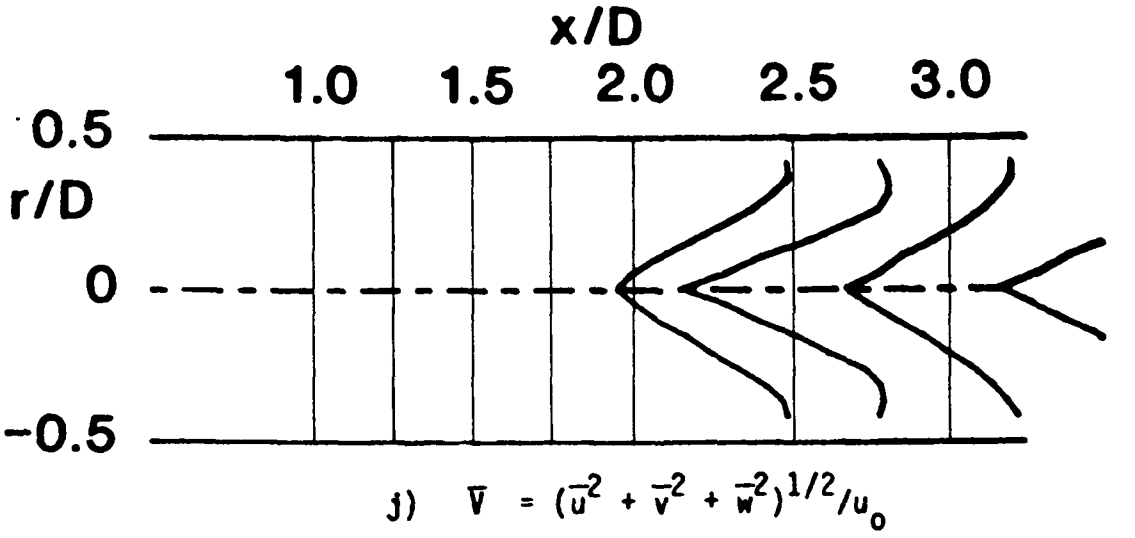

j) $\bar{V} = (\bar{u}^2 + \bar{v}^2 + \bar{w}^2)^{1/2}/u_o$

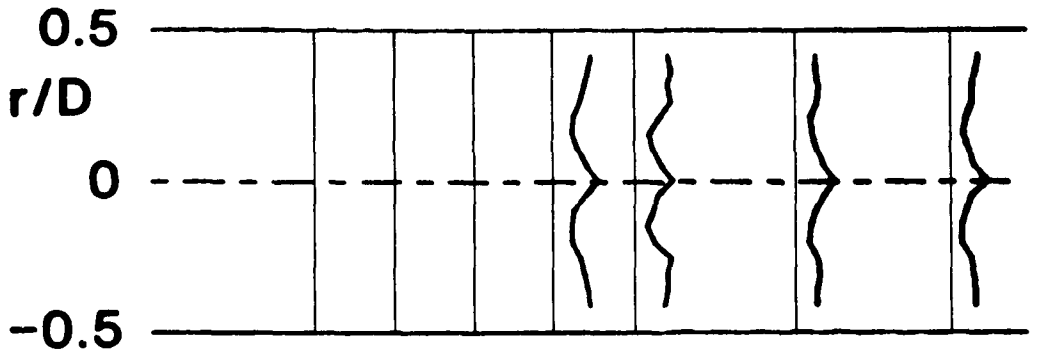

k) $u'_{rms}/\bar{u} \times 2$

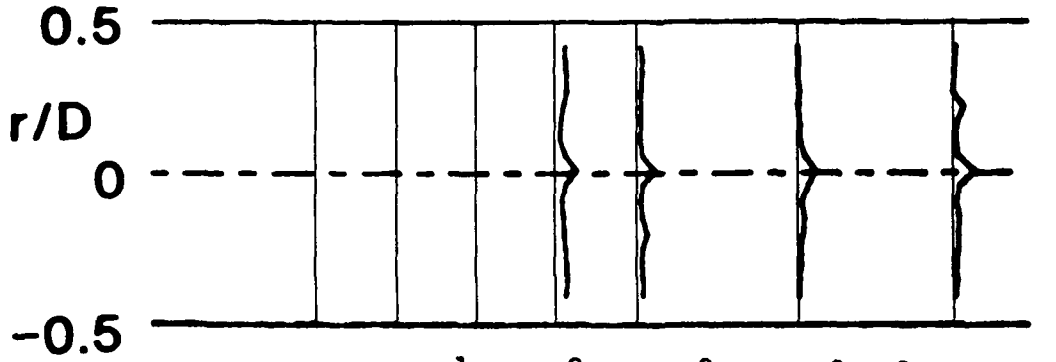

l) $\frac{1}{2}(u'^2_{rms} + v'^2_{rms} + w'^2_{rms})/u_o^2 \times 2$

Figure 20. (Continued)

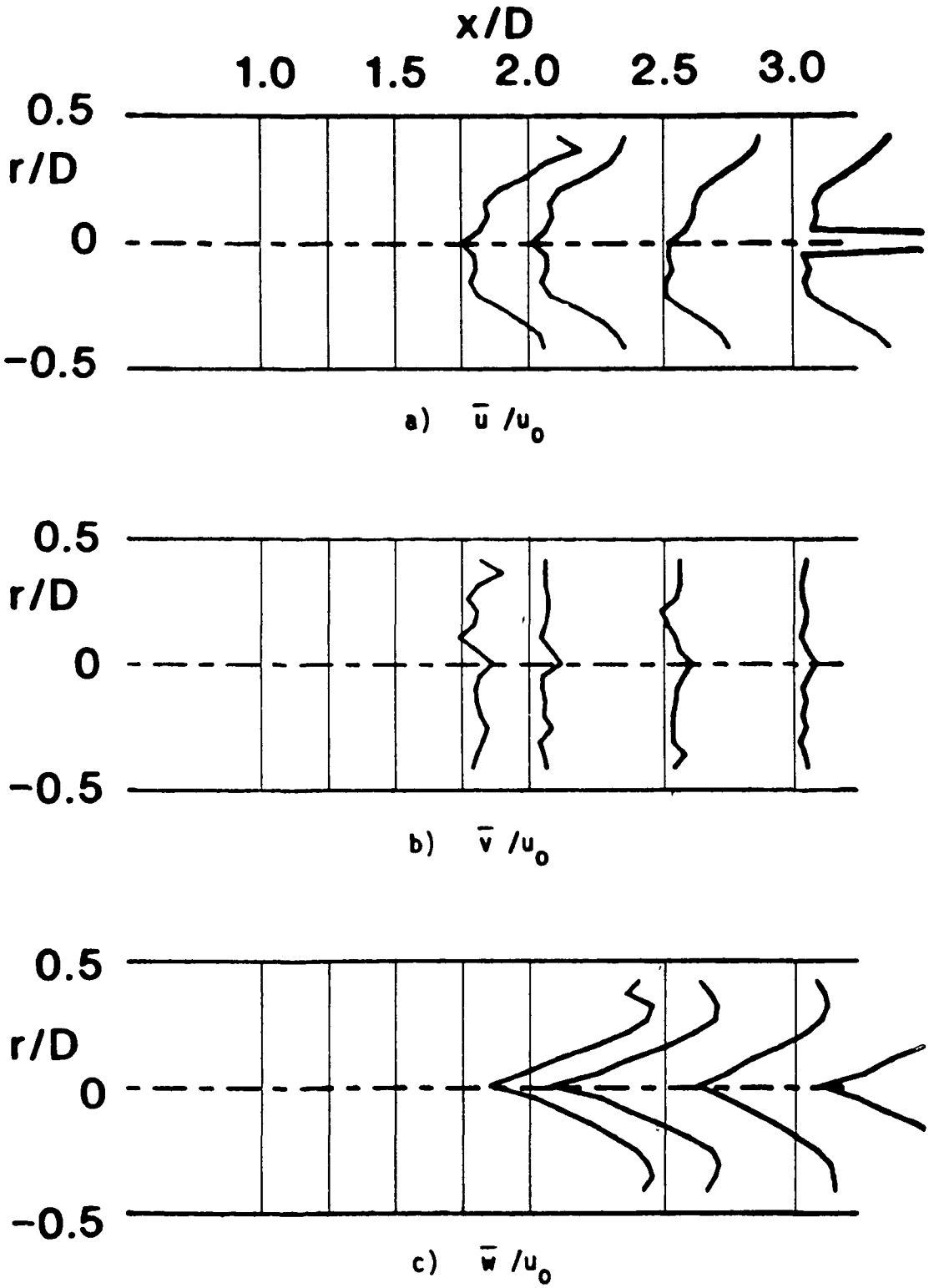

Figure 21. Time-Mean and Turbulent Flowfield, R = 4, ϕ = 70 Degrees, Traverse Angle θ = 300 Degrees.

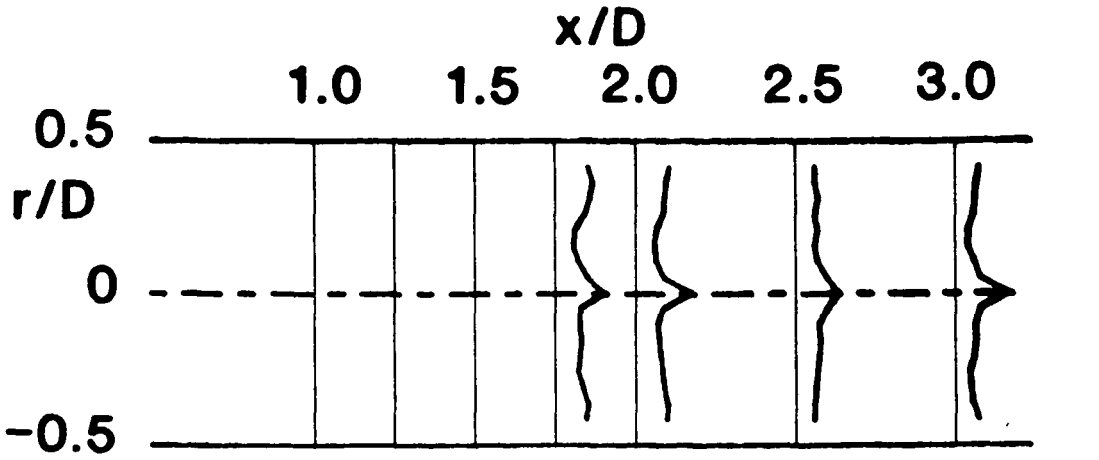

d) u'_{rms}/u_o x 2

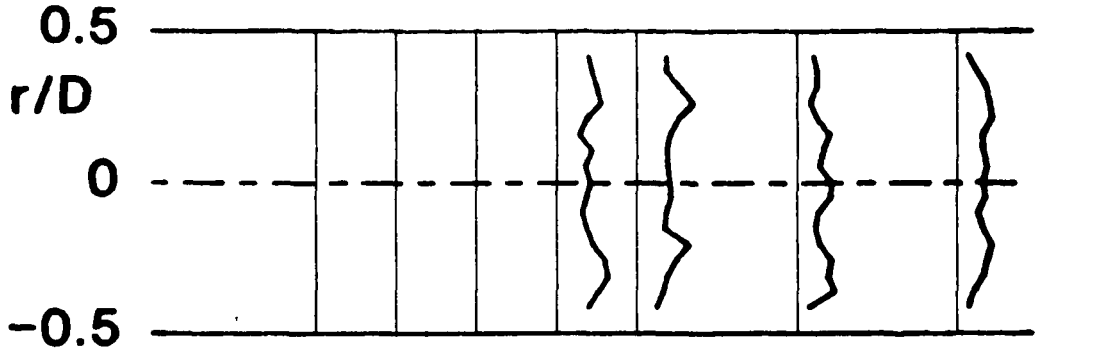

e) v'_{rms}/u_o x 2

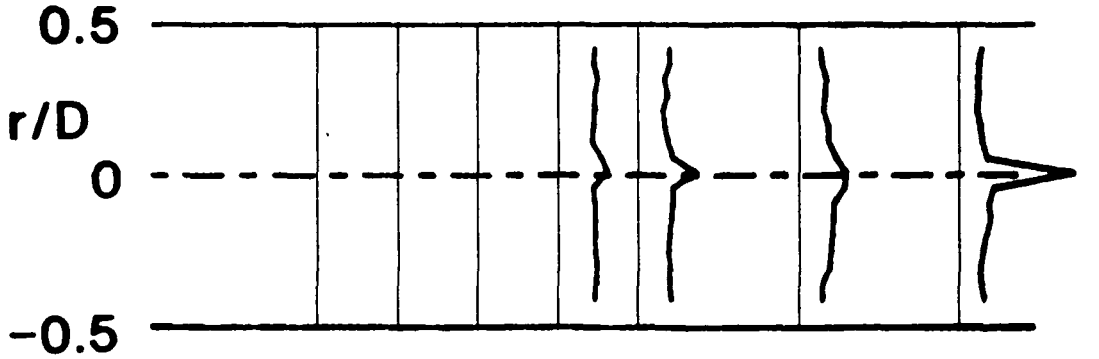

f) w'_{rms}/u_o x 2

Figure 21. (Continued)

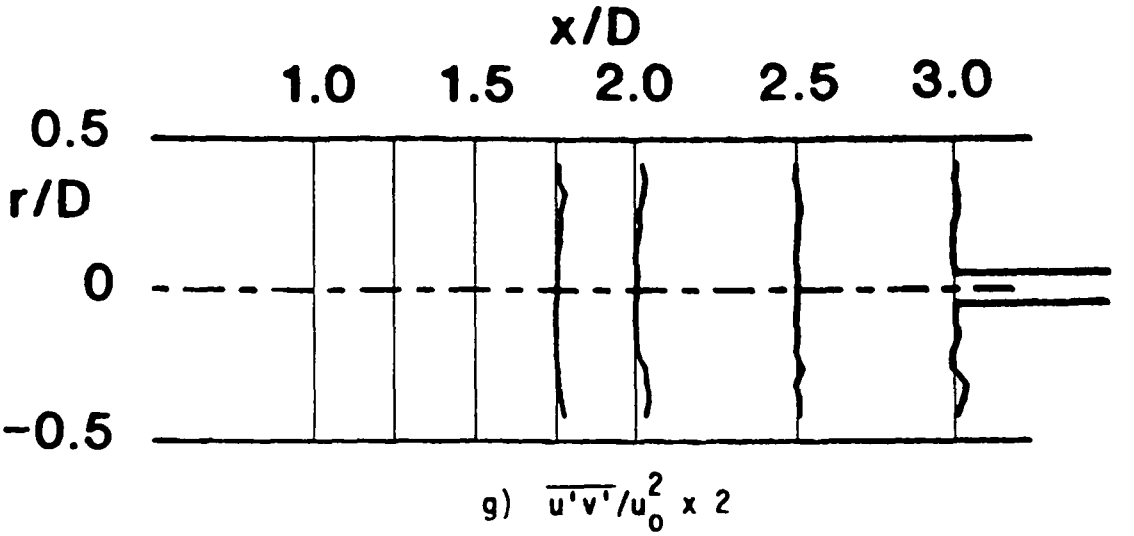

g) $\overline{u'v'}/u_o^2 \times 2$

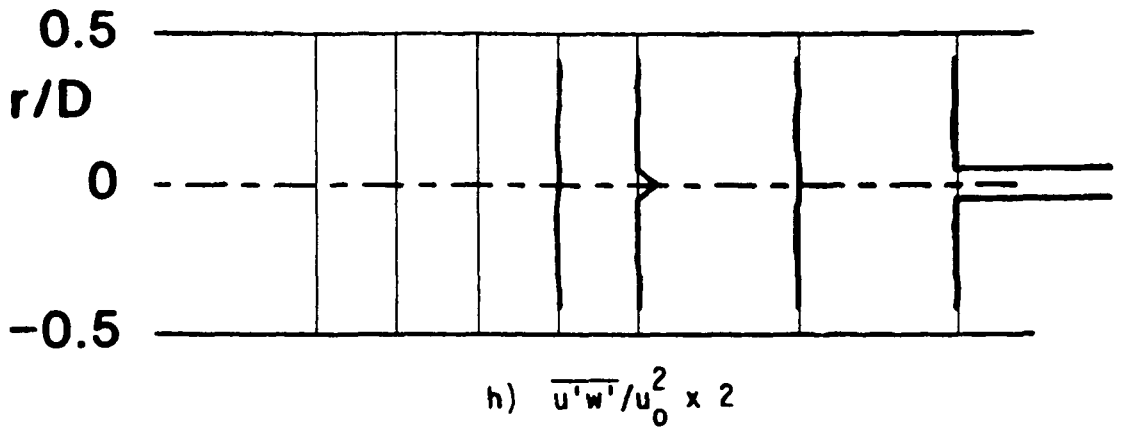

h) $\overline{u'w'}/u_o^2 \times 2$

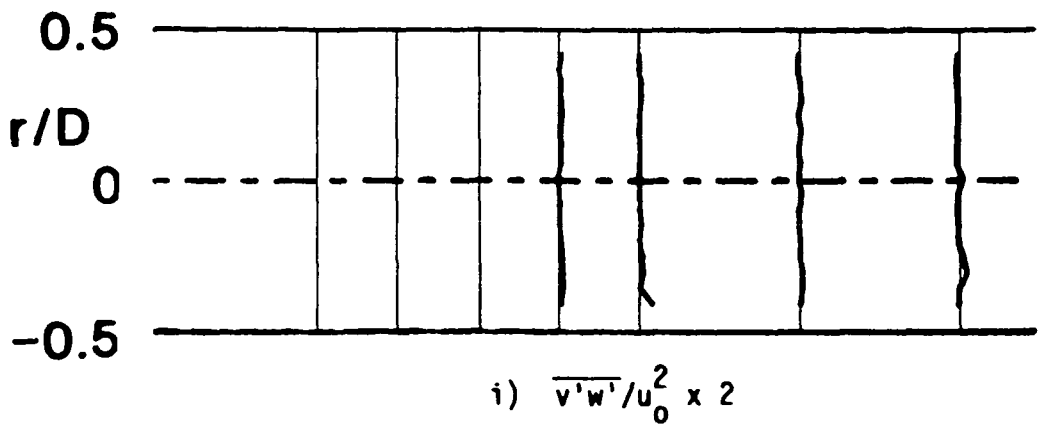

i) $\overline{v'w'}/u_o^2 \times 2$

Figure 21. (Continued)

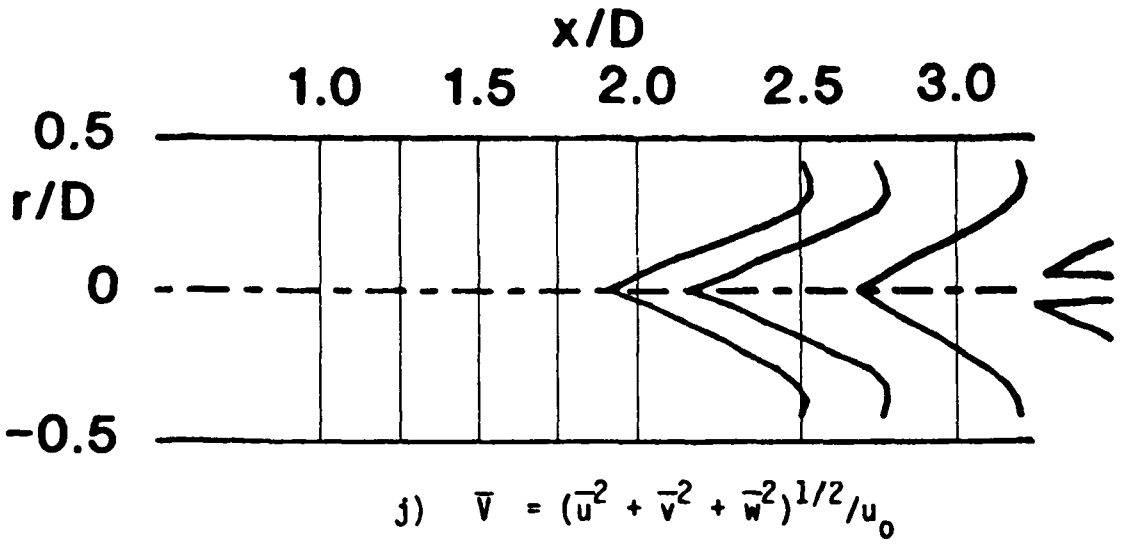

j) $\bar{V} = (\bar{u}^2 + \bar{v}^2 + \bar{w}^2)^{1/2}/u_o$

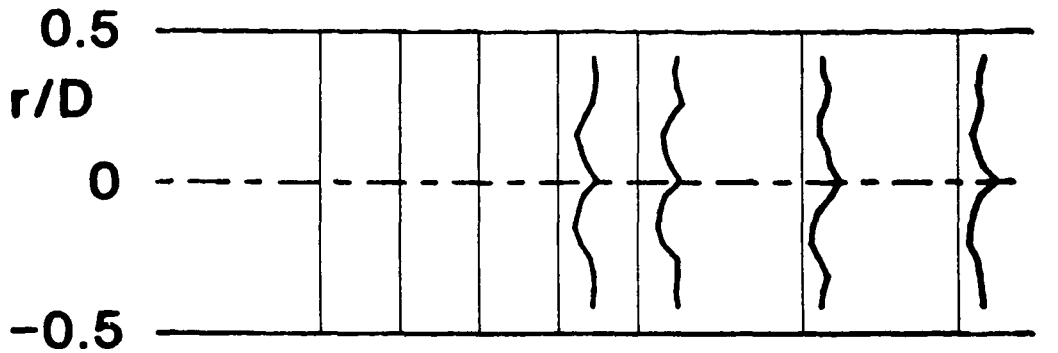

k) $u'_{rms}/\bar{u} \times 2$

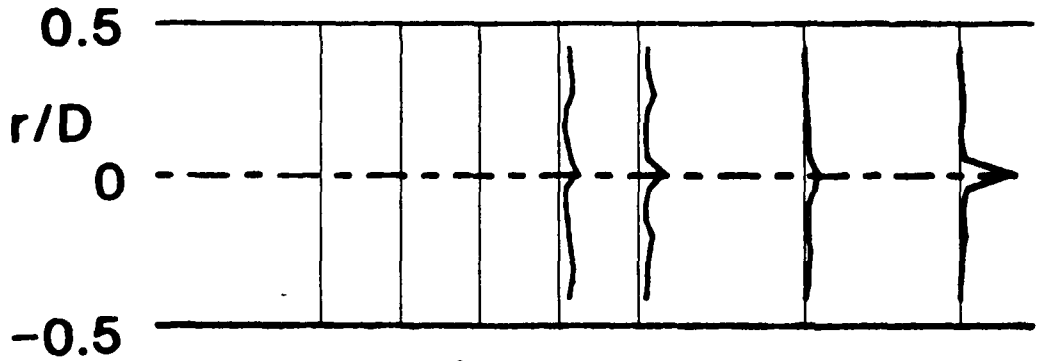

l) $\frac{1}{2}(u'^2_{rms} + v'^2_{rms} + w'^2_{rms})/u_o^2 \times 2$

Figure 21. (Continued)

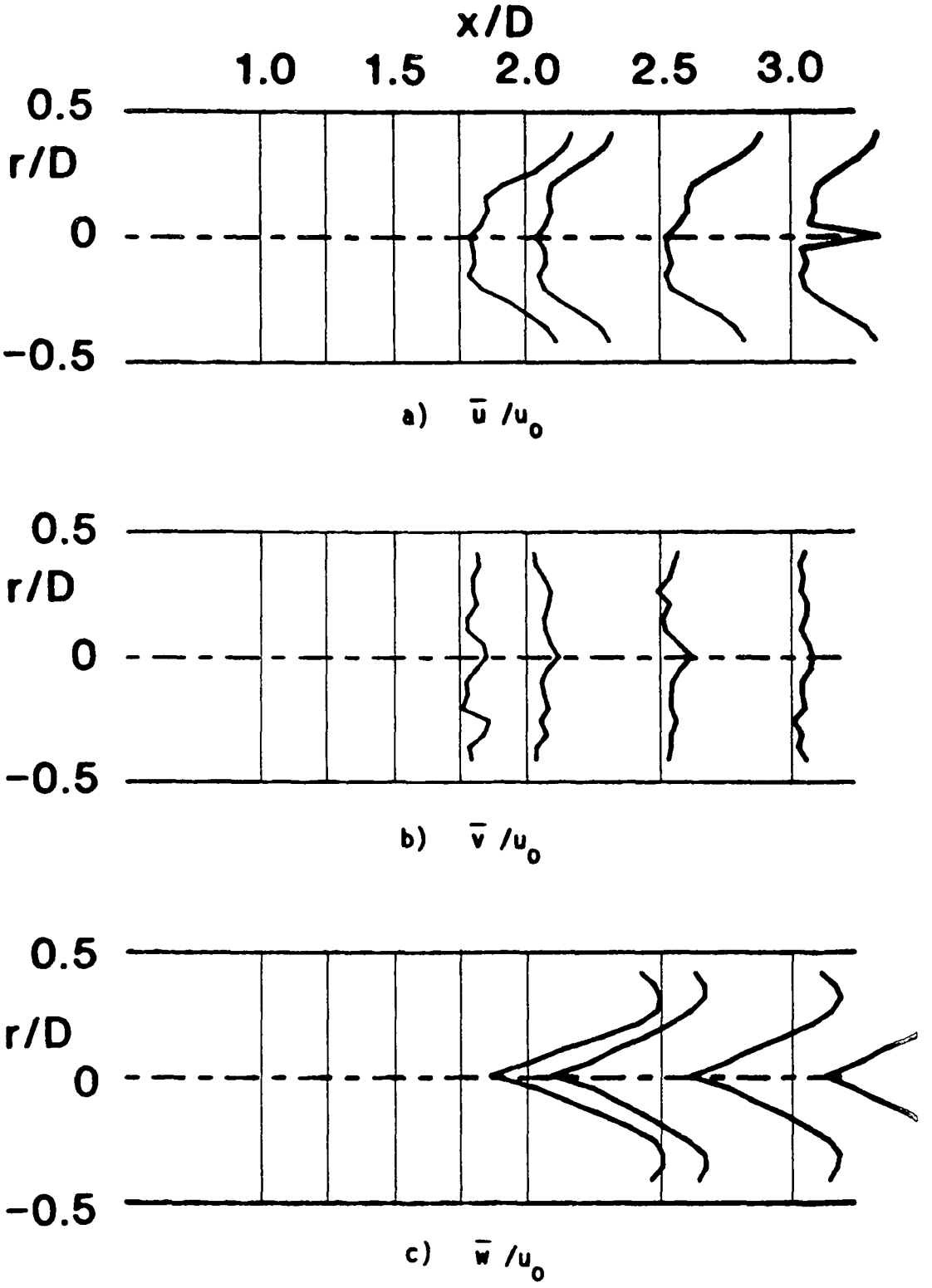

Figure 22. Time-Mean and Turbulent Flowfield, R = 4, ϕ = 70 Degrees, Traverse Angle θ = 330 Degrees.

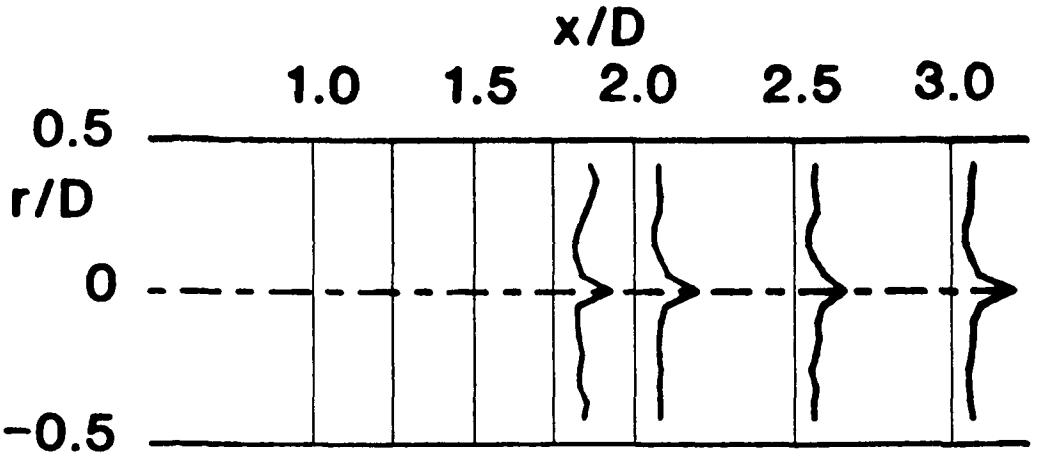

d) u'_{rms}/u_o x 2

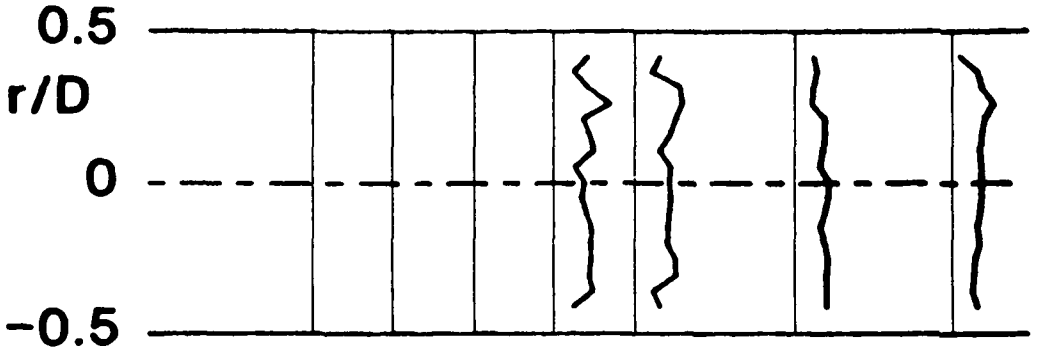

e) v'_{rms}/u_o x 2

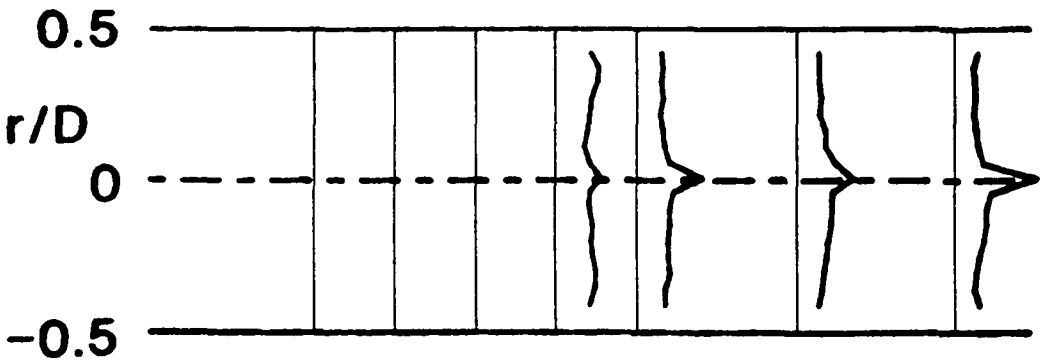

f) w'_{rms}/u_o x 2

Figure 22. (Continued)

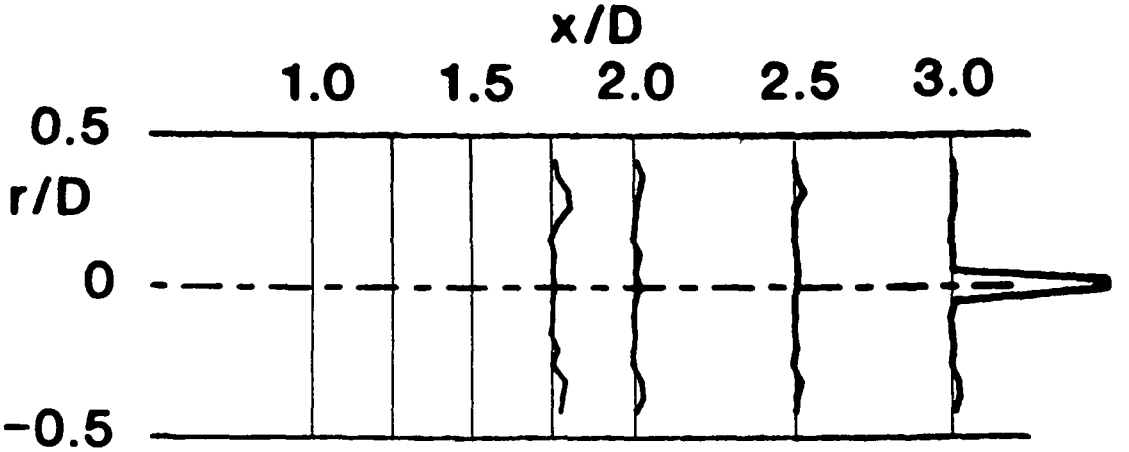

g) $\overline{u'v'}/u_o^2 \times 2$

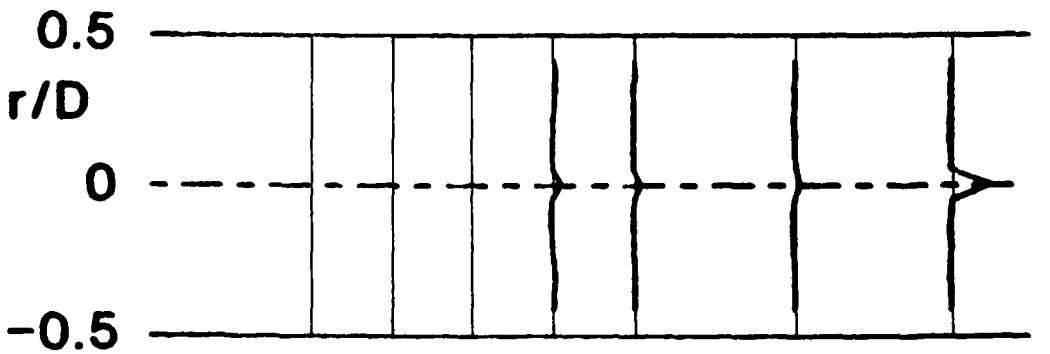

h) $\overline{u'w'}/u_o^2 \times 2$

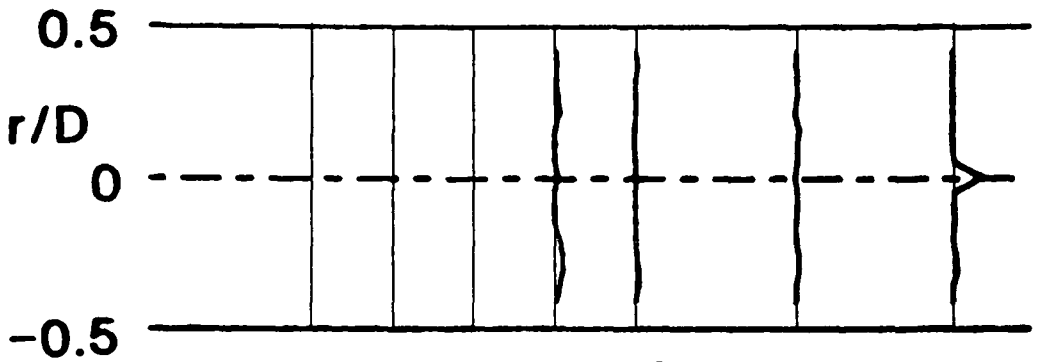

i) $\overline{v'w'}/u_o^2 \times 2$

Figure 22. (Continued)

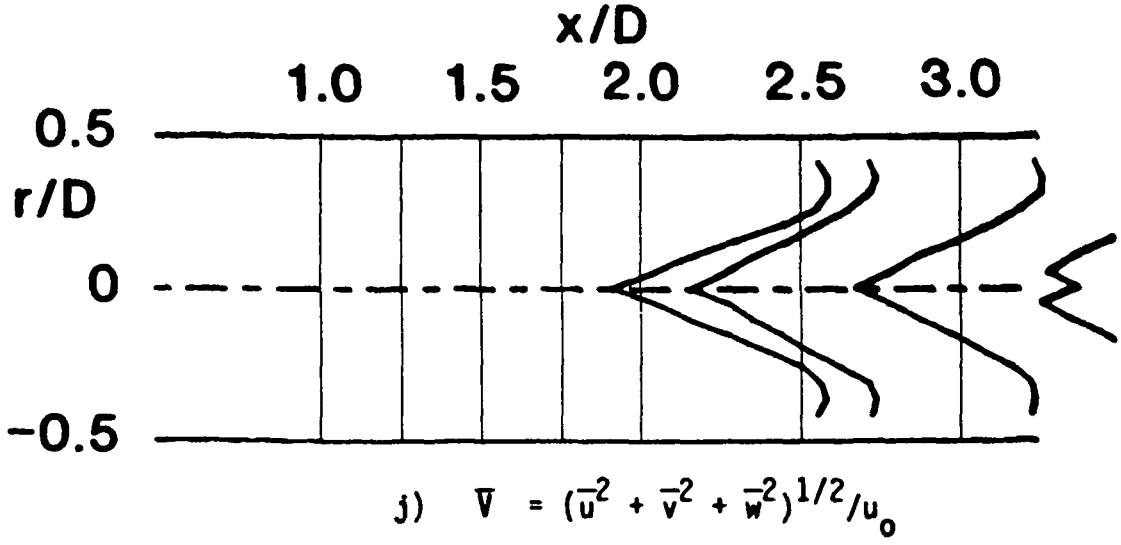

j) $\bar{V} = (\bar{u}^2 + \bar{v}^2 + \bar{w}^2)^{1/2}/u_o$

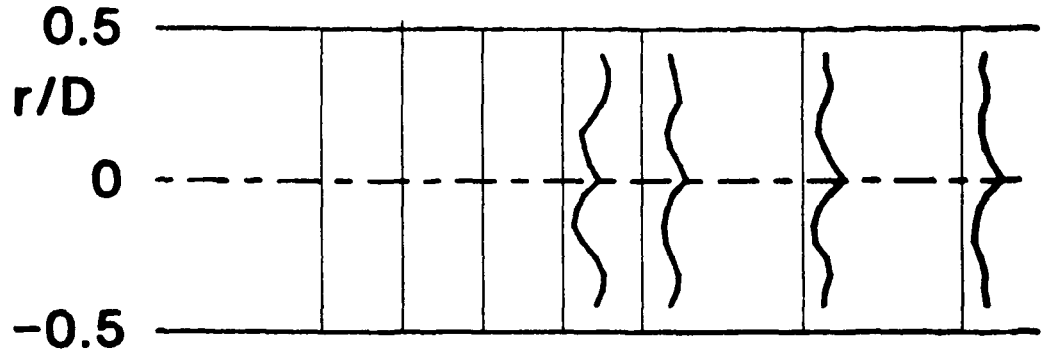

k) $u'_{rms}/\bar{u} \times 2$

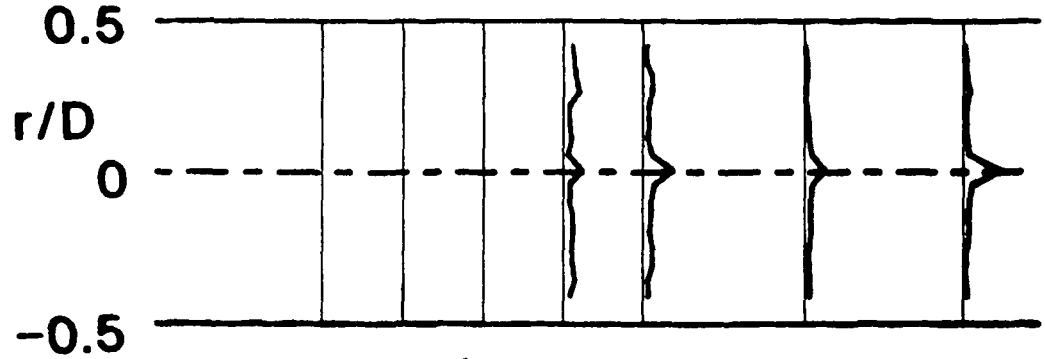

l) $\frac{1}{2}(u'^2_{rms} + v'^2_{rms} + w'^2_{rms})/u_o^2 \times 2$

Figure 22. (Continued)

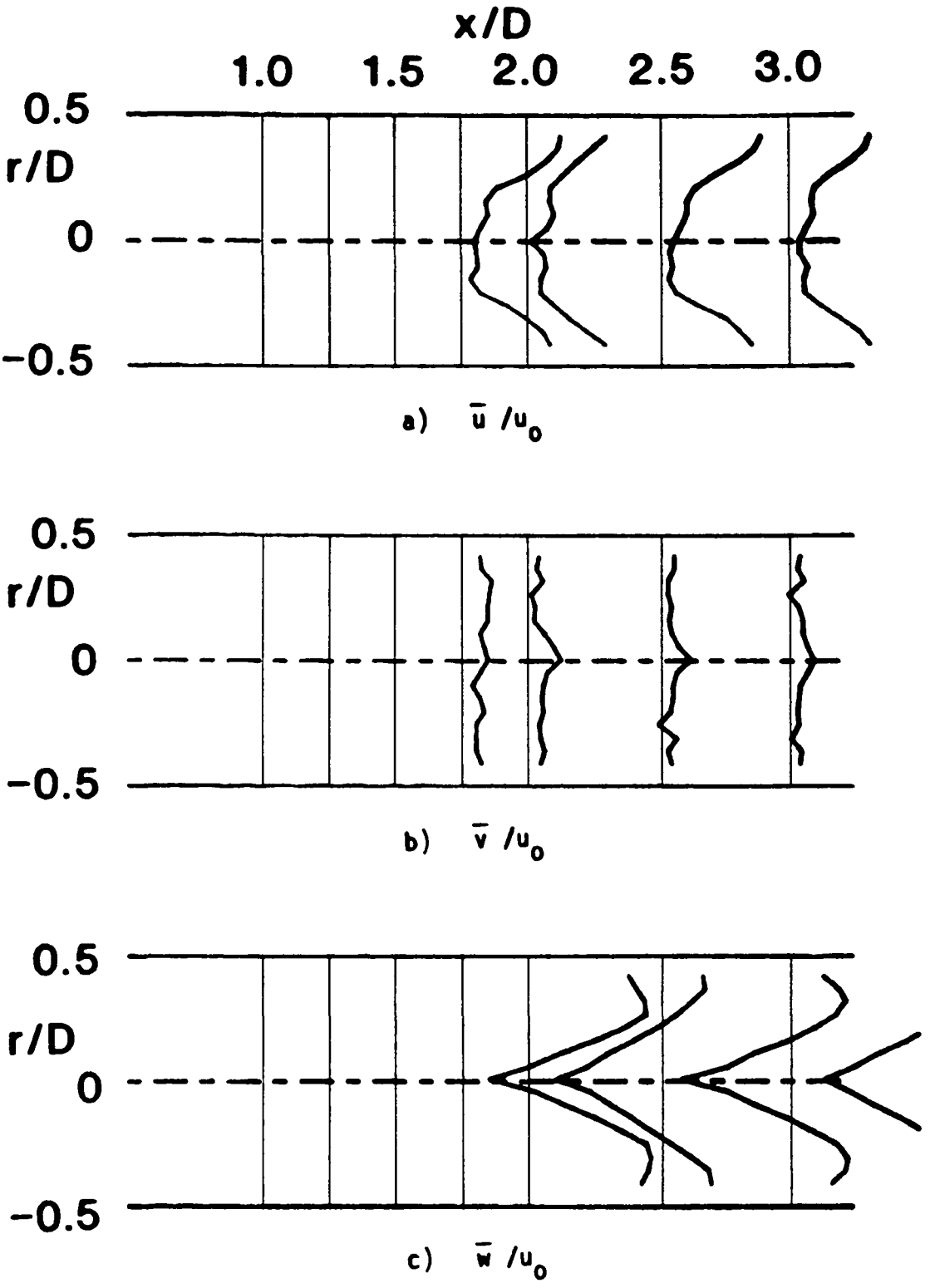

Figure 23. Time-Mean and Turbulent Flowfield, R = 4, ϕ = 70 Degrees, Traverse Angle θ = 0 Degrees.

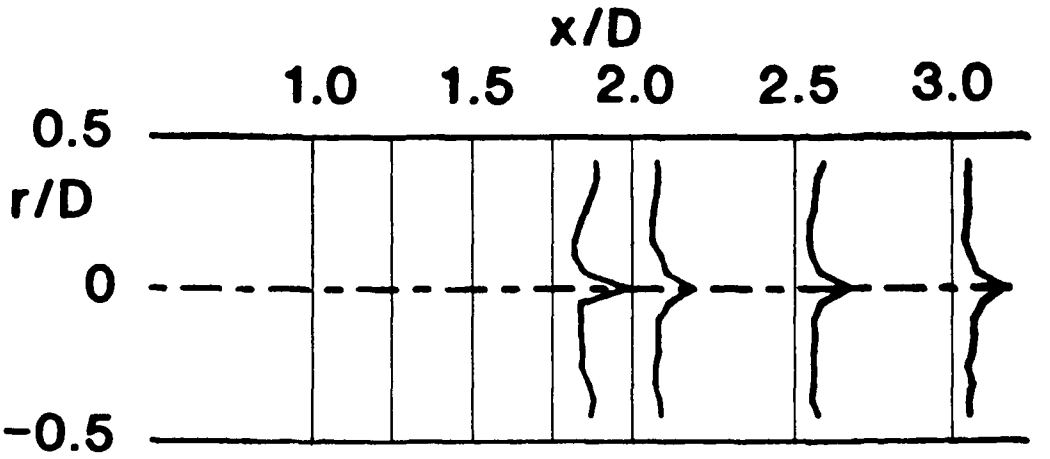

d) u'_{rms}/u_o x 2

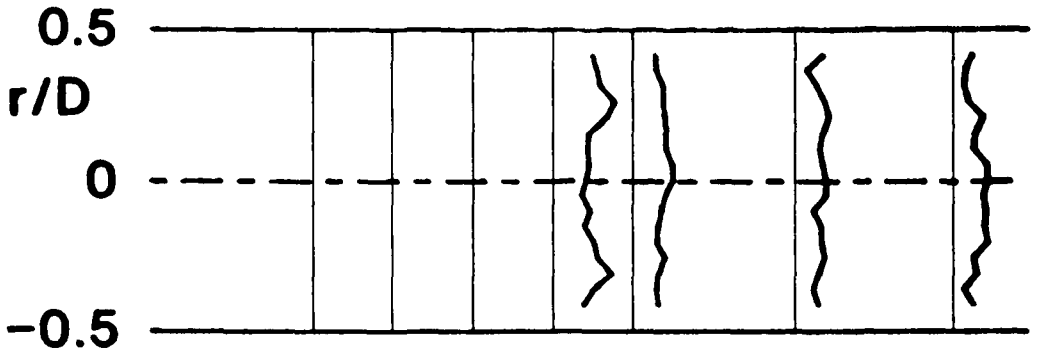

e) v'_{rms}/u_o x 2

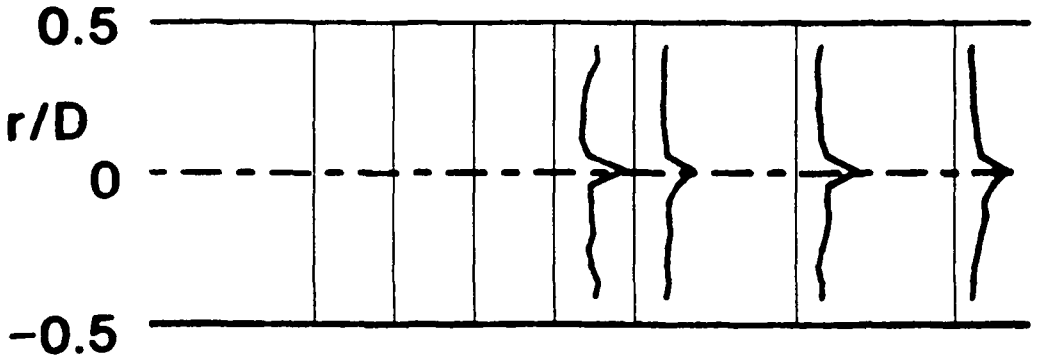

f) w'_{rms}/u_o x 2

Figure 23. (Continued)

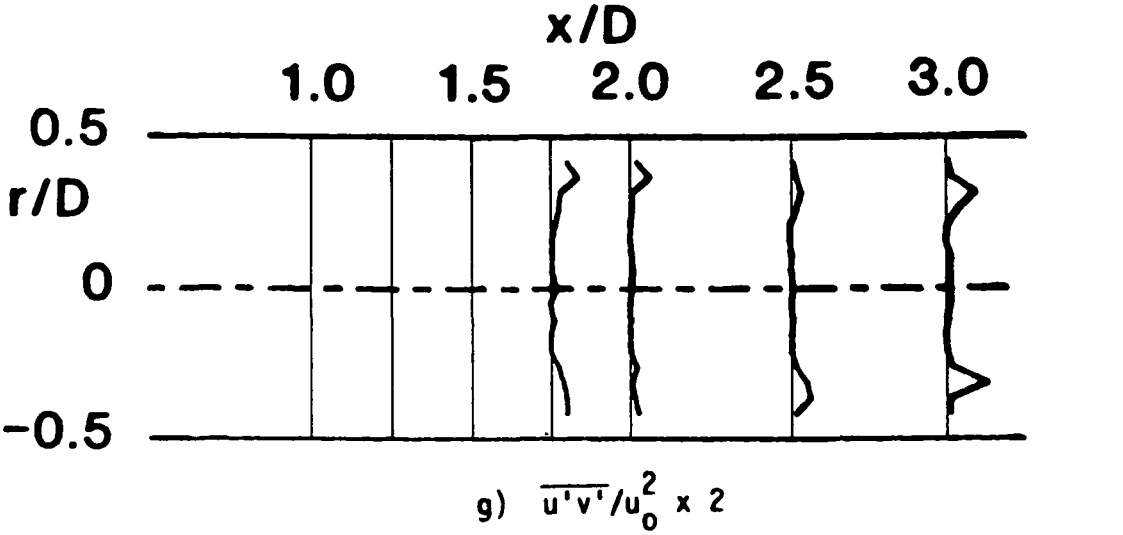

g) $\overline{u'v'}/u_o^2 \times 2$

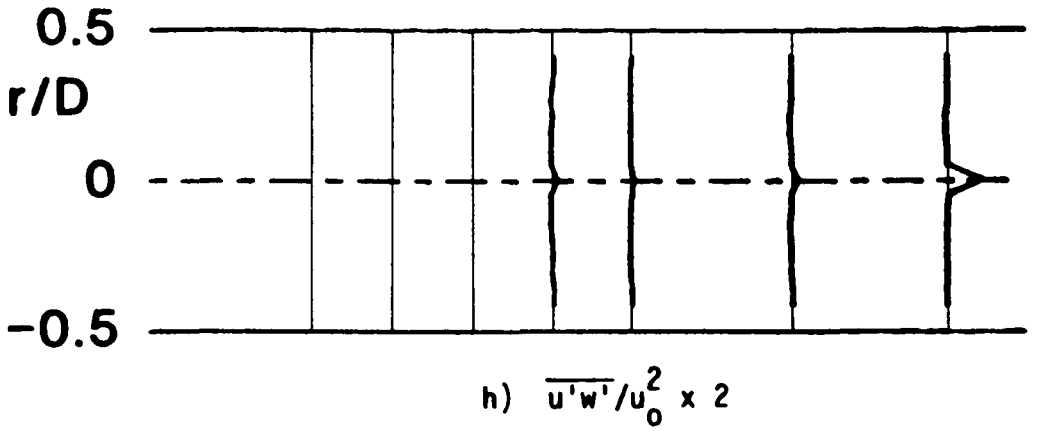

h) $\overline{u'w'}/u_o^2 \times 2$

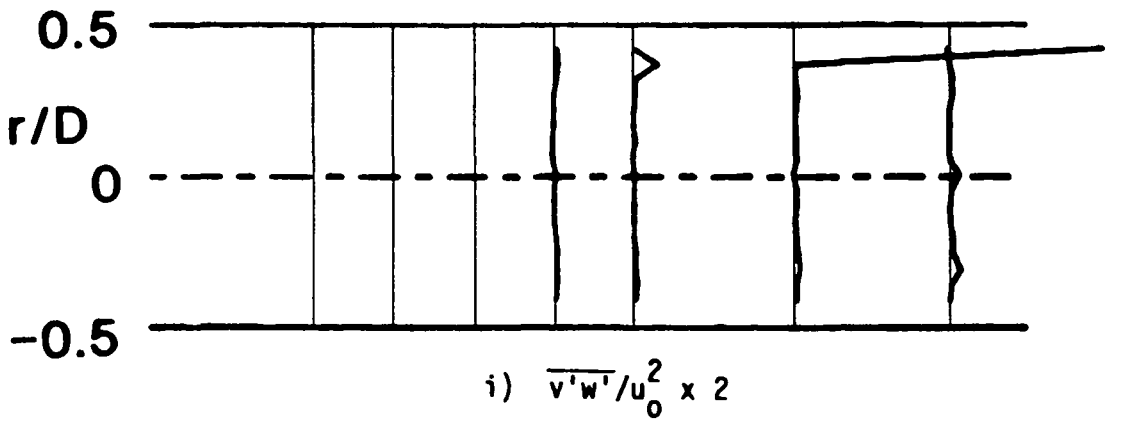

i) $\overline{v'w'}/u_o^2 \times 2$

Figure 23. (Continued)

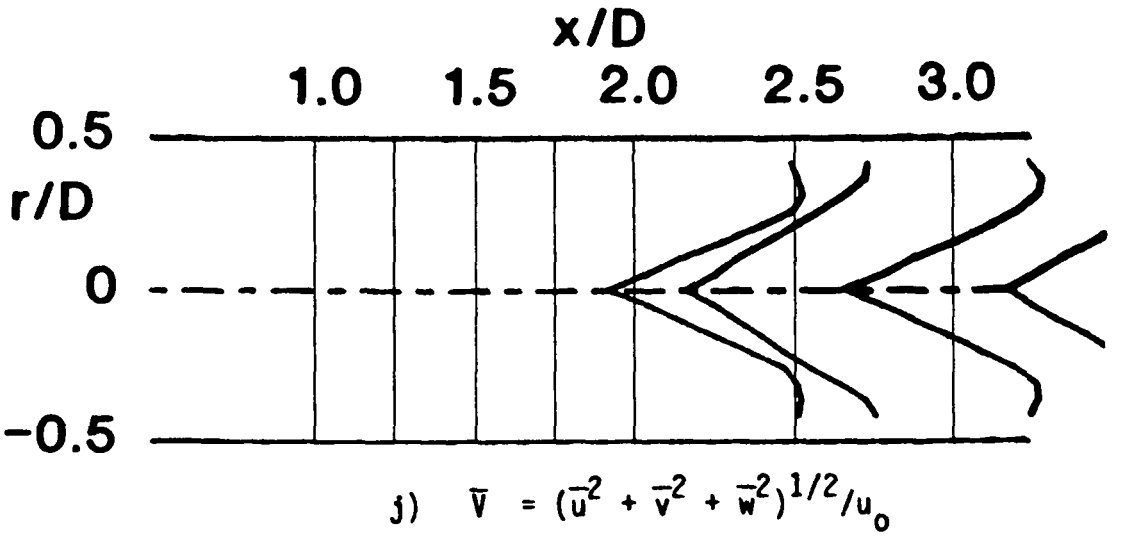

j) $\bar{V} = (\bar{u}^2 + \bar{v}^2 + \bar{w}^2)^{1/2}/u_o$

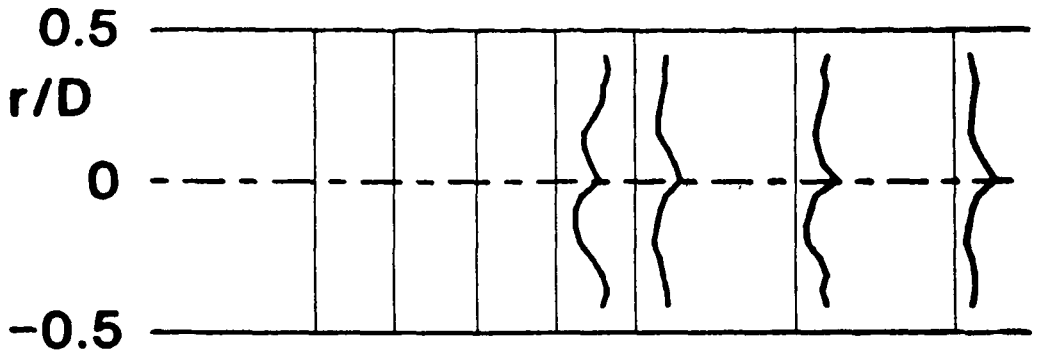

k) $u'_{rms}/\bar{u} \times 2$

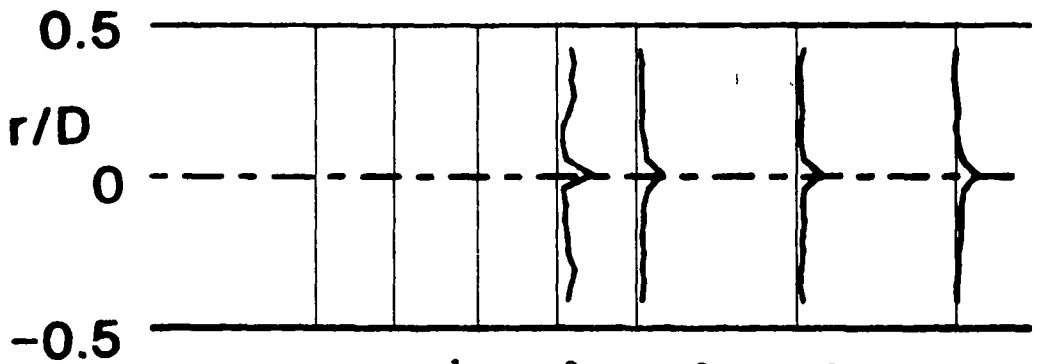

l) $\frac{1}{2}(u'_{rms}{}^2 + v'_{rms}{}^2 + w'_{rms}{}^2)/u_o^2 \times 2$

Figure 23. (Continued)

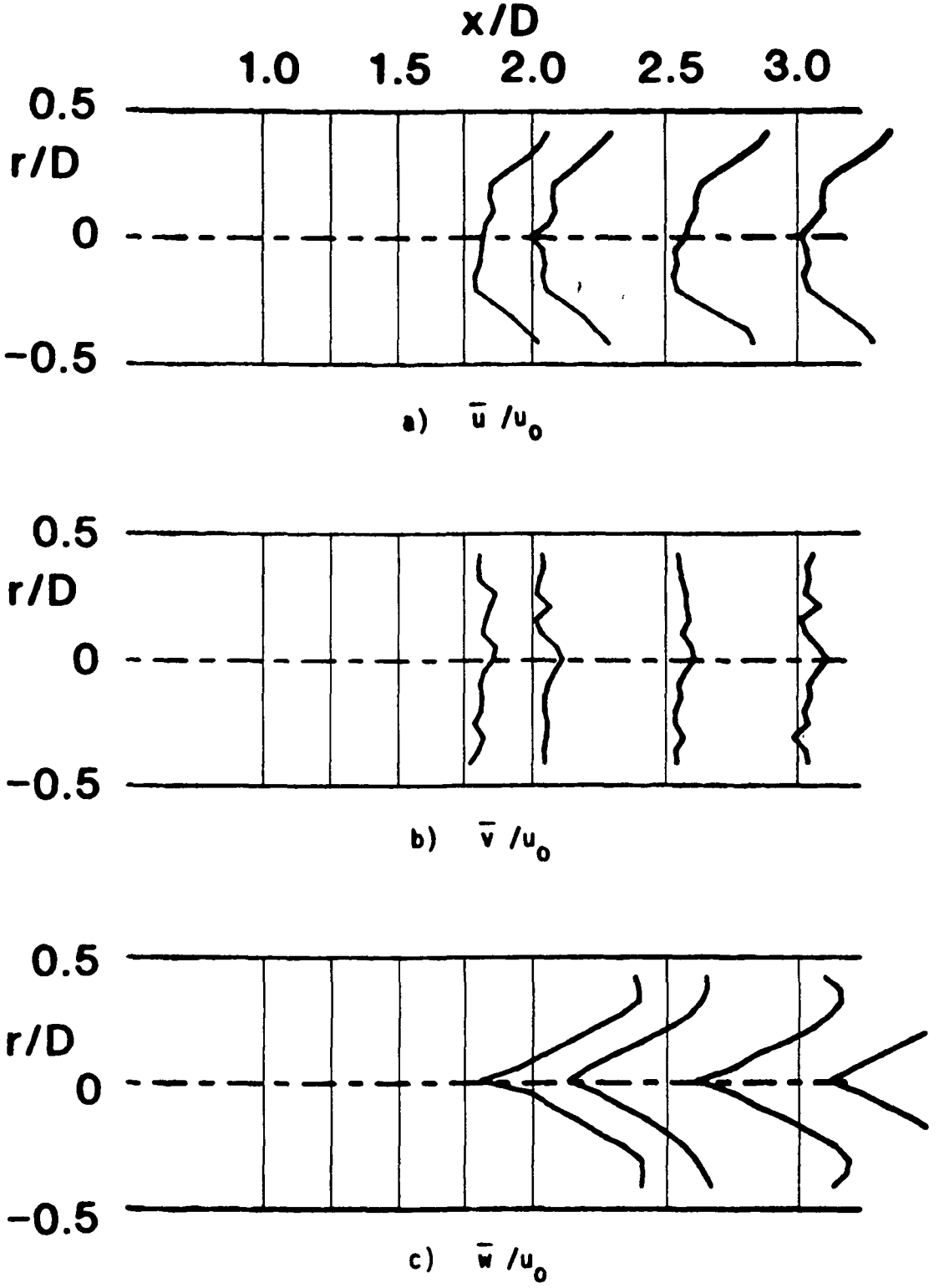

Figure 24. Time-Mean and Turbulent Flowfield, R = 4, ϕ = 70 Degrees, Traverse Angle θ = 30 Degrees.

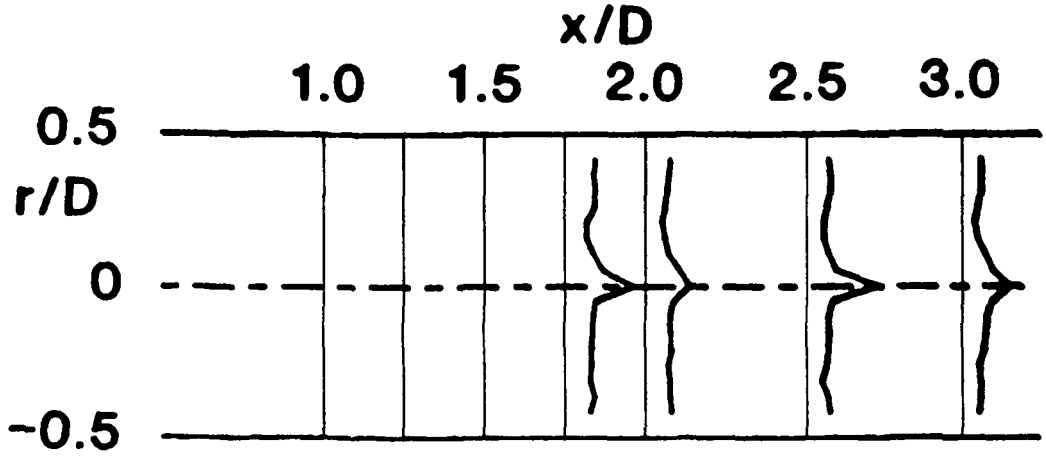

d) u'_{rms}/u_o x 2

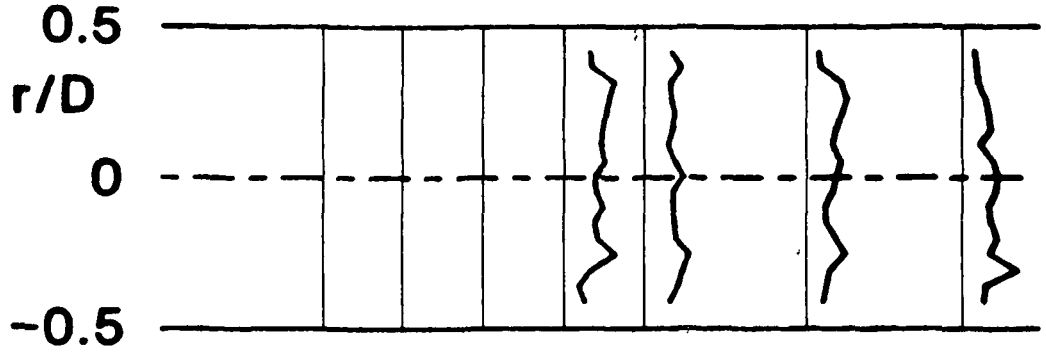

e) v'_{rms}/u_o x 2

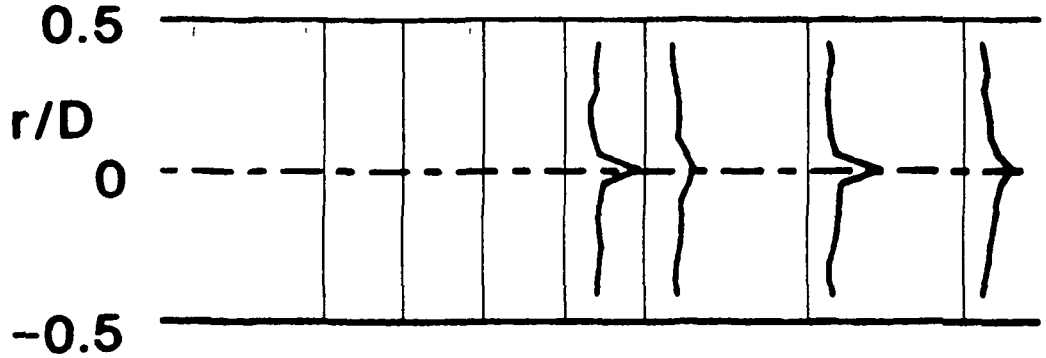

f) w'_{rms}/u_o x 2

Figure 24. (Continued)

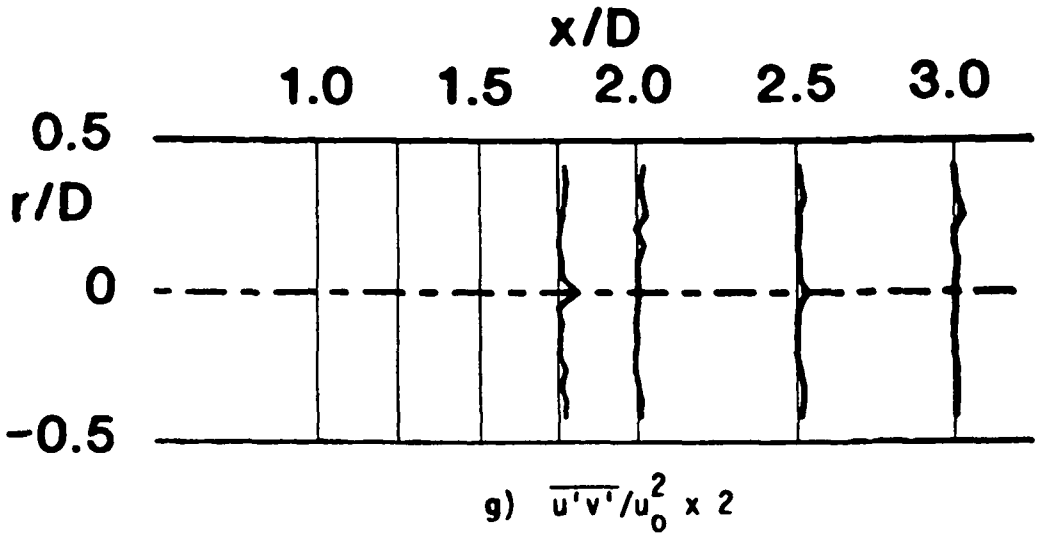

g) $\overline{u'v'}/u_o^2 \times 2$

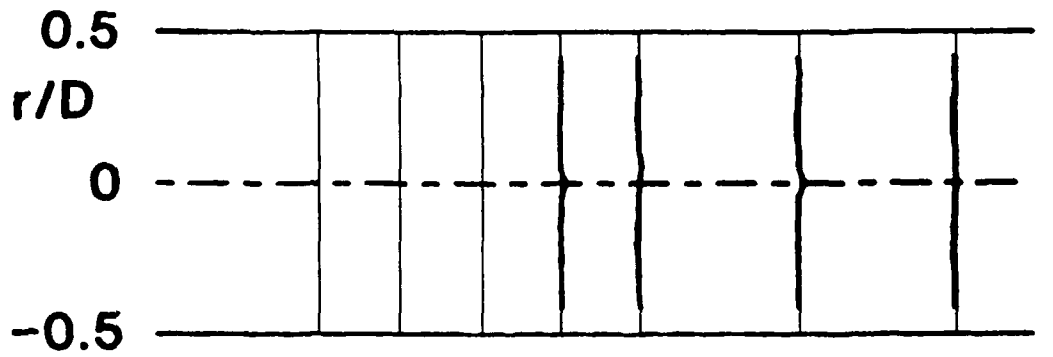

h) $\overline{u'w'}/u_o^2 \times 2$

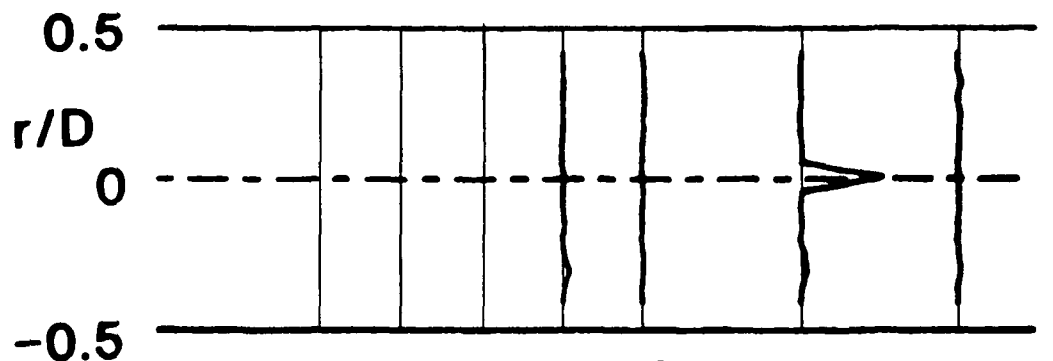

i) $\overline{v'w'}/u_o^2 \times 2$

Figure 24. (Continued)

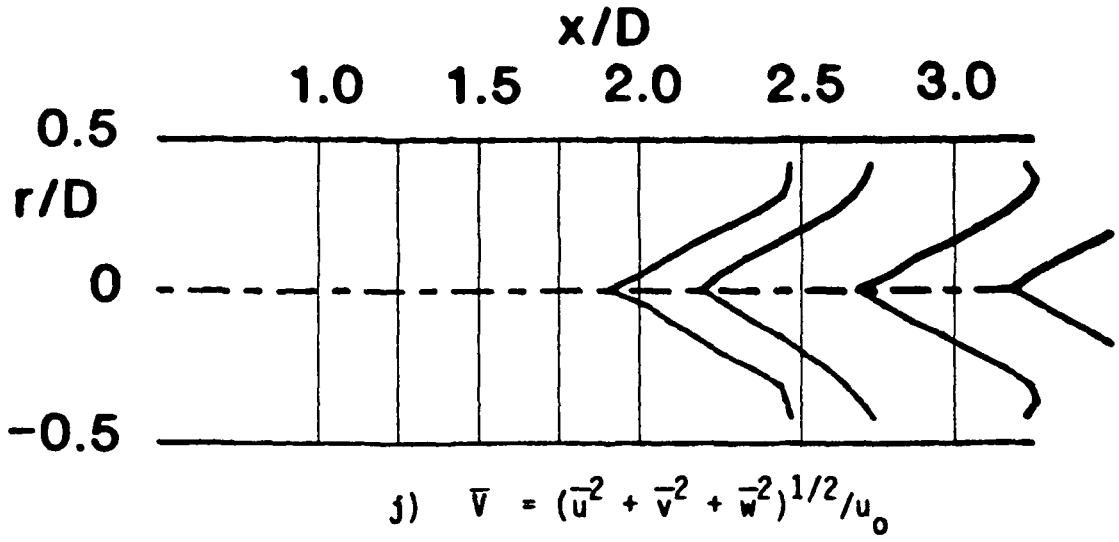

j) $\bar{V} = (\bar{u}^2 + \bar{v}^2 + \bar{w}^2)^{1/2}/u_o$

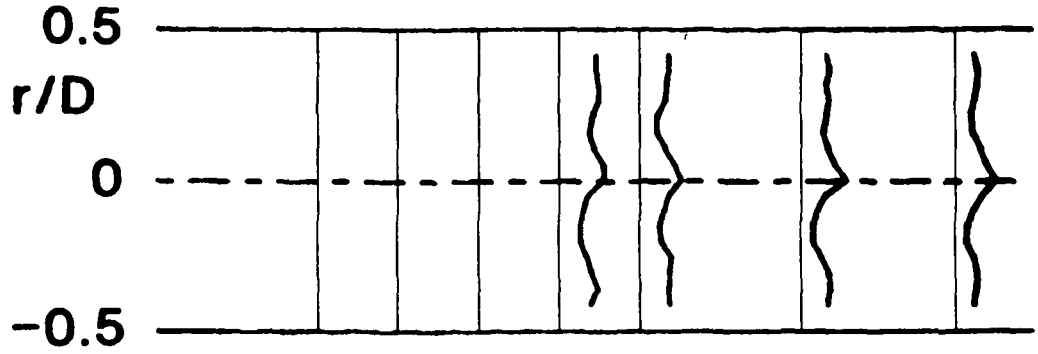

k) $u'_{rms}/\bar{u} \times 2$

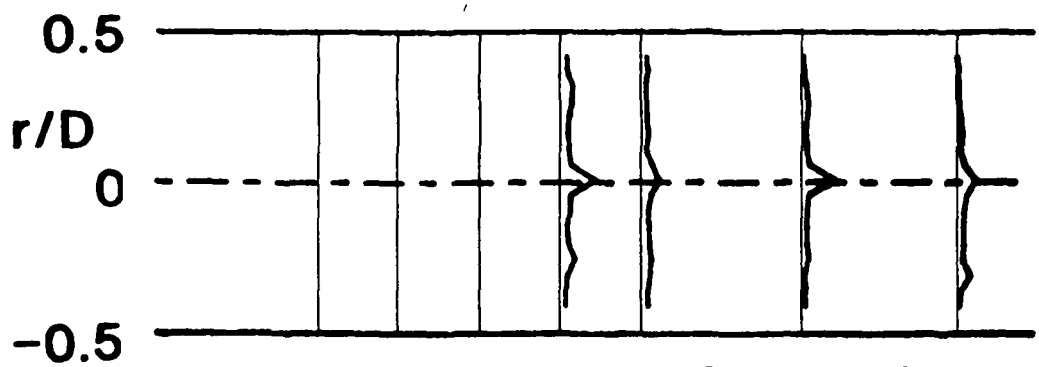

l) $\frac{1}{2}(u'^2_{rms} + v'^2_{rms} + w'^2_{rms})/u_o^2 \times 2$

Figure 24. (Continued)

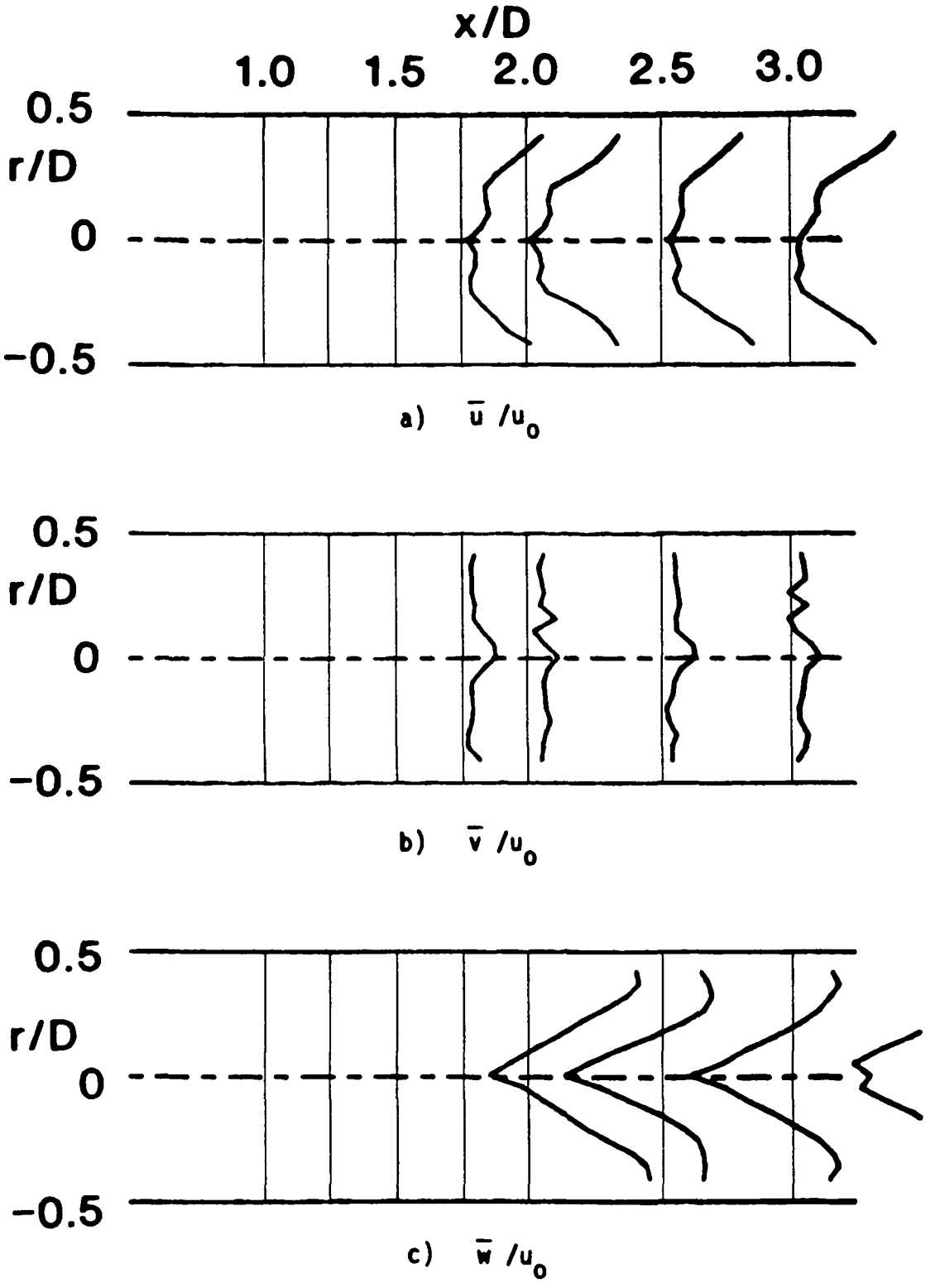

Figure 25. Time-Mean and Turbulent Flowfield, R = 4, ϕ = 70 Degrees, Traverse Angle θ = 60 Degrees.

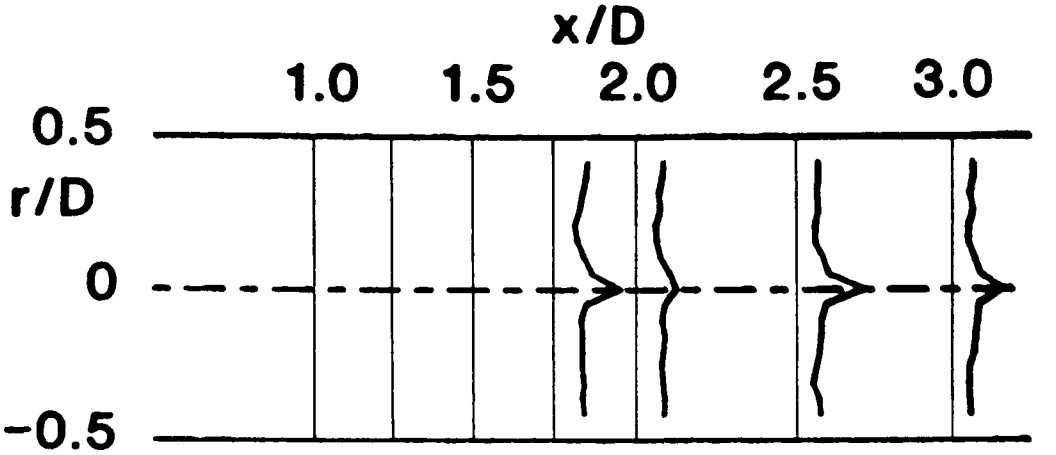

d) u'_{rms}/u_o x 2

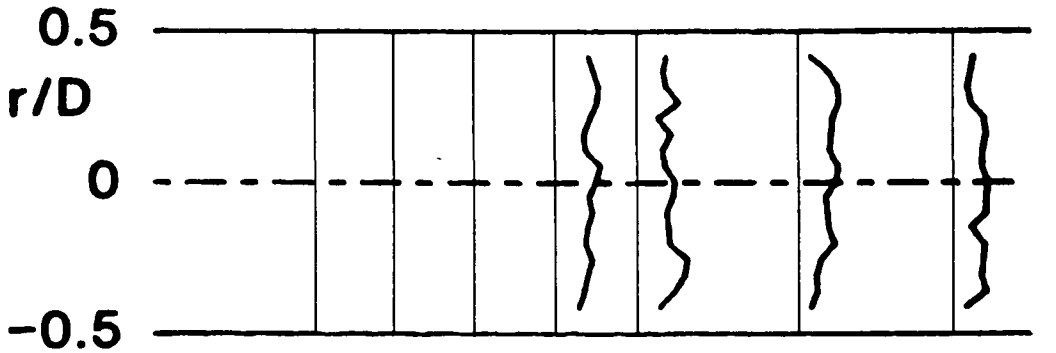

e) v'_{rms}/u_o x 2

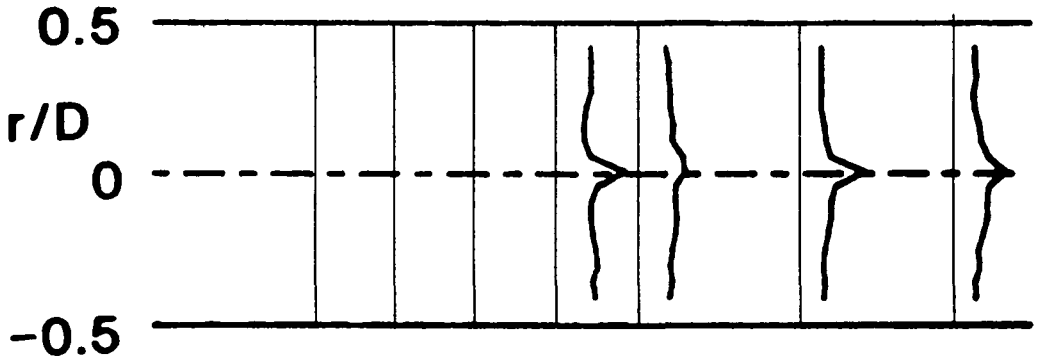

f) w'_{rms}/u_o x 2

Figure 25. (Continued)

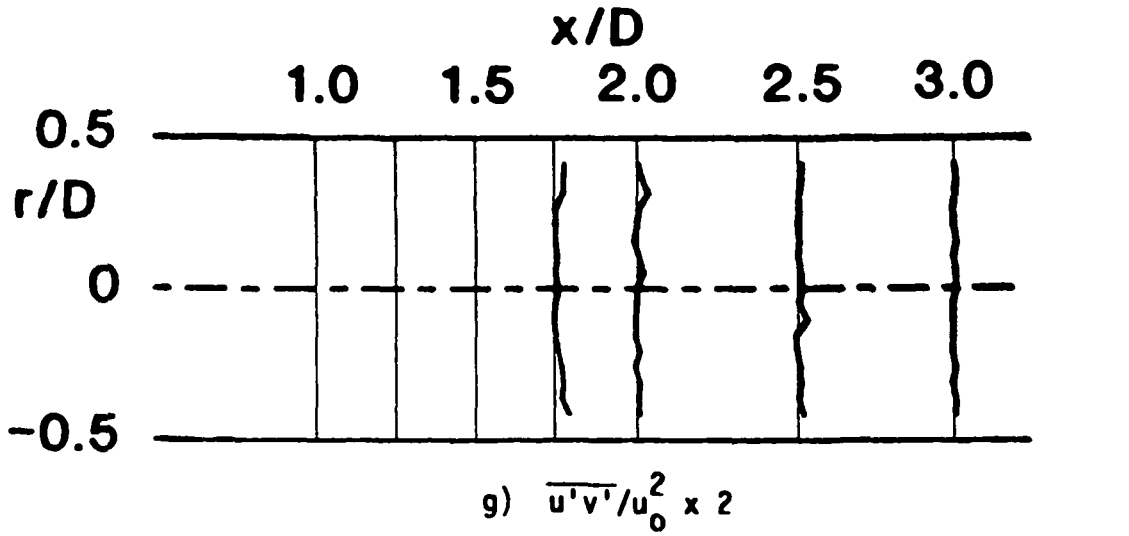

g) $\overline{u'v'}/u_o^2 \times 2$

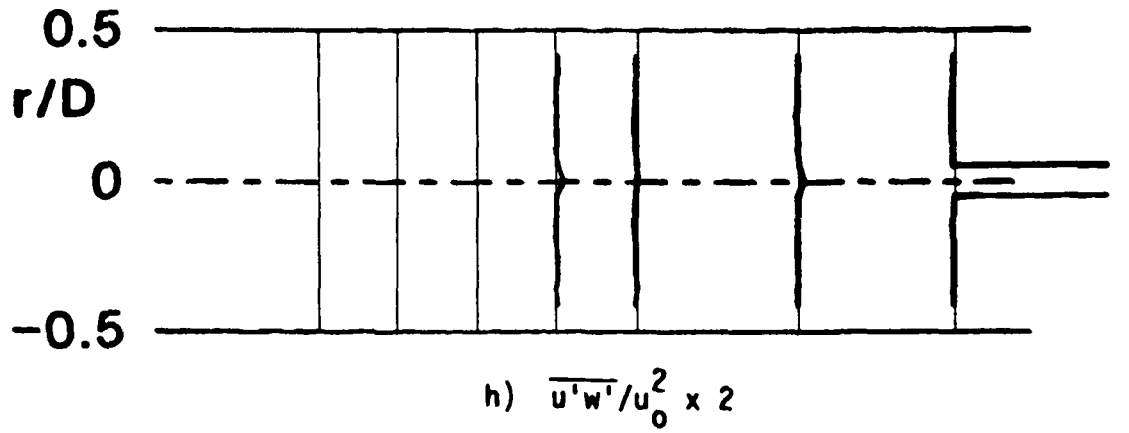

h) $\overline{u'w'}/u_o^2 \times 2$

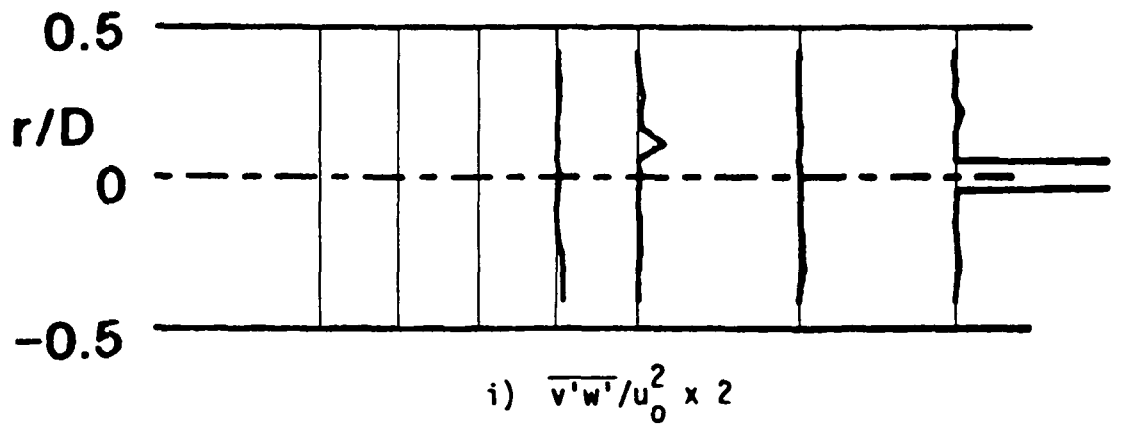

i) $\overline{v'w'}/u_o^2 \times 2$

Figure 25. (Continued)

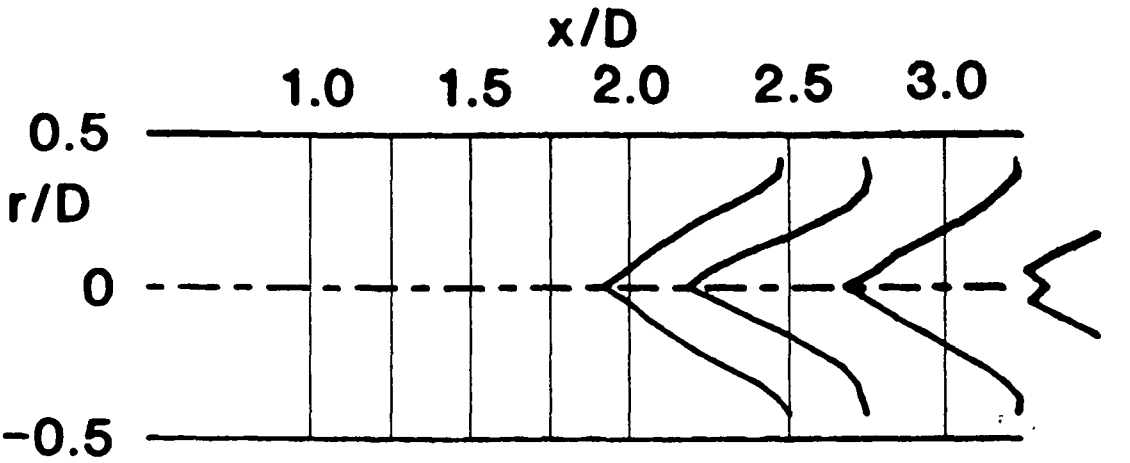

j) $\bar{V} = (\bar{u}^2 + \bar{v}^2 + \bar{w}^2)^{1/2}/u_o$

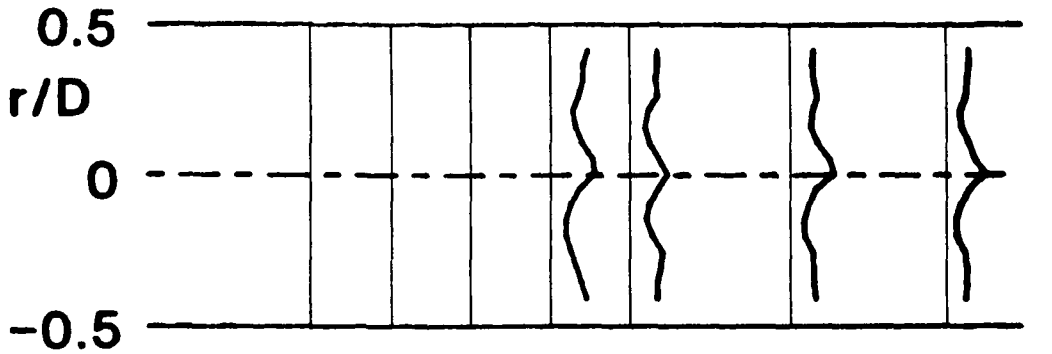

k) $u'_{rms}/\bar{u} \times 2$

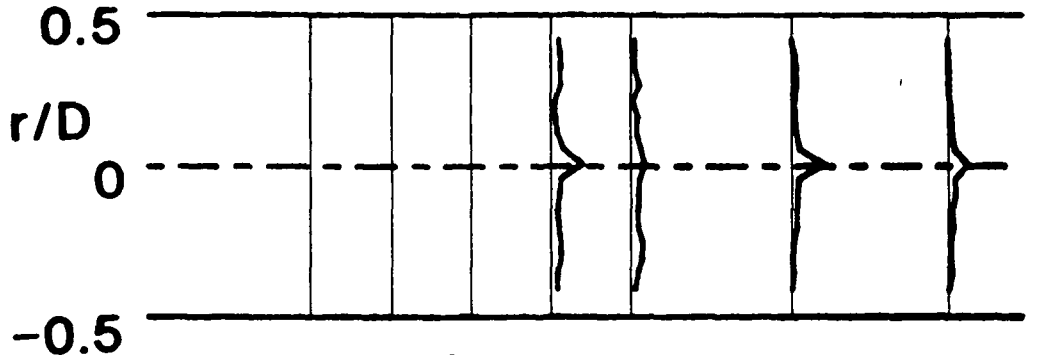

l) $\frac{1}{2}(u'_{rms}{}^2 + v'_{rms}{}^2 + w'_{rms}{}^2)/u_o^2 \times 2$

Figure 25. (Continued)

1 Report No	2 Government Accession No	3 Recipient's Catalog No
NASA CR-175041		

4 Title and Subtitle	5 Report Date
Experiments on Two Opposed Lateral Jets Injected Into Swirling Crossflow	January 1986
	6 Performing Organization Code

7 Author(s)	8 Performing Organization Report No
C.B. McMurry and D.G. Lilley	None
	10 Work Unit No

9 Performing Organization Name and Address	11 Contract or Grant No
Oklahoma State University School of Mechanical and Aerospace Engineering Stillwater, Oklahoma 74078	NAG 3-549
	13 Type of Report and Period Covered
12 Sponsoring Agency Name and Address	Contractor Report
National Aeronautics and Space Administration Washington, D.C. 20546	14 Sponsoring Agency Code 533-04-1A

15 Supplementary Notes

Final report. Project Manager, James D. Holdeman, Internal Fluid Mechanics Division, NASA Lewis Research Center, Cleveland, Ohio 44135. This report was a dissertation submitted by C.B. McMurry to the faculty of the Graduate College of Oklahoma State University in partial fulfillment of the requirements for the degree Master of Science in December 1985.

16 Abstract

Experiments have been conducted to obtain the time-mean and turbulent quantities of opposed lateral jets in a low speed, nonreacting flowfield. A jet-to-crossflow velocity ratio of $R = v_j/u_o = 4$ was used throughout the experiments, with swirl vane angles of $\alpha = 0$ (swirler removed), 45 and 70° used with the crossflow. Flow visualization techniques used were neutrally-buoyant helium-filled soap bubbles and multispark photography in order to obtain the gross flowfield characteristics. Measurements of time-mean and turbulent quantities were obtained utilizing a six-orientation single hot-wire technique. For the non-swirling case, the jets were found not to penetrate past the test-section centerline, in contrast to the single lateral jet with the same jet-to-crossflow velocity ratio. In the swirling cases, the crossflow remains in a narrow region near the wall of the test section. The opposed jets are swept from their vertical courses into spiral trajectories close to the confining walls. Extensive results are presented in r-x plane plots.

17 Key Words (Suggested by Author(s))	18 Distribution Statement
Turbulent jets; Jets in crossflow; Confined flows; Turbulent mixing; Deflected jets; Axisymmetric combustor	Unclassified - unlimited STAR Category 07

19 Security Classif (of this report)	20 Security Classif (of this page)	21 No of pages	22 Price*
Unclassified	Unclassified	115	A05

*For sale by the National Technical Information Service, Springfield, Virginia 22161

National Aeronautics and
Space Administration

Lewis Research Center
Cleveland, Ohio 44135

SECOND CLASS MAIL

ADDRESS CORRECTION REQUESTED

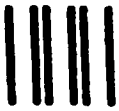

Official Business
Penalty for Private Use $300

Postage and Fees Paid
National Aeronautics and
Space Administration
NASA-451